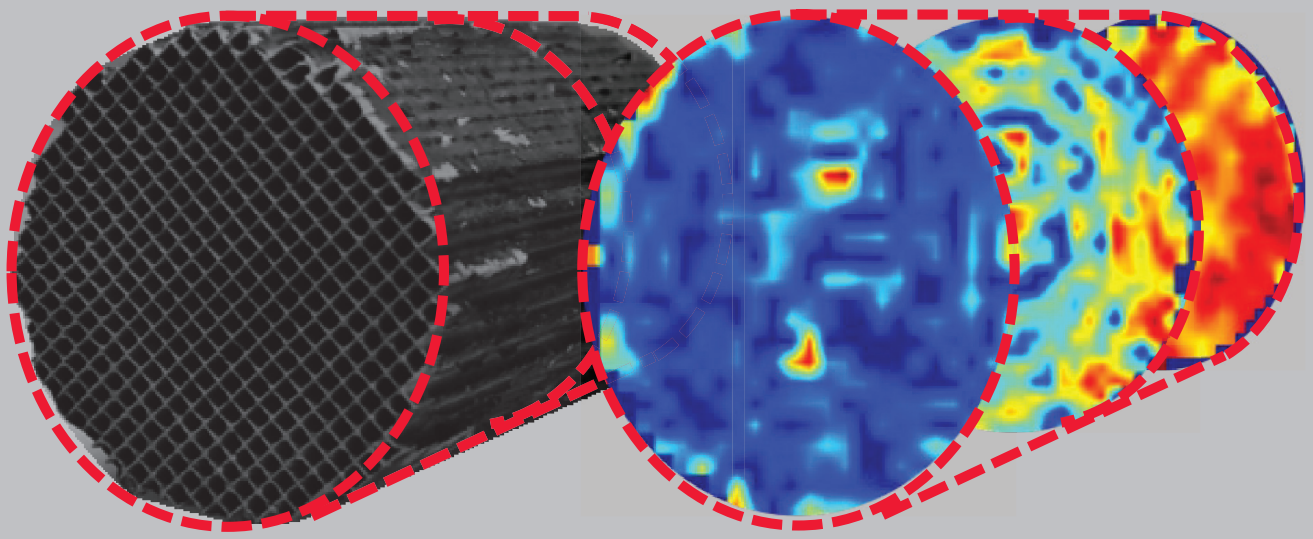

Jürgen Ulpts

Validation of modeling approaches of heterogeneously catalyzed gas phase reaction processes by applying NMR imaging methods

Validation of modeling approaches of heterogeneously catalyzed gas phase reaction processes by applying NMR imaging methods

Vom Fachbereich Produktionstechnik

der

UNIVERSITÄT BREMEN

zur Erlangung des Grades
Doktor-Ingenieur
genehmigte

Dissertation

von

Dipl.-Ing. Jürgen Ulpts

Gutachter:
Prof. Dr.-Ing. Jorg Thöming, Universität Bremen
Prof. Dr. Raimund Horn, Technische Universität Hamburg-Harburg

Tag der mündlichen Prüfung: 06.12.2017

Für meine Familie.

Danksagung

Die vorliegende Arbeit entstand im Rahmen einer Kooperation zwischen dem Zentrum für Umweltforschung und nachhaltige Technologie im Fachbereich Produktionstechnik der Universität Bremen sowie der Arbeitsgruppe in-vivo-MR im Fachbereich 2 der Universität Bremen.
Mein besonderer Dank gilt daher Prof. Dr.-Ing. Jorg Thöming für sein Vertrauen in meine Person, die Forschungsidee dieser Kooperation zum Erfolg zu bringen, sowie für die Betreuung und Begutachtung meiner Dissertation.
Mindestens zu gleichen Teilen gebührt mein Dank auch PD Dr. Wolfgang Dreher der in-vivo-MR Arbeitsgruppe: Er hat nicht nur einem anfangs völlig fachfremden Ingenieur die NMR Grundlagen nahegebracht und unermüdlich Forschungsansätze diskutiert, sondern auch in ewig langen Messkampagnen bis tief in die Nacht und am Wochenende seine Freizeit geopfert. Nicht zuletzt deswegen konnte diese Arbeit zum Erfolg geführt werden. Auch möchte ich seinem Kollegen Peter Erhard ganz herzlich für seine Unterstützung und hilfreichen Ratschläge danken.
Darüber hinaus gilt mein Dank auch Prof. Dr. Raimund Horn, für das Interesse an meiner Arbeit und die Bereitschaft zur Übernahme des Zweitgutachtens.
Ein herzlicher Dank gebührt weiterhin meinen Kollegen und Freunden aus dem Fachbereich, durch die ich meine Promotionszeit in schöner Erinnerung behalten werde. Insbesondere gilt mein Dank Dr. Michael Baune und Prof. Dr. Stefan Stolte für die Vielzahl an Diskussionen und ein jederzeit offenes Ohr.
Für die tatkräftige Unterstützung im Labor und bei der Modellierung möchte ich mich zudem bei Miriam Schubert und Lars Kiewidt bedanken.
Auch möchte ich meinem Freundeskreis danken. Insbesondere Benjamin Besser, Oliver Keszöcze und Florian Meichsner waren jederzeit hilfreiche und wichtige Ansprechpartner.
Abschließend gilt meine tiefe Dankbarkeit meiner Familie und besonders meiner Frau, die während der Promotionsphase so häufig auf mich verzichten musste und trotzdem jederzeit uneingeschränkt unterstützt hat. Ohne ihren Einsatz und Verzicht hätte ich mein Promotionsvorhaben wohl nicht erfolgreich zu Ende gebracht.

Zusammenfassung

Diese Arbeit beschreibt die erstmalige Anwendung der konventionellen spektroskopischen Bildgebung (engl.: magnetic resonance spectroscopic imaging, MRSI) als Validierungswerkzeug für Gasphasenreaktormodelle. Hierzu wurden Messmethoden entwickelt, welche die in-situ-Charakterisierung eines Modelgasphasenreaktionsprozesses ermöglichen. Diese MRSI-Ansätze erlauben Konzentrations- und Temperaturmessungen innerhalb von Katalysatorbetten unter Reaktionsbedingungen, welche nur schwer mittels nicht-invasiver konventioneller Messmethoden gemessen werden können. Bei dem untersuchten System handelte es sich um die Ethylenhydrierungsreaktion, welche innerhalb eines makroskopischen Kernspinresonanz (NMR)-kompatiblen Festbettreaktor katalysiert wurde.
Da NMR-Signale der Gasphase sehr schnell abklingen, bedarf es MRSI-Methoden, die eine unmittelbare Datenerfassung nach Signalanregung ermöglichen. Daher wurde zunächst ein Mehrschicht-MRSI-Ansatz optimiert und auf einem 7-T NMR-Tomographen implementiert, um ultrakurze Echozeiten T_E zu realisieren. Diese Methode wurde in einer ersten Studie genutzt, um die Anwendbarkeit der MRSI zur Untersuchung von Gasphasenkonzentrationen innerhalb eines Festbettreaktors abschätzen zu können. Das Katalysatorbett enthielt hierbei inaktive γ-Al_2O_3-Pellets sowie katalytisch aktive Pt-Al_2O_3-Pellets, um eine Unterscheidung zwischen reaktiven und nicht-reaktiven Bereichen zu ermöglichen. So gelang es, räumliche Verteilungen der chemischen Zusammensetzung der Gasphase aus den MRSI-Datensätzen abzuleiten, einzelne katalytisch aktive Katalysatorpellets zu lokalisieren, sowie den Gesamt-Ethylenumsatz zu bestimmen. Simultan durchgeführte integrale massenspektrometrische (MS) Messungen waren in recht guter Übereinstimmung mit den per MRSI gemessenen Konzentrationen.
Auf Grundlage dieser Ergebnisse wurde der Mehrschicht-Ansatz weiterentwickelt, um 3D-MRSI-Messungen zur Untersuchung von Konzentrationsverteilungen auch in opaken monolithischen Katalysatoren zu ermöglichen. Die Modelreaktion wurde hierbei von einer Pt-beschichteten Schwammpackung bzw. einem monolithischen Wabenkörper katalysiert (Ø: 25 mm; L: 50 mm). Die 3D-MRSI-Messungen erlaubten die Ermittlung von Katalysatorträgerstruktur-abhängigen Konzentrationsverteilungen und des Gesamtreaktionsfortschritts. Um die Plausibilität dieser Messungen nachweisen zu können, wurden die experimentellen Ergebnisse mit einem 1D-Model des Reaktors verglichen, welches auf bereits veröffentlichten kinetischen Daten basierte. Gemessene und simulierte Reaktionsprofile waren hierbei in guter Übereinstimmung. Des Weiteren zeigte ein Vergleich mit simultan durchgeführten integralen MS-Konzentrationsmessungen nur Abweichungen unter 5 %.
Schließlich wurden die räumlich aufgelösten Messungen der Konzentrationsverteilungen innerhalb der monolithischen Katalysatoren mit simultanen Temperaturmessungen kombiniert. Zu diesem Zweck wurden speziell entwickelte, mit Ethylenglykol gefüllte NMR-Mehrpunkthermometer in die monolithischen Katalysatorbetten eingebracht. Die Auswertung der Ethylenglykolspektren ermöglichten die Bestimmung von nahezu kontinuierlichen longitudinalen Temperaturprofilen. Die Ergebnisse der 3D-MRSI Messungen wurden anschließend mit Simulationsrechnungen eines prädiktiven zweidimensionalen Models der Prozesse verglichen. Simulierte und gemessene Konzentrations- und Temperaturprofile waren in sehr guter Übereinstimmung; die Abweichungen waren jeweils geringer als 9 %. Konventionelle MS-Messungen lieferten einen zusätzlichen Beleg für die Genauigkeit der 3D-MRSI-Messungen sowie des 2D-Reaktormodels. Die Ergebnisse zeigen das große Potenzial der 3D-MRSI, um heterogen katalysierte Gasphasenreaktionen in makroskopischen Rohreaktoren zu untersuchen und so Entwicklung und Validierung von physikalisch konsistenten Reaktormodellen zu unterstützen.

Abstract

This thesis describes the first application of conventional magnetic resonance spectroscopic imaging (MRSI) as a validation tool for gas phase reactor models. For this purpose, techniques were developed that enable the in situ characterization of a model gas phase reaction process. These MRSI approaches allow concentration and temperature measurements inside operating catalyst beds which are considered difficult to measure by conventional, non-invasive methods. The system studied was the ethylene hydrogenation reaction catalyzed in a macroscopic nuclear magnetic resonance (NMR)-compatible fixed-bed flow reactor.

Since NMR signals from the gas phase decay very rapidly, MRSI methods are required which allow fast data acquisition after NMR excitation. Thus, a multislice NMR spectroscopic imaging approach was optimized and implemented on a 7-Tesla NMR imaging system to realize ultrashort echo time T_E. This method was used in a first approach to evaluate the applicability of MRSI to study gas phase concentrations within a packed bed reactor. The catalyst bed contained inactive γ-Al_2O_3-pellets and catalytically active Pt-Al_2O_3-pellets to enable the distinction of reactive and non-reactive zones. Spatial maps of the chemical composition could be extracted from the MRSI data sets and allowed the detection of single active catalyst pellets, as well as overall ethylene conversion. Simultaneous integral mass spectrometric (MS) measurements were in fairly good agreement with the MRSI measured concentrations.

Building on these results, the multislice approach was extended and optimized to enable 3D MRSI measurements for the investigation of concentration distributions within opaque monolithic catalysts. The model reaction was catalyzed by a Pt-coated sponge packing or a honeycomb monolith (Ø: 25 mm; L: 50 mm). The 3D MRSI measurements allowed the determination of support structure depending concentration patterns and overall reaction progress. To prove the plausibility of the MRSI data, the experimental results were compared to a 1D model of the reactor based on kinetic data from the literature. Measured and simulated concentration profiles were in good agreement. Furthermore, a comparison with simultaneously performed integral MS concentration measurements demonstrated deviations below 5 %.

Finally, concentration mapping within the monolithic catalysts was combined with simultaneously detected temperature profiles. For this purpose, specially designed ethylene glycol filled NMR multipoint thermometers were inserted into the monolithic catalysts. The analysis of the ethylene glycol spectra enabled the detection of nearly continous longitudinal temperature profiles. The results of the 3D MRSI measurements were compared to simulations of a predictive two dimensional model of the processes. Simulated and measured concentration and temperature profiles were in very good agreement, the deviations were below 9 %. Conventional MS measurements provided further evidence of the accuracy of the 3D MRSI measurements as well as of the 2D reactor model. These results demonstrate the great potential of 3D MRSI for studying heterogeneously catalyzed gas phase reactions within macroscopic tubular reactors, and supporting the development and validation of physically consistent reactor models.

Contents

1 Introduction and aim of this work
1.1 General introduction and motivation . . . 1
1.2 Aim of this work . . . 2
References . . . 2

2 Thematic background
2.1 Heterogeneously catalyzed gas phase reaction processes . . . 5
2.1.1 Packed beds . . . 6
2.1.2 Monolithic catalysts . . . 7
References . . . 8

3 Spatially resolved characterization methods for heterogeneously catalyzed gas phase reaction processes
3.1 Concentration measurements . . . 11
3.1.1 Invasive concentration measurements . . . 11
3.1.2 Non-invasive concentration measurements . . . 13
3.2 Temperature measurements . . . 13
3.2.1 Invasive temperature measurements . . . 13
3.2.2 Non-invasive temperature measurements . . . 14
3.3 Application of MRI to heterogeneous catalysis . . . 14
3.3.1 Concentration measurements . . . 15
3.3.2 Temperature measurements . . . 17
3.3.3 Velocimetry . . . 18
References . . . 18

4 Basics of 3D magnetic resonance spectroscopic imaging
4.1 Basics of nuclear magnetic resonance . . . 24
4.2 NMR tomography . . . 25
4.3 Magnetic resonance spectroscopic imaging (MRSI) . . . 26
References . . . 27

5 Experimental background
5.1 Gas phase MRSI . . . 28
5.2 Pt-catalyzed ethylene hydrogenation: The ideal benchmark reaction . . . 29
5.3 Description of the setup used for the NMR experiments with reactive flows . . . 31
References . . . 32

6 NMR imaging of gas phase reaction processes
6.1 Introduction . . . 35
6.2 Experimental . . . 36
6.2.1 Materials . . . 36
6.2.2 Temperature measurements . . . 36
6.2.3 Ethylene hydrogenation . . . 37
6.2.4 MRSI experiments . . . 38

6.3 Results and discussion . . . 39
6.3.1 Temperature measurements . . . 41
6.3.2 Gas composition measurements . . . 41
6.4 Conclusion . . . 45
References . . . 46

7 NMR imaging of gas phase reaction processes within monolithic catalyst supports
7.1 Introduction . . . 50
7.2 Experimental . . . 50
7.2.1 Materials . . . 50
7.2.2 Ethylene hydrogenation . . . 51
7.2.3 MRSI experiments . . . 52
7.2.4 Modeling approach . . . 53
7.3 Results and discussion . . . 54
7.3.1 Spatially resolved gas concentration analysis . . . 54
7.3.2 MRSI measurement and simulation of the reaction progress . . . 56
7.4 Conclusion . . . 58
References . . . 59

8 NMR based validation of modeling approaches
8.1 Introduction . . . 62
8.2 Experimental . . . 63
8.2.1 Monolithic catalysts . . . 63
8.2.2 Temperature measurements . . . 63
8.2.3 Kinetic measurements . . . 64
8.2.4 3D MRSI temperature and concentration measurements . . . 65
8.3 2D pseudo-homogeneous fixed-bed reactor model . . . 65
8.3.1 Governing balance equations . . . 65
8.3.2 Kinetic model . . . 66
8.3.3 Constitutive models and material laws . . . 66
8.3.4 Numerical solution of the balance equations . . . 68
8.4 Results and discussion . . . 68
8.4.1 Validation of temperature measurements . . . 68
8.4.2 Comparison of MRSI measured and predicted temperature profiles . . . 69
8.4.3 Comparison of MRSI measured and predicted concentration profiles . . . 71
8.5 Conclusion . . . 73
References . . . 73
A8.1 Catalyst model . . . 75
A8.2 Notation . . . 78

9 Conclusion

10 Outlook

A Appendix
A.1 Supporting information for chapter 7 . . . 83
A.1.1 Estimation of the influence of internal and external mass transport . . . 84
References . . . 87

List of Publications **89**

List of Oral and Poster Presentations **91**

1. Introduction and aim of this work

1.1. General introduction and motivation

The industrial production of many bulk and fine chemicals involve heterogeneously catalyzed gas phase processes. Particularly exothermic reactions are usually catalyzed in tubular wall cooled fixed bed reactors with diameters between 15 mm and 40 mm. Since heat can only be removed at the wall of these reactors, temperature and concentration gradients often occur in radial and longitudinal direction, and can have a major impact on process performance and reactor safety [1].

The reaction processes in these reactors are very complex and depend on characteristics such as temperature, pressure, microkinetics and thermodynamics of the reaction, heat and mass transfer properties of the catalyst bed, and the reactor itself. To reduce production costs and increase process efficiency, reaction conditions are desired which allow for kinetically and thermodynamically favorable concentration, pressure, and temperature conditions. To determine optimal operating conditions, usually mathematical models are used which describe the interactions between microscopic and macroscopic reaction processes within such reactors appropriately, and thus allow to analyze potentials for process intensification [2].

These models, however, have to be validated by comparing their simulation results with measurements of benchmark processes to prove their accuracy. Validation measurements are particularly challenging, since reaction conditions have to be measured within usually opaque and mechanically inaccessible catalytic beds. The vast majority of validation experiments are based on invasive measurement techniques. Here, physical probes are inserted into the catalytic beds to measure concentration and temperature profiles at specific positions. To achieve this, special experimental setups are required which can provide physical access to the reaction zones [3].

Particularly for gas phase processes catalyzed by monolithic catalysts, like honeycombs or sponges, often capillary-based techniques are chosen. To this end, the measuring devices are moved longitudinally through a channel of the monolithic structure. Such approaches were widely applied to study various gas phase reaction systems and validate modeling approaches [4–12]. But despite their high popularity and widespread use, invasive techniques have also several disadvantages which have to be considered: The applied probes are typically measuring a specific quantity, like temperature or concentration. Hence, simultaneous collection of temperature and concentration profiles can only be achieved if the capillary contains several suitable detectors. Furthermore, the collected spatially resolved profiles are limited to specific radial positions of the catalyst beds, particularly if a channel has to be drilled to enable the insertion of the probes. Additionally, the detected profiles can be influenced by the presence of the capillary, since the local residence times are altered [13, 14].

Thus, alternative approaches would be favorable which potentially make feasible the non-invasive characterization of optically opaque reaction systems. Such an alternative are Magnetic Resonance Imaging (MRI) methods that are based on the Nuclear Magnetic Resonance (NMR) effect. MRI has long been used to investigate the internal structure of the human body and transport processes occurring within it, and also allow thermal mapping as well as spatially resolved concentration studies within opaque structures. Consequently, these methods gained interest as characterization tools for heterogeneously catalyzed processes [15]. However, existing studies focused mainly on the investigation of 3-phase reaction systems, e.g., on octene hydrogenation and alpha-methylstyrene hydrogenation [16–19]. Here, the detected signals originated predominantly from the liquid phase.

The investigation of gas phase reaction processes is particularly challenging, since the signal intensity of gases is much lower than the signal intensity of liquids. In addition, the NMR signal of gas molecules decay very rapidly which further complicates signal detection [20]. Accordingly, gas phase reaction processes have only been studied by using NMR signal enhancement methods like hyperpolarization or remote detection techniques or a combination thereof [21–25]. Unfortunately,

these approaches restrict NMR experiments to microfluidic devices. Therefore, the NMR based investigation of gas phase processes catalyzed in industrially more relevant macroscopic reactors (Ø>20 mm) has not been demonstrated yet. Furthermore, and surprisingly, the combination of NMR based characterization and mathematical modeling is particularly rare, the validation of predictive reactor models with NMR derived measurements has not been shown so far.

1.2. Aim of this work

On the basis of the available studies of MRI applied in chemical engineering research the following questions arise and are the driving force of this thesis: "Can conventional MRI be used to investigate macroscopic gas phase reactors with monolithic catalysts, and is it possible to use the information for model validation?" To answer these questions severals objectives have to be addressed, which are described below:

The first challenge is to identify an ideal heterogeneously catalyzed gas phase process suitable as model reaction in terms of reaction conditions and NMR visibility. Then an experimental setup has to be designed and constructed that allows safe and reproducible operation of the reaction process within an NMR tomograph. In addition, MRSI methods have to be adapted to the specific challenges of gas phase MRI, and strategies for NMR signal analysis for concentration measurements have to be determined.

The second challenge focuses on the investigation of gas phase processes catalyzed by monolithic catalysts. It has to be ensured that the continuous solid structure of the monolithic catalyst supports does not deteriorate the NMR measurements due to increased magnetic field inhomogeneities induced by susceptibility differences of the different phases. Furthermore, the MRSI measurements have to provide sufficient spatial resolution, especially in longitudinal direction, to allow the analysis of the reaction progress, and to evaluate the plausibility of the results.

The third challenge aims directly at the utmost goal of this work: Model validation by MRSI based characterization. To achieve this, also the temperature boundary conditions of the reaction process have to be known to compare modeling approaches with experimental data. Therefore, temperature measurement methods have to be developed and validated that allow the parallel determination of spatially resolved concentration and temperature distributions. To compare the experimental data with simulation results of the process, a reactor model has to be employed which considers the microkinetics of the reactions as well as heat and mass transfer properties of the fixed beds of the reactor.

The conclusions obtained from addressing these challenges will provide answers to the question if and how conventional MRSI can be applied to give insights into the reaction processes occurring in catalyst beds of gas phase processes.

References

1. Andrigo, P., Bagatin, R. & Pagani, G. Fixed bed reactors. *Catalysis Today* **52,** 197–221 (1999).
2. Jakobsen, H. *Chemical Reactor Modeling* (Springer Science & Business Media, 2014).
3. Morgan, K., Touitou, J., Choi, J.-S., Coney, C., Hardacre, C., Pihl, J., Stere, C., Kim, M.-Y., Stewart, C., Goguet, A. & Partridge, W. Evolution and Enabling Capabilities of Spatially Resolved Techniques for the Characterization of Heterogeneously Catalyzed Reactions. *ACS Catalysis* **6,** 1356–1381 (2016).
4. Horn, R., Williams, K., Degenstein, N. & Schmidt, L. Syngas by catalytic partial oxidation of methane on rhodium: Mechanistic conclusions from spatially resolved measurements and numerical simulations. *Journal of Catalysis* **242,** 92–102 (2006).
5. Beretta, A., Groppi, G., Lualdi, M., Tavazzi, I. & Forzatti, P. Experimental and Modeling Analysis of Methane Partial Oxidation: Transient and Steady-State Behavior of Rh-Coated Honeycomb Monoliths. *Industrial & Engineering Chemistry Research* **48,** 3825–3836 (2009).
6. Beretta, A., Donazzi, A., Livio, D., Maestri, M., Groppi, G., Tronconi, E. & Forzatti, P. Optimal design of a CH_4 CPO-reformer with honeycomb catalyst: Combined effect of catalyst load and channel size on the surface temperature profile. *Catalysis Today* **171,** 79–83 (2011).

7. Sa, J., Fernandes, D., Aiouache, F., Goguet, A., Hardacre, C., Lundie, D., Naeem, W., Partridge, W. & Stere, C. SpaciMS: spatial and temporal operando resolution of reactions within catalytic monoliths. *Analyst* **135,** 2260–2272 (2010).
8. Forzatti, P., Lietti, L. & Gabrielli, N. A kinetic study of the reduction of NO_x stored on Pt-Ba/Al_2O_3 catalyst. *Applied Catalysis B: Environmental* **99,** 145–155 (2010).
9. Stewart, J., Douglas, R., Goguet, A., Stere, C. E. & Blades, L. *A Mathematical Approach to the Balancing of Mass Transfer and Reaction Kinetics in Dual Kinetic Model for Automotive Catalysis* tech. rep. (SAE Technical Paper, 2014).
10. Hettel, M., Diehm, C., Bonart, H. & Deutschmann, O. Numerical simulation of a structured catalytic methane reformer by DUO: The new computational interface for OpenFOAM and DETCHEM. *Catalysis Today* **258, Part 2,** 230–240 (2015).
11. Deutschmann, O. Modeling of the Interactions Between Catalytic Surfaces and Gas-Phase. *Catalysis Letters* **145,** 272–289 (2015).
12. Wehinger, G., Kraume, M., Berg, V., Korup, O., Mette, K., Schlögl, R., Behrens, M. & Horn, R. Investigating dry reforming of methane with spatial reactor profiles and particle-resolved CFD simulations. *AIChE Journal* **62,** 4436–4452 (2016).
13. Hettel, M., Diehm, C., Torkashvand, B. & Deutschmann, O. Critical evaluation of in situ probe techniques for catalytic honeycomb monoliths. *Catalysis Today* **216,** 2–10 (2013).
14. Hettel, M., Antinori, C. & Deutschmann, O. CFD Evaluation of In Situ Probe Techniques for Catalytic Honeycomb Monoliths. *Emission Control Science and Technology* **2,** 188–203 (2016).
15. Koptyug, I. in *Spectroscopic Properties of Inorganic and Organometallic Compounds: Volume 45* (eds Yarwood, J., Douthwaite, R. & Duckett, S.) 1–42 (The Royal Society of Chemistry, 2014).
16. Koptyug, I., Lysova, A., Kulikov, A., Kirillov, V., Parmon, V. & Sagdeev, R. Functional imaging and NMR spectroscopy of an operating gas-liquid-solid catalytic reactor. *Applied Catalysis A: General* **267,** 143–148 (2004).
17. Lysova, A., Koptyug, I., Kulikov, A., Kirillov, V., Sagdeev, R. & Parmon, V. Nuclear magnetic resonance imaging of an operating gas-liquid-solid catalytic fixed bed reactor. *Chemical Engineering Journal* **130,** 101–109 (2007).
18. Lysova, A., Koptyug, I., Kulikov, A., Kirillov, V. & Sagdeev, R. An NMR Imaging Study of Steady-State and Periodic Operation Modes of a Trickle Bed Reactor. *Topics in Catalysis* **52,** 1371–1380 (2009).
19. Gladden, L., Abegao, F., Dunckley, C., Holland, D., Sankey, M. & Sederman, A. MRI: Operando measurements of temperature, hydrodynamics and local reaction rate in a heterogeneous catalytic reactor. *Catalysis Today* **155,** 157–163 (2010).
20. Glover, P. & Mansfield, P. Limits to magnetic resonance microscopy. *Reports on Progress in Physics* **65,** 1489 (2002).
21. Bouchard, L., Burt, S., Anwar, M., Kovtunov, K., Koptyug, I. & Pines, A. NMR Imaging of Catalytic Hydrogenation in Microreactors with the Use of para-Hydrogen. *Science* **319,** 442–445 (2008).
22. Jarenwattananon, N., Glöggler, S., Otto, T., Melkonian, A., Morris, W., Burt, S., Yaghi, O. & Bouchard, L. Thermal maps of gases in heterogeneous reactions. *Nature* **502,** 537–540 (2013).
23. Zhivonitko, V., Telkki, V.-V. & Koptyug, I. Characterization of Microfluidic Gas Reactors Using Remote-Detection MRI and Parahydrogen-Induced Polarization. *Angewandte Chemie International Edition* **51,** 8054–8058 (2012).
24. Zhivonitko, V., Telkki, V.-V., Leppaniemi, J., Scotti, G., Franssila, S. & Koptyug, I. Remote detection NMR imaging of gas phase hydrogenation in microfluidic chips. *Lab on a Chip* **13,** 1554–1561 (2013).

25. Telkki, V.-V., Zhivonitko, V., Selent, A., Scotti, G., Leppäniemi, J., Franssila, S. & Koptyug, I. Lab-on-a-Chip Reactor Imaging with Unprecedented Chemical Resolution by Hadamard-Encoded Remote Detection NMR. *Angewandte Chemie* **126,** 11471–11475 (2014).

2. Thematic background

This chapter provides a short overview of the industrial application and process management challenges of exothermal heterogeneously catalyzed gas phase reaction processes (section 2.1). Further, it will introduce different reactor concepts suitable to catalyze these processes. Since fixed-bed reactors are presently the only reactor design option used for commercial large scale applications, section 2.1.1 will provide a description of currently applied catalyst beds in such reactors, and section 2.1.2 will introduce future options for process intensification of fixed bed reactor concepts by using monolithic catalysts.

2.1. Heterogeneously catalyzed gas phase reaction processes

Heterogeneously catalyzed gas phase reaction processes, or more specifically, reaction processes in which all reactant and product molecules inside the reaction unit are in the gas phase, represent the majority of all industrially relevant reaction processes and produce a great share of all basic intermediate or final chemicals. Examples include (de)hydrogenation reactions (cyclohexane production, selective hydrogenation of acetylene), oxidation (ethylene oxide production), addition (vinyl chloride production) and others, like the famous ammonia synthesis or flue gas purification for instance [1].

Without the use of catalysts most of these reactions would occur with very slow kinetics, if at all. Other possibilities to increase the reaction rate include the change of reaction conditions like pressure or temperature, which in turn could lead to undesirable energy consumption, mechanical stress or decrease of selectivity. Therefore, it is reasonable to introduce a second phase, here solid catalysts, to the system.

These processes are based on a variety of different reaction mechanisms. But all these mechanisms have in common that at least one reactant molecule species adsorbs at the catalytic site of the catalyst and then reacts with other reactant molecules of the gas phase or adsorbed at adjacent catalytic sites. Temperature and pressure conditions have an enormous influence on these reaction mechanisms and can decrease or increase process performance [2–4]. Reactants and catalyst material have to be brought in contact with each other inside a reaction unit, which is typically operated in continuous-flow mode to enable reliable, cost-effective and large scale production of the desired chemical substance. The reaction conditions inside the reactors, like temperature, concentration, pressure, and flow distribution, have to be kept within certain limits to maintain production efficiency. The objective of the process design is to determine reaction conditions which lead to a maximum of achievable selectivities and yields, a minimum of required catalyst space, a maximum of life time and a minimum of expenditure on energy and apparatus required for work-up compared to benchmark processes. These objectives can also be summarized as process intensification [5].

Fixed-bed reactor concepts suitable for catalyzing gas phase reactions include packed bed reactors with large diameters (adiabatic full-space reactors), multi stage reactors, and reactor concepts with a large surface/volume ratio.
Adiabatic reactor concepts are typically used if the gas phase processes either exhibit only an insignificant heat tone or can be operated autothermically. Multi stage reactors are the reactors of choice if the reactions are limited by chemical equilibrium and thus intermediate cooling or heating should be applied.

If the heterogeneously catalyzed gas phase processes are exothermic or even strongly exothermic, like in the scope of this thesis, temperature management becomes a key element of process intensification. Poor temperature management can lead to uncontrolled temperature rise in the reactor which can harm the selectivity of the catalyst and favor undesired side reactions and also can lead to activity problems by premature deactivation or sintering of the catalyst.

Applicable reactor concepts suitable for such processes should enable an efficient heat removal from the reaction zones through a large surface/ volume ratio [1]: for example micro reactors, spin-

ning disc reactors or tubular wall-cooled fixed bed reactors (Figure 2.1). Due to the high space demand, catalyst loss and irregular residence time distribution, fluidized-bed reactors are not considered here.

The former reactor concepts are characterized by extremely high specific surface areas and/or low contact times to enable particularly favorable thermal reaction conditions. However, these approaches are mainly academic, and thus limited to laboratory scale experiments [7–9]. At present, the majority of commercial heterogeneously catalyzed gas phase processes are carried out in multitubular wall-cooled fixed bed reactors. In these reactors the reactants flow through a tube loaded with a catalyst bed. All tubes are in parallel positioned inside a jacket and cooled at the outside of the tube wall with a liquid coolant, typically pressurized water, oil, or molten salt. The number of tubes inside the jacked can vary between 20 and 20000 with tube diameters of about 30 mm.

These reactors are also known as isothermal fixed bed reactors despite the fact that in reality significant temperature gradients occur in longitudinal and radial direction. These gradients, however, can have an enormous impact on the process performance as they can influence the overall heat production of the process, the microkinetics of the reaction system, the fluid properties of products and reactants, and also the thermodynamics of the reaction [1].

The performance of tubular reactors depends further on the inlet temperature and concentration, the temperature of the cooling medium, the heat production of the process, the microkinetics of the reaction system, the fluid properties of products and reactants and the heat, mass and momentum transfer characteristics of the catalyst beds.

If all these parameters are known, the behavior of the reactor can be described with mathematical models. The reliability of such models has to be validated by comparison of simulation results with experimental data to prove that the model describes the interaction between chemical reaction, and mass and heat transfer appropriately. A validated model is in turn the basis on which process intensification potentials can be determined [10].

2.1.1. Packed beds

The vast majority of multi-tubular continuous flow reactors are equipped with packed beds. Packed beds consist of numerous catalyst pellets of a certain shape, chemical composition, and diameter. Catalyst pellets vary in multiple parameters such as chemical composition of the active components, promoters and inhibitors, distribution of the active components, interaction between catalyst material and support, and microstructure of the pellet. Typical forms of catalyst pellets are sphere, cube, single ring, crossweb, pall ring, intalox saddle and many more (cf. Figure 2.2). The shape and size of the pellets depend on the desired features of the catalyst bed (e.g. active surface area per unit volume, voidage and transport coefficients). Typical tube to particle diameter ratios range from 4 to 40 [11], whereas in order to limit hot spot temperatures of extremely exothermic processes values of 4 to 5 are often chosen [1].

Packed beds are formed by dumping the catalyst pellets into the tube. The catalyst loading is crucial for the process: unstable and inefficient arrangements as well as catalyst damage have to be avoided, the pellets must be distributed evenly. In multi-tubular reactors the reproducibility and uniformity of the resulting structure of the packed bed in every tube has to be ensured, which is achieved by measuring the weight of the filled pellets and the resulting pressure drop along the tubular reactors. Both values should be maintained between 95 % and 105 % of the mean value. During operation, critical changes of the structure, such as settlement, shrinkage or structure collapse have to be monitored closely, as these phenomena can have dramatical effects on economic viability and reactor safety.

Especially bridging effects can lead to high voidage packing regions and hence local overheating during exothermic operation. Due to these effects, tube filling is an important economical aspect, and subject to significant research effort [12]. Despite the previously mentioned difficulties associated with packed beds and especially their non-optimal heat transfer characteristics, they are still the standard for wall cooled tubular reactors. Thus, momentum, heat and mass transfer characteristics of these beds are subject to research since decades. For common pellet types (ring, cylinder, hollow cylinder, etc.) these parameters are well validated [13–15]. Nevertheless, the development of new pellet types is still an ongoing process [16], which will

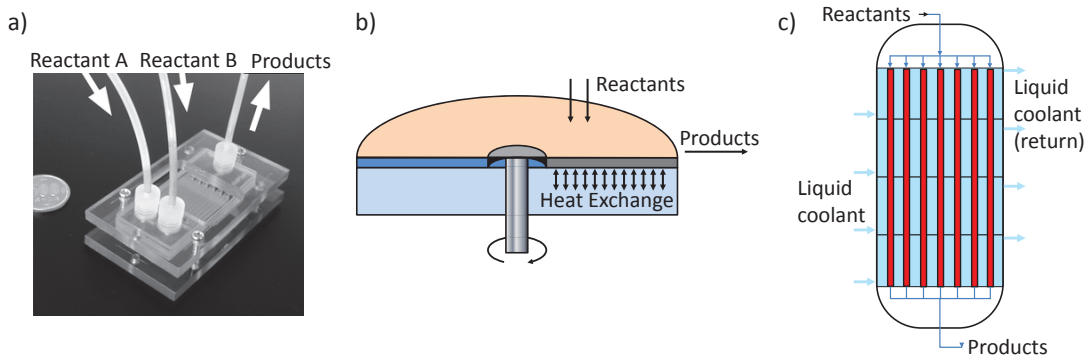

Figure 2.1.: Representation of a typical micro reactor (a), reprinted with permission from [6], schematic of a spinning disc reactor adapted from [5] on (b) and a scheme of a multi-tubular fixed bed reactor (c).

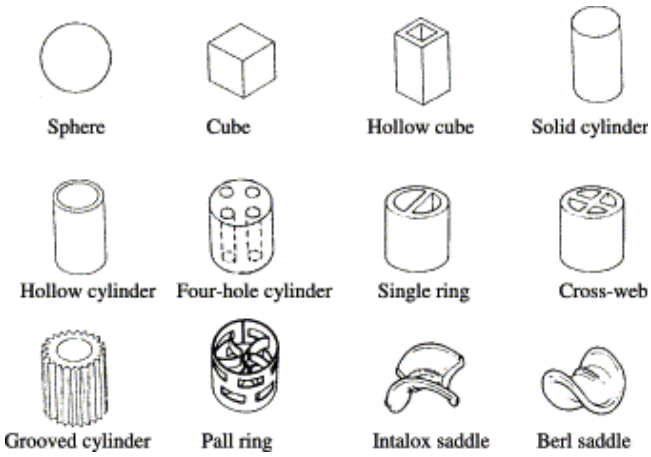

Figure 2.2.: Typical shapes of catalyst pellets used in tubular fixed-bed reactors. Reprinted with permission from [12].

make the investigation of packed beds necessary in the future, for example to adapt form factors or flattening coefficients for transfer correlations.

2.1.2. Monolithic catalysts

Another option for catalytic beds is to use monolithic catalyst supports instead of packed beds. These catalysts are usually made of metal or a ceramic material coated with a thin layer of washcoat which acts as support for the catalytically active species. Common features of these monolithic catalysts are [5]:

- low pressure drop due to a large open frontal area
- enhanced mechanical strength and structure integrity due to the continuous solid phase which allow alternative reactor configurations
- typically 1.5 to 4 times higher specific surface area compared to packed beds
- high catalyst efficiency, due to short diffusion paths

Independent of their bulk material, monolithic catalyst supports can be divided into two categories: Catalysts with channel structured supports or with open cell structured supports (cf. Figure 2.3).

Channel structured catalysts are commonly made from ceramic extrudates or flat and corrugated metal foils, which are stacked in thin layers and wowed into cylindrical or elliptical bodies. They were initially used in purifying applications, like automotive catalysis, ozone abatement in aircrafts, destruction of organic compounds of exhaust air of restaurants, and flue gas treatment of power plants [17]. These applications have in common that large volume flows have to be processed and the reactants are highly diluted by gaseous inerts. Thus, temperature management is of minor importance and mostly adiabatic reactors are applied. Nevertheless, the heat transfer characteristics of honeycomb structures are well investigated, and generally accepted heat transfer correlations are available [19, 20].

Radial dispersion is not crucial in most applications, and can only be achieved in case of metal foil honeycombs by punching out and embossing the foil materials. However, this is predominantly done to increase turbulence inside the channels [21] and does not enhance radial heat transfer properties. The adiabatic conditions inside the channels remain nearly unchanged.

To increase the heat transfer characteristics, honeycomb designs have been investigated which include large volume fractions of support made of materials with high temperature conductivities [19], but have been proven impractical due to high manufacturing and development costs and significantly

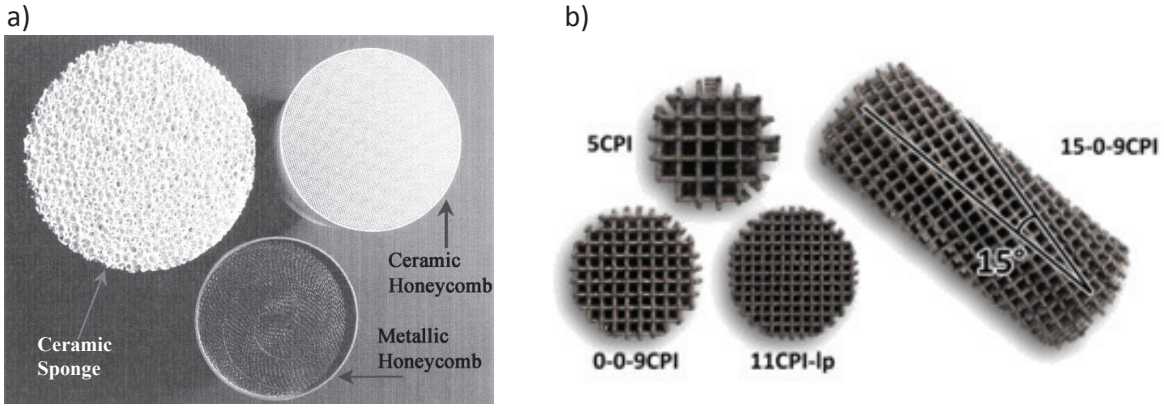

Figure 2.3.: (a) Examples of channel structured (honeycombs) and open cell structured (sponges) monolithic catalyst supports. (b) Examples of additive manufactured periodic open cellular structures with cubic cell geometry. Reprinted with permission from [17] and [18].

reduced specific surface area. Consequently, channel structured catalysts have very limited importance as catalyst beds for isothermal tubular reactors [5, 17, 22].

Open cellular structures, however, allow radial dispersion, and hence heat removal. They can be separated into two different categories: reticulated open-cell sponges with irregular structure for example produced by replica techniques [23], and periodic open cellular structures with well-defined geometries which can be produced by additive manufacturing techniques [18, 24, 25] (cf. Figure 2.3). Recently, such structures are used as heat transfer devices [26, 27], but also considered as a very promising option as catalyst supports for exothermic reactions [28, 29]. Especially catalytic sponge packings have been applied as catalyst support for various exothermic gas phase reactions, such as CO-oxidation [30, 31], several hydrogenation reactions [32–35], the oxidative coupling of methane [36], and methanation processes [37, 38]. Unanimously, improved process performance like higher space time yields and selectivities, smoother temperature distributions, and increased catalyst stability were reported, when using solid sponges compared to state-of-the-art catalyst systems, e. g. randomly packed beds. In every case, the process performances benefit from the main advantage of catalytic sponges: They allow a decoupling of thermal conductivity, which is controlled by the support and catalytic activity, controlled by the catalytic coating.

But despite the huge scientific interest, generally accepted heat and mass transfer correlations for open cellular structures are not available yet, due to the variety of possible combinations: regular or irregular structure, sprout dimensions, solid conductivity, window size and many more. This is underlined by the number of recently published papers on this subject [33, 39]. In addition, most of the correlations were derived from studies with non-reactive gaseous flows. Operando studies are quite rare which is caused by difficult accessibility of monolithic supports compared to packed beds and experimental efforts. But from the view of the author, such studies are essential to prove the validity of transfer correlations, and particularly the performance of catalyst supports under reaction conditions.

Commercial applications are only reluctantly discussed by industrial users. Currently, concerns regarding a sufficient thermal wall coupling of the open cellular structure prevent industrial use. However, a recent study could disprove this concern: Razza et al. showed that a low fraction of contact area (10 % to 20 %) is sufficient to significantly enhance heat transfer between catalyst support and cooled reactor wall [40]. Hence, open cellular structures might be the basis for future industrially scale process intensification approaches.

References

1. Andrigo, P., Bagatin, R. & Pagani, G. Fixed bed reactors. *Catalysis Today* **52,** 197–221 (1999).
2. Boudart, M., Davis, B. & Heinemann, H. in *Handbook of Heterogeneous Catalysis* (eds Ertl, G., Knözinger, H., Schüth, F.

& Weitkamp, J.) 1–48 (Wiley-VCH Verlag GmbH, 2008).

3. LePage, J., Schlögl, R., Wainwright, M., Schü, F., Unger, K., Ko, E., Jacobsen, H., Kleinschmit, P., Menon, R. G., Delmon, B., Lee, K.-Y., Misino, M. & Oyama, S. in *Handbook of Heterogeneous Catalysis* (eds Ertl, G., Knözinger, H., Schüth, F. & Weitkamp, J.) 49–138 (Wiley-VCH Verlag GmbH, 2008).
4. Levenspiel, O. *Chemical reaction engineering* (John Wiley & Sons, 1999).
5. Stankiewicz, A., Moulijn, J., *et al.* Process intensification: transforming chemical engineering. *Chemical Engineering Progress* **96,** 22–34 (2000).
6. Kikutani, Y., Hibara, A., Uchiyama, K., Hisamoto, H., Tokeshi, M. & Kitamori, T. Pile-up glass microreactor. *Lab on a Chip* **2,** 193–196 (2002).
7. Reintjens, R. & de Vries, A. Microreactors: Lessons Learned From Industrial Applications. *Chemical Engineering* **123,** 40 (2016).
8. Pennemann, H. & Kolb, G. Review: Microstructured reactors as efficient tool for the operation of selective oxidation reactions. *Catalysis Today* **278, Part 1,** 3–21 (2016).
9. Visscher, F., van der Schaaf, J., Nijhuis, T. & Schouten, J. Rotating reactors - A review. *Chemical Engineering Research and Design* **91,** 1923–1940 (2013).
10. Jakobsen, H. *Chemical Reactor Modeling* (Springer Science & Business Media, 2014).
11. Winterberg, M. & Tsotsas, E. Impact of tube-to-particle-diameter ratio on pressure drop in packed beds. *AIChE Journal* **46,** 1084–1088 (2000).
12. Afandizadeh, S. & Foumeny, E. Design of packed bed reactors: guides to catalyst shape, size, and loading selection. *Applied Thermal Engineering* **21,** 669–682 (2001).
13. Verein Deutscher Ingenieure, V.-G. V. u. C. D Thermophysikalische Stoffeigenschaften. *VDI-Wärmeatlas: Berechnungsblätter für den Wärmeübergang,* 137–686 (2006).
14. Verein Deutscher Ingenieure, V.-G. V. u. C. L Strömungsdynamik und Druckverlust. *VDI-Wärmeatlas: Berechnungsblätter für den Wärmeübergang,* 1221–1446 (2006).
15. Verein Deutscher Ingenieure, V.-G. V. u. C. M Sonderprobleme der Wärmeübertragung. *VDI-Wärmeatlas: Berechnungsblätter für den Wärmeübergang,* 1459–1569 (2006).
16. Weng, H., Luo, J., Yin, Y., Duan, Z., Sha, Y., Ye, L., Tu, S. & Lai, Y. Performance characteristics of a new spherical metal mesh packing. *Chemical Engineering and Processing: Process Intensification* **72,** 68–73 (2013).
17. Heck, R., Gulati, S. & Farrauto, R. The application of monoliths for gas phase catalytic reactions. *Chemical Engineering Journal* **82,** 149–156 (2001).
18. Klumpp, M., Inayat, A., Schwerdtfeger, J., Körner, C., Singer, R., Freund, H. & Schwieger, W. Periodic open cellular structures with ideal cubic cell geometry: Effect of porosity and cell orientation on pressure drop behavior. *Chemical Engineering Journal* **242,** 364–378 (2014).
19. Groppi, G. & Tronconi, E. Honeycomb supports with high thermal conductivity for gas/solid chemical processes. *Catalysis Today* **105,** 297–304 (2005).
20. Visconti, C., Groppi, G. & Tronconi, E. Accurate prediction of the effective radial conductivity of highly conductive honeycomb monoliths with square channels. *Chemical Engineering Journal* **223,** 224–230 (2013).
21. Downey, M., Müller-Haas, K., Park, T., Diewald, R. & Radovanovic, R. *Structured Foil Catalysts: A Road Map to Highly Effective, Compact Aftertreatment Systems* tech. rep. (SAE Technical Paper, 2007), 01–4038.
22. Zhao, C. Review on thermal transport in high porosity cellular metal foams with open cells. *International Journal of Heat and Mass Transfer* **55,** 3618–3632 (2012).
23. Luyten, J., Mullens, S., Cooymans, J., Wilde, A. D., Thijs, I. & Kemps, R. Different methods to synthesize ceramic foams. *Journal of the European Ceramic Society* **29,** 829–832 (2009).
24. Lämmerann, M., Schwieger, W. & Freund, H. Experimental investigation of gas-liquid distribution in periodic open cellular structures as potential catalyst supports. *Catalysis Today* **273,** 161–171 (2016).

25. Körner, C. Additive manufacturing of metallic components by selective electron beam melting: a review. *International Materials Reviews* **61,** 361–377 (2016).

26. Lu, T., Stone, H. & Ashby, M. Heat transfer in open-cell metal foams. *Acta Materialia* **46,** 3619–3635 (1998).

27. Banhart, J. Manufacture, characterisation and application of cellular metals and metal foams. *Progress in Materials Science* **46,** 559–632 (2001).

28. Bianchi, E., Heidig, T., Visconti, C., Groppi, G., Freund, H. & Tronconi, E. An appraisal of the heat transfer properties of metallic open-cell foams for strongly exo-/endothermic catalytic processes in tubular reactors. *Chemical Engineering Journal* **198-199,** 512–528 (2012).

29. Tronconi, E., Groppi, G. & Visconti, C. Structured catalysts for non-adiabatic applications. *Current Opinion in Chemical Engineering* **5,** 55–67 (2014).

30. Patcas, F., Garrido, G. & Kraushaar-Czarnetzki, B. CO oxidation over structured carriers: A comparison of ceramic foams, honeycombs and beads. *Chemical Engineering Science* **62,** 3984–3990 (2007).

31. Garrido, G., Patcas, F., Lang, S. & Kraushaar-Czarnetzki, B. Mass transfer and pressure drop in ceramic foams: A description for different pore sizes and porosities. *Chemical Engineering Science* **63,** 5202–5217 (2008).

32. Gräf, I., Rühl, A.-K. & Kraushaar-Czarnetzki, B. Experimental study of heat transport in catalytic sponge packings by monitoring spatial temperature profiles in a cooled-wall reactor. *Chemical Engineering Journal* **244,** 234–242 (2014).

33. Gräf, I., Ladenburger, G. & Kraushaar-Czarnetzki, B. Heat transport in catalytic sponge packings in the presence of an exothermal reaction: Characterization by 2D modeling of experiments. *Chemical Engineering Journal* **287,** 425–435 (2016).

34. Elias, Y., von Rohr, P. R., Bonrath, W., Medlock, J. & Buss, A. A porous structured reactor for hydrogenation reactions. *Chemical Engineering and Processing: Process Intensification* **95,** 175–185 (2015).

35. Lali, F. Characterization of foam catalysts as packing for tubular reactors. *Chemical Engineering and Processing: Process Intensification* **105,** 1–9 (2016).

36. Liu, H., Yang, D., Gao, R., Chen, L., Zhang, S. & Wang, X. A novel Na_2WO_4-Mn/SiC monolithic foam catalyst with improved thermal properties for the oxidative coupling of methane. *Catalysis Communications* **9,** 1302–1306 (2008).

37. Li, Y., Zhang, Q., Chai, R., Zhao, G., Cao, F., Liu, Y. & Lu, Y. Metal-foam-structured Ni-Al_2O_3 catalysts: Wet chemical etching preparation and syngas methanation performance. *Applied Catalysis A: General* **510,** 216–226 (2016).

38. Frey, M., Romero, T., Roger, A.-C. & Edouard, D. Open cell foam catalysts for CO_2 methanation: Presentation of coating procedures and in situ exothermicity reaction study by infrared thermography. *Catalysis Today* **273,** 83–90 (2016).

39. Fischedick, T., Kind, M. & Dietrich, B. Radial two-phase thermal conductivity of ceramic sponges up to high temperatures - experimental results and correlation. *International Journal of Thermal Sciences* **114,** 98–113 (2017).

40. Razza, S., Heidig, T., Bianchi, E., Groppi, G., Schwieger, W., Tronconi, E. & Freund, H. Heat transfer performance of structured catalytic reactors packed with metal foam supports: Influence of wall coupling. *Catalysis Today* **273,** 187–195 (2016).

3. Spatially resolved characterization methods for heterogeneously catalyzed gas phase reaction processes

The reaction conditions within catalytic beds are characterized by pressure, concentration, temperature, and flow conditions [1–3]. Traditional approaches investigated the impact of varying reaction conditions by equipping a conventional reactor with a catalyst bed of interest and changing the amount and concentration of reactants introduced to the reactor, the inlet pressure and the reactor temperature. The product gas is then sampled at the reactor outlet and analyzed by methods like gas chromatography (GC), mass spectrometry (MS), or Fourier Transform Infrared (FTIR) spectroscopy. The process performance can only be determined by comparing the inlet and outlet concentrations and pressures. The properties of the reaction and transfer processes inside the reactor remain unknown, the catalyst bed is treated as a black box. The knowledge obtained by this kind of "tail-end" experiments is obviously not sufficient to understand interactions between reaction, catalyst, catalyst support, reactor and process performance [4].

The profound understanding of these interactions, however, is essential to describe reaction processes with multidimensional numerical models. These modeling approaches have to be validated by comparing the simulation results with benchmark processes, since validated reactor models are indispensable for all methods for process control and process intensification which are not based on try and error approaches [1, 5]. Thus benchmark processes should provide as much spatially resolved information about the reaction conditions as possible.

Consequently, measurement techniques and reactor designs were developed over the last years which allowed spatially resolved characterization of heterogeneously catalyzed gas phase processes. These measurements are focusing on the determination of local concentration and temperature conditions [1], and thus will be discussed in the subsequent sections. The measurement of pressure distributions within the catalyst bed under reaction conditions is of minor interest, since it can be determined from pressure drop characteristics of the catalyst bed, inlet pressure, flow rate, temperature and concentration conditions. Velocimetry within operating catalyst beds, however, would be of more interest, but can recently only be applied to a very limited degree. Nevertheless, it will be discussed in context of section 3.3.

3.1. Concentration measurements

3.1.1. Invasive concentration measurements

The most common techniques which can provide spatially resolved concentration measurements are in situ probe techniques. One of the first reactors which enabled this kind of spatial concentration measurements was presented by Baiker et al. in the mid 1980s to describe the hydrogenation of toluene using industrial catalysts in a non-isothermal non-adiabatic continuous flow fixed bed reactor [6–8]. They achieved concentration measurements within the reactor by analyzing the gas composition at fixed positions with a network of IR-analyzer probes and additional GC measurements at the inlet and outlet area of the reactor (cf. Figure 3.1).

Nevertheless, this approach has also some disadvantages: The achievable spatial resolution is rather low for installation reasons alone. A certain distance between two adjacent measuring positions has to be taken into account. In addition, the reactor has to provide multiple sample locations which is not the case in industrial reactors and may alter the reaction conditions.

Sampling techniques which could provide nearly continuous longitudinal concentration profiles were developed in the late 1990s by Partridge et al. to study exhaust emission processes within honeycomb monoliths [9]. Initially, measurements were achieved by inserting a capillary into a channel of the catalyst which sucked gas into a probe followed

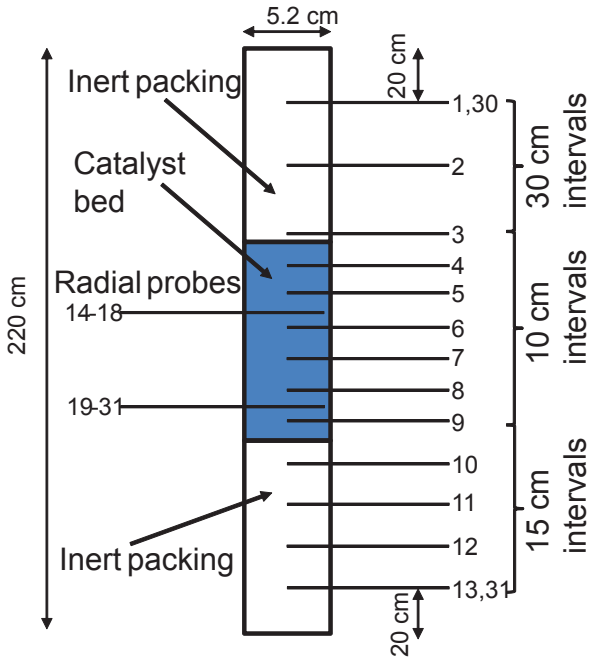

Figure 3.1.: Illustration of the reactor used by Baiker et al. to measure spatially resolved axial and radial concentration and temperature profiles. The reactor concept allowed to insert physical probe measuring devices at different axial (1–13, 30–31) and radial (14–23) positions within the catalyst bed and the inert packing. Locations 1 to 23 correspond to the thermocouples and IR-analyzer sampling probes, while 30 and 31 are the GC sampling probes. This drawing is interpreted and adapted with permission from [6].

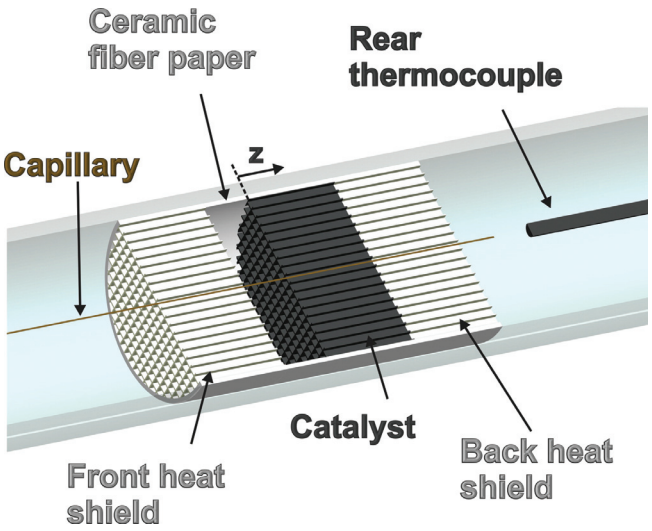

Figure 3.2.: Sketch of a typical capillary system to collect spatially resolved concentration and temperature data. Reprinted with permission from [17].

by analysis with mass spectrometers (SpaciMS). The probe capillary could be moved stepwise in axial direction, and thus enabled determination of nearly continuous longitudinal concentration profiles (cf. Figure 3.2). Later this approach was also combined with gas chromatography (Spaci-GC) and FTIR spectroscopy (Spaci-IR) [10]. The latter is a suitable alternative to investigate NO_x reduction reactions (SCR), since NH_3, N_2O, NO and NO_2 have fairly intense and easily differentiable absorption bands, and thus reduces calibration effort compared to MS and GC methods. But this approach is generally limited to operation conditions near ambient pressure, and the gas sample required for analysis is considerably higher than for MS and GC systems. Consequently, MS and GC measurements are still the methods of choice [1], and are more frequently used to investigate reaction processes within monolithic catalysts, such as SCR, partial oxidation of methane and ethylene, or CO oxidation [11–16].

Horn et al. [18–21] developed a related technique which also uses a capillary system but with a caped end and a sidewards oriented sampling orifice. The capillary can be inserted in a packed bed or in a hole drilled through the open cellular irregularly structured monolithic catalyst. In the latter case, the drilled channel has only a slightly larger diameter than the capillary (∼0.8 mm). The orientation of the sampling orifices should avoid blocking of the capillary, and, in contrast to Spaci-MS/IR approaches, the capillary keeps the channel filled at any time. This should avoid gas bypassing and maintain stable flow conditions. The lateral position of the sampling orifice can be moved with µm resolution by means of a stepper motor. Rotatory movement of the capillary is also possible to enable different sampling orifice orientations.

In addition to conventional concentration measurements with a mass spectrometer the system can also be equipped with optical sensors to allow Raman spectroscopy for the analysis of catalytic surface species and deposits [22, 23]. Continuous improvement of the reactor design allows concentration profile measurements at temperatures up to 1300 °C and pressures up to 45 bar [21].

Despite the widespread application of suction probe techniques for characterization of various reaction processes like oxidative dehydrogenation of ethane, dry reforming of methane, or partial oxidation of methane, and model validation [11, 13, 18, 24–29], their invasive nature disturbs the local flow conditions: on the one hand a small amount of gas is sucked in at the capillary orifice, on the other hand the capillary blocks a share of the cat-

alyst bed which can lead to an alternation of the local residence time [5, 17]. This can lead to a bias of the measured concentration profile which has to be considered. Hence, alternative non-invasive concentration measurements are highly desirable.

3.1.2. Non-invasive concentration measurements

Non-invasive concentration measurements are usually based on optical methods like laser induced fluorescence (LIF) (partial methane oxidation and SCR, [30, 31]) or IR spectroscopy (oligomerization of 4-fluorostyrene, hydrogenation of benzene, [32, 33]). However, the reactors used for these experiments have to provide access for the electromagnetic radiation. Thus, specially designed reactors with optical access windows have to be applied, which differ significantly from industrially used tubular continuous flow reactors. In addition, some of these methods can lead to a considerable energy input into the gas phase which in turn can change the local reaction conditions and make the concentration measurements invasive. Moreover, these methods may not resolve spatial properties along the line of sight, but rather provide bulk averaged information. Hence, they are more suitable to investigate microkinetic phenomena like reaction intermediates or active surface species but not to analyze concentration profiles inside opaque catalyst beds of tubular continuous flow reactors under reaction conditions.

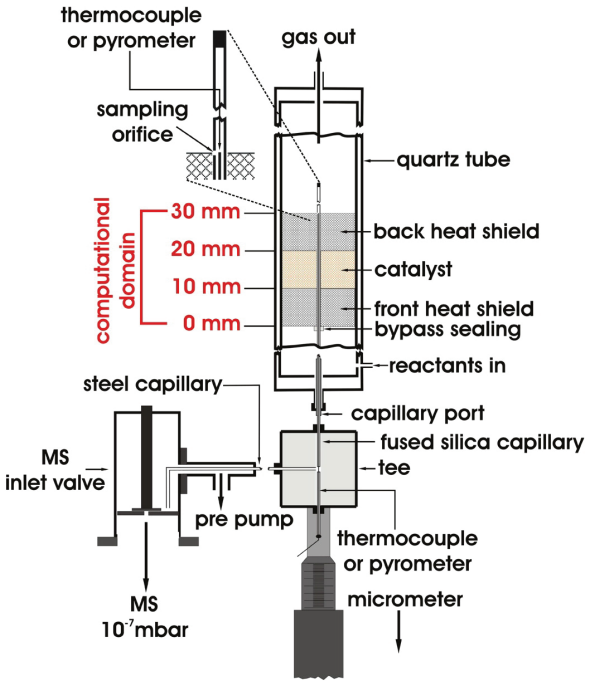

Figure 3.3.: Schematic representation of a reactor system developed by Horn et al. The setup allows to resolve species and temperature distributions within a monolithic sponge catalyst showing the location of the different elements of the system. Reprinted with permission from ref [41]. An enhanced version of this reactor enabled measurements at temperatures up to 1300 °C and pressures up to 45 bar [21].

3.2. Temperature measurements

3.2.1. Invasive temperature measurements

To monitor radial and axial temperature profiles within continuous flow reactors the oldest and most commonly applied method is to insert a network of physical probes radially into the catalyst bed at various positions (cf. Figure 3.1). Thermocouples and IR thermometers are typically applied in this kind of reactor. As already mentioned in section 3.1 Baiker et al. were the first to use such a concept to investigate dynamic reaction processes within a fixed bed reactor [6–8]. Since then, this straightforward approach has been adopted in numerous studies, but was usually only combined with integral concentration measurements at the reactor's outlet [34–39].

However, in addition to the disadvantages of this sampling concept mentioned earlier, the insertion of physical probes induce a disturbance. The disturbance can manifest itself as the difference between the measured temperature and the temperature which would occur in the absence of instrumentation. Furthermore, temperature measurements can be distorted by thermal conduction of the sensor itself and its supports as well as radiative heat transfer between sensor and its surrounding. Thus by applying this method, the accuracy and reliability of the measured data have to be considered carefully. Improvements of this approach can most likely be achieved by reducing the size of the probes.

In the context of the development of suction probe techniques, comparable temperature measurement techniques were developed and applied for various gas phase reactions (cf. section 3.1). Here, physical temperature sensors are moved translatory through fixed beds, like honeycomb monoliths [15, 24, 25], packed beds [23, 29], and catalytic sponges [20, 21, 40] at a constant radial position (cf. Figure 3.3). However, in case of catalytic sponges, a channel has to be drilled through the structure to enable the insertion of the probes.

As thermometers, typically thermocouples and pyrometers are both applied due to their complementary properties [15, 21, 24, 25]: Pyrometers sense thermal radiation from the solid catalyst, whereas the sensing tips of thermocouples are often not in direct contact with the catalyst but with the gas flow, and thus are more sensitive towards the gas temperature [40]. However, it has to be mentioned that conduction errors in thermocouple measurements can lead to high measurement uncertainties if the thermocouple body is subject to significant temperature gradients which depend on the orientation of the thermocouple, for instance upstream or downstream [24].

Spatially resolved temperature measurements without moving the sensor system or using sensor network is possible by employing fiber Bragg grating (FBG) and optical frequency domain reflectometry (OFDR). These methods are based on the spectral analysis of backscattered light along the optical fiber length. Nguyen et al. [42, 43] employed a commercial OFDR system to study longitudinal temperature profiles in a NH_3 oxidation process and in a C_3H_6 oxidation process inside a honeycomb catalyst. The spatial resolution was about 3 mm with a temporal resolution of ca. 0.9 Hz. This technique appears to be favorable, since no translatory movement is required during the measurement, but care must be taken to ensure a strain free insertion of the sensor, since fiber strain can cause equivalent displacement and lead to a corruption of the temperature measurement. In addition, neither has the OFDR technique been used to validate modeling approaches nor has the combination of OFDR and concentration measurements been demonstrated yet.

3.2.2. Non-invasive temperature measurements

The most commonly applied method to measure temperature profiles of catalyst beds non-invasively is infrared thermography (IR). Here, a measurement device detects electromagnetic radiation (detection band: typically 0.7 µm to 10 µm) of an observed object. The detected radiation is used to calculate the temperature based on Planck's law of black body radiation. This technique has been applied to analyze temperature profiles of several gas phase processes which were for example catalyzed by single channels (hydrocarbon reforming reactions and CO oxidation, [44, 45]), catalytic plate reactors (CO methanation,[46]), and catalytic sponges (CO_2 methanation, [47]).

However, it must be pointed out that these methods can only measure superficial temperatures, and are subject to the same restrictions as non-invasive concentration measurement methods. Thus, the value of these techniques to study temperature profiles within opaque porous catalyst beds of real world reactors is rather limited.

Other non-invasive temperature measurement methods, like Laser induced fluorescence, absorption and emission spectroscopy or Rayleigh and Raman scattering are more likely to be used to study non-reactant flows and combustion processes [3, 48–50].

3.3. Application of MRI to heterogeneous catalysis

Over the last decades Magnetic Resonance Imaging has become one of the most important imaging method for medical diagnostics and research, despite its obvious limitations. These include, for instance, modest spatial resolution, and the inapplicability to study samples with a high amount of ferromagnetic material compared to other tomography methods, e.g. X-ray tomography or positron emission tomography. But in contrast to the latter methods, MRI is not a highly specialized tool for morphological studies, but rather a versatile toolkit that also contains tools for angiography, thermometry, spectroscopy, functional MRI and many more [51]. Furthermore, it is the only method that allows a non-invasive holistic characterization of the state of internal organs and various processes in a human body.

Surprisingly, the chemical engineering community profits only slightly from the progress of medical MRI based diagnostics. Only a few research groups are trying to establish MRI as a characterization tool to measure reaction processes within reactors spatially resolved and non-invasively. Particularly studies on heterogeneously catalyzed gas phase processes are quite rare. This might be explained by the following aspects which have hampered a wider usage of MRI in chemical engineering: First of all, a researcher with a chemical engineering background interested in applying MRI has to get access to appropriate equipment and know-how. Although suitable NMR imaging systems, for example tomographs of the Bruker's BioSpec series, are widely available, they are predominantly used in biomedical research facilities.

Chemical engineering research groups with access to NMR imaging systems do exist, but they are rather the exception than the rule.

If this preliminary obstacle is overcome, an experimental setup has to be constructed that on the one hand meets the requirements of an NMR tomograph, and on the other hand allows reaction conditions comparable to conventional reactors. For instance, bulk metallic materials have to be avoided as construction materials, because even if non-magnetic, the magnetic field gradients of the MRI system would induce eddy currents in any electrically conductive material which would distort the homogeneity of the magnetic field and make MRI experiments impossible. In addition, when dealing with highly exothermic processes, as it was the case in this work, the MRI hardware has to be protected from high temperatures, as well as from accidental damage. These requirements, however, can be met: at lower pressures, specially designed glass reactors with appropriate temperature control devices have already been applied [52–54]. Recently, also tubular continuous flow reactors became commercially available (Ø≈20 mm) that allow MRI investigations at elevated temperatures and pressures (up to 350 °C and 30 bar, cf. [55]). This proves that MRI can also be used to study reaction processes at industrially relevant operating conditions.

Since the framing experimental conditions and challenges have been explained, the following sections will give an overview on MRI of operating chemical reactors.

3.3.1. Concentration measurements

By applying magnetic resonance spectroscopic imaging methods, it is possible to obtain spatially resolved information about the product and reactant distribution within a reactor, and thus characterize a process regarding conversion and selectivity. The methods used in those studies usually yield a separate NMR spectrum in every detected voxel which make the experiments very time consuming (for further explanation see section 4.3). The measurement time can only be decreased by decreasing the spatial resolution within the FOV or by just measuring in a small number of selected volume elements of the sample. This approach is called volume-selective NMR spectroscopy (VOSY). The first study which demonstrated the ^{1}H MRSI based mapping of chemical conversion of a heterogeneously catalyzed reaction occurring within a fixed-bed reactor was presented by Yuen et al. in 2002 [56]. Their model reaction was the liquid-phase esterification of methanol and acetic acid catalyzed by a fixed-bed of catalyst particles made of acidic ion exchange resin. The experiments were performed at ambient temperature and pressure conditions. They used both strategies to reduce the measurement time by just measuring one spatial coordinate along the bed axis (128 increments over 13 mm length of the fixed bed, data acquisition time: 3 min) or applying VOSY measurements with 30 selected volume elements (spatial resolution: 1.5 mm × 1.5 mm × 0.5 mm; data acquisition time: 3 min). In a follow-up study they combined MRI-based detection of chemical conversion of the same process with lattice-Boltzmann (LB) predictions of the flow field within the fixed-bed reactor to explore dependencies of local conversion with locally averaged fluid velocities [57]. The LB approach, however, just determined the superficial flow pattern, but did not incorporate mass transfer and chemical reaction.

Later, Koptyug et al. also demonstrated the investigation of 3-phase systems like α-methyl styrene hydrogenation and 1-octene hydrogenation, in each case catalyzed by a packed bed and at elevated temperature and ambient pressure conditions [51, 54, 58–60]. Here, measurements were performed along two spatial directions [58, 59] (spatial resolution: 230 µm × 140 µm; slice thickness: 2 mm; data acquisition time: 34 s) within a central slice of the catalyst bed, and spatially resolved spectroscopic studies [59] (spatial resolution: 1.3 mm × 0.66 mm; slice thickness: 2 mm; data acquisition time: 22.5 min), as well as multislice 2D measurements [60] (spatial resolution: down to 163 µm × 364 µm; 5 slices; slice thickness: 1 mm; data acquisition time: 8.4 s) to map the conversion progress.

On the basis of the same model reaction, Kirillov and Koptyug demonstrated the first combination of MRI and modeling of a chemical reaction process: They monitored self-oscillations of the liquid fraction within a partially wetted and continuously irrigated catalyst pellet in exothermic α-methyl styrene hydrogenation by means of MRI (spatial resolution: 230 µm × 140 µm; slice thickness: 2 mm; data acquisition time: 34 s), and explained the phenomena with physical and mathematical models of the process [61].

Also the ^{1}H MRI based monitoring of conversion and product distribution of an ethylene oligo-

merization process at elevated temperatures (100 °C – 200 °C) and pressures (∼28 bar) has been demonstrated with a novel reactor concept capable of operating reactions at elevated pressures and temperatures within NMR imaging systems [55].

However, the ^{1}H NMR spectra of liquids in porous materials often suffer from line broadening due to magnetic field inhomogeneities induced by the magnetic susceptibility differences between different phases (solid, liquid, and gas) [51]. This effect can cause overlapping of different spectral components, and thus can make signal separation and consequently also component quantification impossible. In some studies, this problem was solved by applying ^{13}C spectrometry instead of the detection of ^{1}H nuclei [53, 62, 63]. Here, signal separation is facilitated, since the chemical shift range of ^{13}C NMR is at least one order of magnitude larger than for ^{1}H NMR. Nevertheless, ^{13}C NMR involves an unavoidable loss in signal-to-noise ratio (SNR), due to a four-fold lower gyromagnetic ratio, but also because of the minor natural abundance of the ^{13}C isotope. Such dramatic loss in sensitivity can be avoided by using ^{13}C-enriched compounds in the experiments. However, the amounts that one would need to feed continuous flow reactors for a reasonable period of time would be unacceptably expensive.

Nevertheless, in all the experiments mentioned above, the NMR signal was only or at least predominantly [55] measured in the liquid phase. Measuring ^{1}H NMR spectra of a gas phase is even more challenging since gases exhibit a significantly lower signal intensity due to a lower spin density (factor ∼1000), especially at ambient pressure and elevated temperatures. In addition, the spin-spin relaxation times T_2 of gases are rather short, which further decreases the SNR and complicates signal detection [64]. Thus MRI based approaches for addressing heterogeneously catalyzed gas-phase reactions typically use signal enhancement techniques. These techniques rely mainly on two different approaches: remote detection and hyperpolarization.

In remote detection approaches, encoding and detection parts of the NMR method are separated: spectral, spatial or dynamic information of the fluid molecules are encoded by a large radio frequency (RF) coil around a reactor, while the information is read out by a microsolenoid wound around the outlet tubing when the fluid flows out [51, 65]. Due to the decreasing of the size of the detector RF coil, the specific sensitivity can be increased significantly [66, 67]. With this technique, the gas phase propene hydrogenation catalyzed by micro reactors was analyzed regarding conversion and fluid flow [65, 68] (spatial resolution: down to 0.5 mm × 1.75 mm; data acquisition time: down to 2 h 44 min).

Hyperpolarization techniques rely on the attempt to maximize the polarization of nuclear spins in a magnetic field, thereby providing gains in NMR sensitivity by more than 4 orders of magnitude [69]. To visualize heterogeneously catalyzed gas phase processes that involve hydrogen conversion, parahydrogen-induced polarization (PHIP, or PASADENA) is particularly suitable. Here, normal hydrogen, which consists at room temperature and thermal equilibrium of a 3:1 mixture of two different species, orthohydrogen and parahydrogen, is converted into parahydrogen enriched hydrogen (p-H_2). This is achieved by passing hydrogen through an ortho/para conversion catalyst held at cryogenic temperatures [69, 70]. p-H_2 gives no NMR signal by itself, but if the protons of p-H_2 participate in a suitable chemical reaction in which they become magnetically inequivalent, strong observable magnetization can be produced with signal enhancements up to a factor of 10,000 [71].

The combination of PHIP and MRI has already been used to study gas reactions in model reactors: Bouchard et al. studied hydrogenation of propylene with p-H_2 catalyzed in a tubular micro reactor (Ø≈1.6 mm). The process yields p-H_2 polarized propane with an hyperintense NMR signal. Due to signal enhancement by a factor of ∼300 compared to thermal polarization, it enabled the mapping of active regions and flow patterns of p-H_2–polarized propane in the catalyst bed [72] (spatial resolution: 20 µm × 60 µm) . Zhivonitko et al. [73] combined the hyperpolarization approach with remote detection to study the same reaction. The combination of both techniques lead to a signal enhancement factor of $\sim 5 \cdot 10^4$ compared to conventional MRI, and allowed the visualization of the reaction progress even within smaller tubular micro reactors (Ø: 150 µm to 800 µm; L: 5 mm to 15 mm; spatial resolution down to: 160 µm × 620 µm; data acquisition time: 13 min) than with other signal enhancement approaches. Here, also MRI and mathematical modeling was combined: They fitted a theoretical equation for the reaction yield based on a 1D plug-flow reactor model

to the experimentally determined reaction yields. The fitted models described the measured reaction yields reasonably well, the best agreement being achieved for smaller reactor sizes and lower reaction yields.

However, remote detection and hyperpolarization techniques or combinations thereof are of particular interest for micro reactors and experiments to investigate kinetic phenomena. If reaction processes within fixed beds of macroscopic scale (Ø>20 mm) should be studied, these techniques are less suitable: The size of macroscopic reactors limits the benefits of remote detection, and the product gas molecules are quickly loosing their hyperpolarization properties due to unavoidable relaxation processes [72, 73], and thus restricts the application to systems with rather short residence times.

3.3.2. Temperature measurements

NMR based temperature measurements can in principle be achieved by measuring the variation of relaxation times, the molecular self-diffusion coefficients, the resonance frequency of specific species within the sample or by determining temperature induced equilibrium magnetization decrease [74]. Unfortunately, these four mentioned characteristics can also be influenced drastically by chemical conversion processes, even if the temperature conditions remain unchanged. This complicates NMR based temperature measurements in chemical reactors significantly compared to thermometry in biological tissues.

Gladden et al. overcame this problem by filling liquids with temperature sensitive NMR properties into small non-metallic and impermeable containers that could be inserted into a packed bed [53]. Here, four gas bubbles were filled with ethylene glycol which were distributed along the cental axis of a packed bed. Ethylene glycol is assumed to be an ideal NMR thermometer, since the resonance frequency shift of the ^{1}H spectra of ethylene glycol allows temperature determination in the range of 310 K to 438 K [75, 76] without the need for any calibration. Gladden et al. used this technique to evaluate the local temperatures (measurement uncertainty: ± 2 °C; data acquisition time: 132 s) during the hydrogenation of 1-octene by applying volume selective ^{1}H spectroscopy. Although this method is invasive and just provides a very coarse spatial resolution, it has the advantage of remote temperature detection in opaque media: Neither optical nor mechanical access is needed. Nevertheless, just the temperature of a comparably large foreign object inside the packed bed is measured which might be quite different from the temperatures of the reactive areas. In addition, the measurement range is not very large ($\Delta T \approx$130 K [76]).

Koptyug et al. presented another NMR based thermometry technique. They exploited that the spin-lattice relaxation and the signal intensity of solid ^{27}Al nuclei is temperature dependent [77]. Based on this approach, they developed measurement techniques that allowed for quantitative temperature mapping of the solid temperature of Al_2O_3 supported catalysts during propylene hydrogenation and hydrogen oxidation [78, 79]. This approach is very promising, as it does not need any additional sensors, and is based on ^{27}Al that occurs commonly in the solid phase of heterogeneously catalyzed processes. Thus, it can potentially reveal the actual temperature conditions, e.g. temperature gradients or hot spots, in operating catalytic reactors. Nevertheless, it has to be mentioned that additional equipment, like ^{27}Al RF coils, is needed to perform the measurements. Additionally, independent calibration measurements have to to be performed to relate the measured ^{27}Al NMR signal intensity to actual temperatures. And, although temperature measurements up to 700 K were performed (spatial resolution: 0.4 mm × 0.4 mm; data acquisition time: 21 min), measurement uncertainties of more than 30 K were noticed, due to an overall decrease of signal intensity with increasing temperature.

In 2013, Jarenwattananon et al. presented a thermometry approach which can derive temperature information directly from the gas phase of a heterogeneously catalyzed process [80, 81]. They stated that in presence of an additional read out magnetic field gradient the peak width of a gas phase signal decreases with increasing temperature. This effect was used to calculate temperature maps of a propylene hydrogenation process catalyzed in a micro reactor (spatial resolution: 0.73 mm × 0.7 mm; data acquisition time: 30 min). Here, signal enhancement was achieved by using para-state-enriched hydrogen. This method seems to be an attractive option, but an application of this method with "conventional" thermally polarized gases failed in self-conducted experiments (data not shown). Thus, this approach might be limited to experiments which employ hyperpolar-

ization techniques, and hence with rather low residence times of the gas molecules. Furthermore, calibration measurements are needed to relate gradient strength, peak width and temperature. And finally, the theory behind this peak decreasing effect is apparently not fully elucidated and is recently subject to debate [82–84].

As concluding remark it should be mentioned that the combination of NMR based thermometry and mathematical modeling has not been demonstrated yet.

3.3.3. Velocimetry

Conventional velocimetry techniques are not well suited to investigate flow patterns of reactive flows in opaque porous structures. Hot film anemometry, for instance, is invasive and measures the heat transfer from a sensor exposed to fluid motion. Thus it alters the flow conditions within the structures under investigation, and will interpret detected heat alterations always as velocity changes which makes the technique inapplicable in operating catalyst beds [4].

Optical methods, e. g. Laser doppler anemometry, particle image velocimetry or molecular tagging velocimetry, can only be applied to analyze gas flows in micro channels and translucent porous structures [2, 85, 86]. Other methods, such as the radio active particle tracking technique have been used to investigate gas-fluidized beds and spouted beds, but to the authors knowledge not to study gas flows through opaque porous structures [87].

So far the only option to study gas flows inside opaque catalyst beds appear to be magnetic resonance velocimetry (MRV). Conventionally used in medical diagnostics to investigate physiologic flows in biological structures like blood vessels, MRV can also be applied to gas flows in model reactors. Thus some studies already demonstrated MRV based investigations of gas flows in porous structures: Koptyug et. al demonstrated the feasibility of MRV-based velocity mapping inside honeycomb channels by employing thermally polarized gases (propane, acetylene, butane; Re numbers: 190-570) with a resolution of 400 µm with reasonable data acquisition times (20-90 min) [88, 89]. Gladden et al. investigated gaseous SF_6 flows through a packed bed which consisted of glass spheres 5 mm diameter (max. resolution: 350 µm × 350 µm × 1.5 mm; data acquisition time: 19 min; Re number ∼290) [90], and honeycomb monoliths (channel diameter ∼1 mm; max. resolution: 140 µm × 140 µm × 12 mm; data acquisition time: 14 min; Re numbers: 106-428) [91]. But the application of MRV to reactive flows have not been addressed yet, and is still an open question.

References

1. Morgan, K., Touitou, J., Choi, J.-S., Coney, C., Hardacre, C., Pihl, J., Stere, C., Kim, M.-Y., Stewart, C., Goguet, A. & Partridge, W. Evolution and Enabling Capabilities of Spatially Resolved Techniques for the Characterization of Heterogeneously Catalyzed Reactions. *ACS Catalysis* **6,** 1356–1381 (2016).
2. Morini, G. L., Yang, Y., Chalabi, H. & Lorenzini, M. A critical review of the measurement techniques for the analysis of gas microflows through microchannels. *Experimental Thermal and Fluid Science* **35,** 849–865 (2011).
3. Childs, P., Greenwood, J. & Long, C. Review of temperature measurement. *Review of Scientific Instruments* **71,** 2959–2978 (2000).
4. Jakobsen, H. *Chemical Reactor Modeling* (Springer Science & Business Media, 2014).
5. Hettel, M., Antinori, C. & Deutschmann, O. CFD Evaluation of In Situ Probe Techniques for Catalytic Honeycomb Monoliths. *Emission Control Science and Technology* **2,** 188–203 (2016).
6. Baiker, A. & Bergougnan, M. Investigation of a fixed-bed pilot plant reactor by dynamic experimentation. Part 1. Apparatus and experimental results. *The Canadian Journal of Chemical Engineering* **63,** 138–145 (1985).
7. Baiker, A. & Bergougnan, M. Investigation of a fixed-bed pilot plant reactor by dynamic experimentation. Part 2. Simulation of reactor behaviour. *The Canadian Journal of Chemical Engineering* **63,** 146–154 (1985).
8. Baiker, A. & Epple, D. Simple method for the modelling of the behaviour of a non-isothermal, non-adiabatic fixed-bed catalytic reactor. *Applied catalysis* **22,** 55–69 (1986).
9. Partridge, W., Storey, J., Lewis, S., Smithwick, R., DeVault, G., Cunningham, M., Currier, N. & Yonushonis, T. *Time-Resolved Measurements of Emission Transients By Mass Spectrometry* tech. rep. (SAE Technical Paper, 2000).

10. Luo, J.-Y., Hou, X., Wijayakoon, P., Schmieg, S., Li, W. & Epling, W. Spatially resolving SCR reactions over a Fe/zeolite catalyst. *Applied Catalysis B: Environmental* **102,** 110–119 (2011).

11. Sa, J., Fernandes, D., Aiouache, F., Goguet, A., Hardacre, C., Lundie, D., Naeem, W., Partridge, W. & Stere, C. SpaciMS: spatial and temporal operando resolution of reactions within catalytic monoliths. *Analyst* **135,** 2260–2272 (2010).

12. Michael, B., Nare, D. & Schmidt, L. Catalytic partial oxidation of ethane to ethylene and syngas over Rh and Pt coated monoliths: Spatial profiles of temperature and composition. *Chemical Engineering Science* **65,** 3893–3902 (2010).

13. Forzatti, P., Lietti, L. & Gabrielli, N. A kinetic study of the reduction of NO_x stored on Pt-Ba/Al_2O_3 catalyst. *Applied Catalysis B: Environmental* **99,** 145–155 (2010).

14. Easterling, V., Ji, Y., Crocker, M., Dearth, M. & McCabe, R. Application of spaciMS to the study of ammonia formation in lean NOx trap catalysts. *Applied Catalysis B: Environmental* **123-124,** 339–350 (2012).

15. Diehm, C. & Deutschmann, O. Hydrogen production by catalytic partial oxidation of methane over staged Pd/Rh coated monoliths: Spatially resolved concentration and temperature profiles. *International Journal of Hydrogen Energy* **39,** 17998–18004 (2014).

16. Bugosh, G., Easterling, V., Rusakova, I. & Harold, M. Anomalous steady-state and spatio-temporal features of methane oxidation on Pt/Pd/Al_2O_3 monolith spanning lean and rich conditions. *Applied Catalysis B: Environmental* **165,** 68–78 (2015).

17. Hettel, M., Diehm, C., Torkashvand, B. & Deutschmann, O. Critical evaluation of in situ probe techniques for catalytic honeycomb monoliths. *Catalysis Today* **216,** 2–10 (2013).

18. Horn, R., Williams, K., Degenstein, N. & Schmidt, L. Syngas by catalytic partial oxidation of methane on rhodium: Mechanistic conclusions from spatially resolved measurements and numerical simulations. *Journal of Catalysis* **242,** 92–102 (2006).

19. Horn, R., Degenstein, N., Williams, K. & Schmidt, L. Spatial and temporal profiles in millisecond partial oxidation processes. *Catalysis Letters* **110,** 169–178 (2006).

20. Horn, R., Williams, K., Degenstein, N., Bitsch-Larsen, A., Nogare, D., Tupy, S. & Schmidt, L. Methane catalytic partial oxidation on autothermal Rh and Pt foam catalysts: Oxidation and reforming zones, transport effects, and approach to thermodynamic equilibrium. *Journal of Catalysis* **249,** 380–393 (2007).

21. Horn, R., Korup, O., Geske, M., Zavyalova, U., Oprea, I. & Schlögl, R. Reactor for in situ measurements of spatially resolved kinetic data in heterogeneous catalysis. *Review of Scientific Instruments* **81,** 064102 (2010).

22. Korup, O., Schlögl, R. & Horn, R. Carbon formation in catalytic partial oxidation of methane on platinum: Model studies on a polycrystalline Pt foil. *Catalysis Today* **181,** 177–183 (2012).

23. Geske, M., Korup, O. & Horn, R. Resolving kinetics and dynamics of a catalytic reaction inside a fixed bed reactor by combined kinetic and spectroscopic profiling. *Catalysis Science & Technology* **3,** 169–175 (2013).

24. Beretta, A., Groppi, G., Lualdi, M., Tavazzi, I. & Forzatti, P. Experimental and Modeling Analysis of Methane Partial Oxidation: Transient and Steady-State Behavior of Rh-Coated Honeycomb Monoliths. *Industrial & Engineering Chemistry Research* **48,** 3825–3836 (2009).

25. Beretta, A., Donazzi, A., Livio, D., Maestri, M., Groppi, G., Tronconi, E. & Forzatti, P. Optimal design of a CH_4 CPO-reformer with honeycomb catalyst: Combined effect of catalyst load and channel size on the surface temperature profile. *Catalysis Today* **171,** 79–83 (2011).

26. Stewart, J., Douglas, R., Goguet, A., Stere, C. E. & Blades, L. *A Mathematical Approach to the Balancing of Mass Transfer and Reaction Kinetics in Dual Kinetic Model for Automotive Catalysis* tech. rep. (SAE Technical Paper, 2014).

27. Hettel, M., Diehm, C., Bonart, H. & Deutschmann, O. Numerical simulation of a structured catalytic methane reformer by DUO: The new computational interface for OpenFOAM and DETCHEM. *Catalysis Today* **258, Part 2,** 230–240 (2015).

28. Deutschmann, O. Modeling of the Interactions Between Catalytic Surfaces and Gas-Phase. *Catalysis Letters* **145,** 272–289 (2015).

29. Wehinger, G., Kraume, M., Berg, V., Korup, O., Mette, K., Schlögl, R., Behrens, M. & Horn, R. Investigating dry reforming of methane with spatial reactor profiles and particle-resolved CFD simulations. *AIChE Journal* **62,** 4436–4452 (2016).

30. Schneider, A., Mantzaras, J., Bombach, R., Schenker, S., Tylli, N. & Jansohn, P. Laser induced fluorescence of formaldehyde and Raman measurements of major species during partial catalytic oxidation of methane with large H_2O and CO_2 dilution at pressures up to 10 bar. *Proceedings of the Combustion Institute* **31,** 1973–1981 (2007).

31. Zellner, A., Suntz, R. & Deutschmann, O. Two-Dimensional Spatial Resolution of Concentration Profiles in Catalytic Reactors by Planar Laser-Induced Fluorescence: NO Reduction over Diesel Oxidation Catalysts. *Angewandte Chemie International Edition* **54,** 2653–2655 (2015).

32. Stavitski, E., Kox, M., Swart, I., deGroot, F. & Weckhuysen, B. In Situ Synchrotron-Based IR Microspectroscopy To Study Catalytic Reactions in Zeolite Crystals. *Angewandte Chemie International Edition* **47,** 3543–3547 (2008).

33. Titze, T., Chmelik, C., Kullmann, J., Prager, L., Miersemann, E., Gläser, R., Enke, D., Weitkamp, J. & Kärger, J. Microimaging of Transient Concentration Profiles of Reactant and Product Molecules during Catalytic Conversion in Nanoporous Materials. *Angewandte Chemie International Edition* **54,** 5060–5064 (2015).

34. Hüppmeier, J., Barg, S., Baune, M., Koch, D., Grathwohl, G. & Thöming, J. Oxygen feed membranes in autothermal steam-reformers - A robust temperature control. *Fuel* **89,** 1257–1264 (2010).

35. Löfberg, A., Essakhi, A., Paul, S., Swesi, Y., Zanota, M.-L., Meille, V., Pitault, I., Supiot, P., Mutel, B., Courtois, V. L. & Bordes-Richard, E. Use of catalytic oxidation and dehydrogenation of hydrocarbons reactions to highlight improvement of heat transfer in catalytic metallic foams. *Chemical Engineering Journal* **176-177,** 49–56 (2011).

36. Mülheims, P. & Kraushaar-Czarnetzki, B. Temperature Profiles and Process Performances of Sponge Packings As Compared to Spherical Catalysts in the Oxidation of o-Xylene to Phthalic Anhydride. *Industrial & Engineering Chemistry Research* **50,** 9925–9935 (2011).

37. Schildhauer, T., Pangarkar, K., van Ommen, J., Nijenhuis, J., Moulijn, J. & Kapteijn, F. Heat transport in structured packings with two-phase co-current downflow. *Chemical Engineering Journal* **185-186,** 250–266 (2012).

38. Gräf, I., Rühl, A.-K. & Kraushaar-Czarnetzki, B. Experimental study of heat transport in catalytic sponge packings by monitoring spatial temperature profiles in a cooled-wall reactor. *Chemical Engineering Journal* **244,** 234–242 (2014).

39. Gräf, I., Ladenburger, G. & Kraushaar-Czarnetzki, B. Heat transport in catalytic sponge packings in the presence of an exothermal reaction: Characterization by 2D modeling of experiments. *Chemical Engineering Journal* **287,** 425–435 (2016).

40. Korup, O., Mavlyankariev, S., Geske, M., Goldsmith, C. F. & Horn, R. Measurement and analysis of spatial reactor profiles in high temperature catalysis research. *Chemical Engineering and Processing: Process Intensification* **50,** 998–1009 (2011).

41. Nogare, D., Degenstein, N., Horn, R., Canu, P. & Schmidt, L. Modeling spatially resolved profiles of methane partial oxidation on a Rh foam catalyst with detailed chemistry. *Journal of Catalysis* **258,** 131–142 (2008).

42. Nguyen, H., Harold, M. & Luss, D. Optical frequency domain reflectometry measurements of spatio-temporal temperature inside catalytic reactors: Applied to study wrong-way behavior. *Chemical Engineering Journal* **234,** 312–317 (2013).

43. Nguyen, H., Harold, M. & Luss, D. Spatiotemporal behavior of Pt/Rh/CeO2/BaO catalyst during lean-rich cycling. *Chemical Engineering Journal* **262,** 464–477 (2015).

44. Bosco, M. & Vogel, F. Optically accessible channel reactor for the kinetic investigation of hydrocarbon reforming reactions. *Catalysis Today* **116,** 348–353 (2006).

45. Gänzler, A., Casapu, M., Boubnov, A., Müller, O., Conrad, S., Lichtenberg, H., Frahm, R. & Grunwaldt, J.-D. Operando spatially and time-resolved X-ray absorption spectroscopy and infrared thermography during oscillatory CO oxidation. *Journal of Catalysis* **328,** 216–224 (2015).

46. Kopyscinski, J., Schildhauer, T., Vogel, F., Biollaz, S. & Wokaun, A. Applying spatially resolved concentration and temperature measurements in a catalytic plate reactor for the kinetic study of CO methanation. *Journal of Catalysis* **271,** 262–279 (2010).

47. Frey, M., Romero, T., Roger, A.-C. & Edouard, D. Open cell foam catalysts for CO_2 methanation: Presentation of coating procedures and in situ exothermicity reaction study by infrared thermography. *Catalysis Today* **273,** 83–90 (2016).

48. Gord, J., Meyer, T. & Roy, S. Applications of ultrafast lasers for optical measurements in combusting flows. *Annu. Rev. Anal. Chem.* **1,** 663–687 (2008).

49. Frank, J. & Kaiser, S. High-resolution imaging of dissipative structures in a turbulent jet flame with laser Rayleigh scattering. *Experiments in Fluids* **44,** 221–233 (2008).

50. Rothamer, D., Snyder, J., Hanson, R. & Steeper, R. Optimization of a tracer-based PLIF diagnostic for simultaneous imaging of EGR and temperature in IC engines. *Applied Physics B* **99,** 371–384 (2010).

51. Koptyug, I. in *Spectroscopic Properties of Inorganic and Organometallic Compounds: Volume 45* (eds Yarwood, J., Douthwaite, R. & Duckett, S.) 1–42 (The Royal Society of Chemistry, 2014).

52. Koptyug, I., Lysova, A., Sagdeev, R. & Parmon, V. Application of multinuclear MRI and solid state MRI in heterogeneous catalysis. *Catalysis Today* **126,** 37–43 (2007).

53. Gladden, L., Abegao, F., Dunckley, C., Holland, D., Sankey, M. & Sederman, A. MRI: Operando measurements of temperature, hydrodynamics and local reaction rate in a heterogeneous catalytic reactor. *Catalysis Today* **155,** 157–163 (2010).

54. Lysova, A. & Koptyug, I. Magnetic resonance imaging methods for in situ studies in heterogeneous catalysis. *Chemical Society Reviews* **39,** 4585–4601 (2010).

55. Roberts, S., Renshaw, M., Lutecki, M., McGregor, J., Sederman, A., Mantle, M. & Gladden, L. Operando magnetic resonance: monitoring the evolution of conversion and product distribution during the heterogeneous catalytic ethene oligomerisation reaction. *Chemical Communications* **49,** 10519–10521 (2013).

56. Yuen, E., Sederman, A. & Gladden, L. In situ magnetic resonance visualisation of the spatial variation of catalytic conversion within a fixed-bed reactor. *Applied Catalysis A: General* **232,** 29–38 (2002).

57. Gladden, L., Alexander, P., Britton, M., Mantle, M., Sederman, A. & Yuen, E. In situ magnetic resonance measurement of conversion, hydrodynamics and mass transfer during single- and two-phase flow in fixed-bed reactors. *Magnetic Resonance Imaging* **21,** 213–219 (2003).

58. Koptyug, I., Lysova, A., Kulikov, A., Kirillov, V., Parmon, V. & Sagdeev, R. Functional imaging and NMR spectroscopy of an operating gas-liquid-solid catalytic reactor. *Applied Catalysis A: General* **267,** 143–148 (2004).

59. Lysova, A., Koptyug, I., Kulikov, A., Kirillov, V., Sagdeev, R. & Parmon, V. Nuclear magnetic resonance imaging of an operating gas-liquid-solid catalytic fixed bed reactor. *Chemical Engineering Journal* **130,** 101–109 (2007).

60. Lysova, A., Koptyug, I., Kulikov, A., Kirillov, V. & Sagdeev, R. An NMR Imaging Study of Steady-State and Periodic Operation Modes of a Trickle Bed Reactor. *Topics in Catalysis* **52,** 1371–1380 (2009).

61. Kirillov, V., Koptyug, I., Kulikov, A., Kuzin, N., Lysova, A., Shigarov, A. & Parmon, V. Self-oscillations on a partially wetted catalyst pellet in α-methylstyrene hydrogenation: Experiment and mathematical modeling. *Theoretical Foundations of Chemical Engineering* **39,** 24–35 (2005).

62. Sederman, A., Mantle, M., Dunckley, C., Huang, Z. & Gladden, L. In Situ MRI Study of 1-octene Isomerisation and Hydrogenation within a Trickle-bed Reactor. *Catalysis Letters* **103,** 1–8 (2005).

63. Gladden, L., Mantle, M. & Sederman, A. Magnetic resonance imaging of catalysts and catalytic processes. *Advances in Catalysis* **50,** 1–75 (2006).

64. Glover, P. & Mansfield, P. Limits to magnetic resonance microscopy. *Reports on Progress in Physics* **65,** 1489 (2002).

65. Zhivonitko, V., Telkki, V.-V., Leppaniemi, J., Scotti, G., Franssila, S. & Koptyug, I. Remote detection NMR imaging of gas phase hydrogenation in microfluidic chips. *Lab on a Chip* **13,** 1554–1561 (2013).

66. Hoult, D. & Richards, R. The signal-to-noise ratio of the nuclear magnetic resonance experiment. *Journal of Magnetic Resonance (1969)* **24,** 71–85 (1976).

67. Olson, D., Peck, T., Webb, A., Magin, R. & Sweedler, J. High-resolution microcoil 1H-NMR for mass-limited, nanoliter-volume samples. *Science* **270,** 1967 (1995).

68. Telkki, V.-V., Zhivonitko, V., Selent, A., Scotti, G., Leppäniemi, J., Franssila, S. & Koptyug, I. Lab-on-a-Chip Reactor Imaging with Unprecedented Chemical Resolution by Hadamard-Encoded Remote Detection NMR. *Angewandte Chemie* **126,** 11471–11475 (2014).

69. Barskiy, D. *et al.* NMR Hyperpolarization Techniques of Gases. *Chemistry - A European Journal* **23,** 725–751 (2017).

70. Koptyug, I., Kovtunov, K., Burt, S., Anwar, M. S., Hilty, C., Han, S.-I., Pines, A. & Sagdeev, R. para-Hydrogen-Induced Polarization in Heterogeneous Hydrogenation Reactions. *Journal of the American Chemical Society* **129,** 5580–5586 (2007).

71. Kovtunov, K., Salnikov, O., Zhivonitko, V., Skovpin, I., Bukhtiyarov, V. & Koptyug, I. Catalysis and Nuclear Magnetic Resonance Signal Enhancement with Parahydrogen. *Topics in Catalysis* **59,** 1686–1699 (2016).

72. Bouchard, L., Burt, S., Anwar, M., Kovtunov, K., Koptyug, I. & Pines, A. NMR Imaging of Catalytic Hydrogenation in Microreactors with the Use of para-Hydrogen. *Science* **319,** 442–445 (2008).

73. Zhivonitko, V., Telkki, V.-V. & Koptyug, I. Characterization of Microfluidic Gas Reactors Using Remote-Detection MRI and Parahydrogen-Induced Polarization. *Angewandte Chemie International Edition* **51,** 8054–8058 (2012).

74. Germain, D., Chevallier, P., Laurent, A. & Saint-Jalmes, H. MR monitoring of tumour thermal therapy. *Magnetic Resonance Materials in Physics, Biology and Medicine* **13,** 47–59 (2001).

75. Van Geet, A. Calibration of the Methanol and Glycol Nuclear Magnetic Resonance Thermometers with a Static Thermistor Probe. *Analytical Chemistry* **40,** 2227–2229 (1968).

76. Kaplan, M., Bovey, F. & Cheng, H. Simplified method of calibrating thermometric nuclear magnetic resonance standards. *Analytical Chemistry* **47,** 1703–1705 (1975).

77. Koptyug, I., Sagdeev, D., Gerkema, E., As, H. V. & Sagdeev, R. Solid-state ^{27}Al MRI and NMR thermometry for catalytic applications with conventional (liquids) MRI instrumentation and techniques. *Journal of Magnetic Resonance* **175,** 21–29 (2005).

78. Koptyug, I., Khomichev, A., Lysova, A. & Sagdeev, R. Spatially Resolved NMR Thermometry of an Operating Fixed-Bed Catalytic Reactor. *Journal of the American Chemical Society* **130,** 10452–10453 (2008).

79. Lysova, A., Kulikov, A., Parmon, V., Sagdeev, R. & Koptyug, I. Quantitative temperature mapping within an operating catalyst by spatially resolved ^{27}Al NMR. *Chemical Communications* **48,** 5763–5765 (2012).

80. Jarenwattananon, N., Glöggler, S., Otto, T., Melkonian, A., Morris, W., Burt, S., Yaghi, O. & Bouchard, L. Thermal maps of gases in heterogeneous reactions. *Nature* **502,** 537–540 (2013).

81. Jarenwattananon, N. & Bouchard, L. Motional Averaging of Nuclear Resonance in a Field Gradient. *Physical Review Letters* **114,** 197601 (2015).

82. Lisy, V. & Tóthová, J. Comment on "Motional Averaging of Nuclear Resonance in a Field Gradient". *Physical Review Letters* **117,** 249701 (2016).

83. Jarenwattananon, N. & Bouchard, L. Jarenwattananon and Bouchard Reply. *Physical Review Letters* **117,** 249702 (2016).

84. Lisy V., V. & Tóthová, J. Attenuation of the NMR signal due to hydrodynamic Brownian motion. *Journal of Molecular Liquids* **234,** 182–186 (2017).

85. Samouda, F., Colin, S., Barrot, C., Baldas, L. & Brandner, J. J. Micro molecular tagging velocimetry for analysis of gas flows in mini and micro systems. *Microsystem Technologies* **21,** 527–537 (2015).

86. Butscher, D., Hutter, C., Kuhn, S. & von Rohr, P. Particle image velocimetry in a foam-like porous structure using refractive index matching: a method to characterize the hydrodynamic performance of porous structures. *Experiments in Fluids* **53,** 1123–1132 (2012).

87. Rasouli, M., Bertrand, F. & Chaouki, J. A multiple radioactive particle tracking technique to investigate particulate flows. *AIChE Journal* **61,** 384–394 (2015).

88. Koptyug, I., Altobelli, S., Fukushima, E., Matveev, A. & Sagdeev, R. Thermally Polarized ^{1}H NMR Microimaging Studies of Liquid and Gas Flow in Monolithic Catalysts. *Journal of Magnetic Resonance* **147,** 36–42 (2000).

89. Koptyug, I., Ilyina, L. Y., Matveev, A., Sagdeev, R., Parmon, V. & Altobelli, S. Liquid and gas flow and related phenomena in monolithic catalysts studied by ^{1}H NMR microimaging. *Catalysis Today* **69,** 385–392 (2001).

90. Gladden, L. & Sederman, A. Recent advances in Flow MRI. *Journal of Magnetic Resonance* **229,** 2–11 (2013).

91. Ramskill, N., York, A., Sederman, A. & Gladden, L. Magnetic resonance velocity imaging of gas flow in a diesel particulate filter. *Chemical Engineering Science* **158,** 490–499 (2017).

4. Basics of 3D magnetic resonance spectroscopic imaging

Locally resolved magnetic resonance spectroscopic imaging is a well established method for medical diagnostics. But despite its widespread distribution the application for the investigation of chemical reaction processes is comparably rare, and thus the basic principles of 3D MRSI may not be necessarily known in the chemical engineering community. Therefore, the following sections will give a brief introduction into the physical principles of NMR and the applied 3D MRSI methods of this thesis. For a more detailed and extensive description, the interested reader is referred to numerous NMR spectroscopy and Imaging textbooks (for instance: [1]).

4.1. Basics of nuclear magnetic resonance

Nuclear magnetic resonance is based on the effect that atomic nuclei with an odd total number of protons and neutrons posses an angular momentum $\vec{l}$ and a magnetic momentum $\vec{\mu}$ which are directly connected by:

$$\vec{\mu} = \gamma \cdot \vec{l}, \tag{4.1}$$

where γ describes the gyromagnetic ratio which is the ratio of the magnetic moment to the angular momentum of a system. According to the laws of quantum mechanics, the component of the angular momentum $\vec{l}_z$ along a magnetic field $\vec{B}_0$ ($\vec{B}_0 \neq 0$ and $\vec{B}_0 \parallel z$, $z \equiv$ spatial direction) can only exhibit discrete volumes, determined by the spin quantum number I. This corresponds to a quantization of the angular momentum $\vec{l}_z = m \cdot \hbar$, where $\hbar$ is the Planck's constant divided by 2π, and m is given by $m = -I, -I+1, ... + I$. Since the energy of an angular momentum within a magnetic field can be described by $E = -\mu \cdot B_0$, this results in the existence of discrete energy levels:

$$E_m = -\gamma \cdot m \cdot \hbar \cdot B_0 \tag{4.2}$$

If, like in this work, only ^{1}H nuclei with $I = 1/2$ are considered, only two energy levels exist with the energy difference:

$$\Delta E_m = \gamma \cdot \hbar \cdot B_0. \tag{4.3}$$

Exchange between these energy levels can only be achieved by photons of a specific resonance frequency ν_0. The resonance frequency is directly linked to the main magnetic field strength. This relationship is described by the Larmor equation, the fundamental equation of NMR:

$$\omega_0 = 2\pi \cdot \nu_0 = \gamma \cdot B_0. \tag{4.4}$$

For ^{1}H nuclei the gyromagnetic ratio is $\gamma = 42.576 \cdot 2\pi\,\mathrm{MHz/T}$.

The of spin states in thermal equilibrium are populated according to the Boltzmann distribution, i.e. :

$$\frac{N(E_1)}{N(E_2)} = \exp\left(-\Delta E/kT\right), \tag{4.5}$$

where N describes the population of a state, k is the Boltzmann constant and T the absolute temperature. The magnetic properties of all nuclei within a sample volume averaged together create a net magnetization $\vec{M} = (M_x, M_y, M_z)$ in direction of the magnetic field B_0 which can be described like a regular vector using the principles of classical physics. For a tomograph with a magnetic field strength of 7 T this leads at room temperature to a $N(E_1)/N(E_2)$-ratio of 0.99995 which explains the comparably low sensitivity of NMR measurements compared to other methods.

The temporal evolution of $\vec{M}$ is described by the empiric Bloch equations:

$$d\vec{M}(t)/dt = \gamma \cdot \left[\vec{M} \times \vec{B}\right] - \frac{\vec{M}_x + \vec{M}_y}{T_2} - \frac{\vec{M}_z - \vec{M}_0}{T_1}, \tag{4.6}$$

where T_1 is the longitudinal relaxation or spin-lattice time, and T_2 is the transverse or spin-spin relaxation time. At thermal equilibrium in a static magnetic field, the net magnetization is $\vec{M}_0 = (0, 0, M_0)$. The absence of a transverse component of the macroscopic magnetization $\vec{M}_{x,y} = (M_x, M_y, 0)$ represents missing phase coherence of the x and y components of the single spins. To flip

the macroscopic magnetization, a radiofrequency field $\left(\vec{B_1}\right)$, also called Radio Frequency (RF) pulse, with the frequency ν_0, is applied perpendicular to the main magnetic field. This allows a deflection of the net magnetization by a specific "flip angle". After an RF excitation, $\vec{M}$ precesses around the main magnetic field $\vec{B}_0$, and according to the law of induction, induces an RF-voltage into a receiver coil until $\vec{M}_{x,y}$ is decayed due to transversal relaxation.

But due to magnetic field inhomogeneities, which occur in any real NMR experiment the transverse magnetization decays faster than predicted by natural atomic and molecular mechanisms. The time constant for this effective transverse magnetization decay is called T_2^* and takes account of T_2 and the influence of B_0 inhomogeneities, which are described by an additional decay constant T_2':

$$\frac{1}{T_2^*} = \frac{1}{T_2} + \frac{1}{T_2'}. \tag{4.7}$$

The induced voltage detected by the RF-receiver coil is amplified, transformed to the low frequency (LF) range and phase sensitively detected into two channels with a 90° phase difference of the reference signal with the frequency ν_{0r}. This complex LF-signal $s(t)$ is sampled with a constant sampling increment t_s by an analog-to-digital converter and saved ($s_n = s(n \cdot t_s)$ with n = 0,1,2,...N-1). The complex time domain signal can be converted into equally spaced samples of the frequency domain by means of the discrete Fourier transform (DFT), with $k = 1, 0, ...N-1$:

$$f_k = \sum_{n=0}^{N-1} s_N \cdot \exp\left(-i \cdot 2 \cdot \pi \cdot n \cdot k/N\right). \tag{4.8}$$

The sampling rate of the time domain signal determines the spectral width (SW) within which a clear allocation of the sampled signals is possible (Nyquist theorem):

$$SW = 1/t_s. \tag{4.9}$$

Chemical shift

The resonance frequencies of ^{1}H nuclei within a sample are not only effected by the applied external magnetic field, but also by a local field. The local field is a result of shielding effects by electrons surrounding the nuclei. The electrons produce a small induced magnetic field that opposes the external field. Accordingly, the ^{1}H nuclei of different molecules or functional groups of molecules do not resonate at precisely the same frequency. These differences in resonance frequency are called chemical shifts and depend upon the chemical nature of the molecule in which they reside:

$$\omega = (1 - \sigma)\,\omega_0. \tag{4.10}$$

Here σ is the shielding constant.

The chemical shift is given as a field independent dimensionless value $\delta = (\omega - \omega_0)/\omega_0$ in ppm (parts per million) and is specific for each type of nucleus and chemical configuration. Thus it is of fundamental importance, since the measurement of chemical shift distributions allows the determination and quantification of different components within a sample volume. In some special cases it also enables the measurement of temperature [2, 3].

J-coupling

When the spin of one nucleus affects the spin of another nucleus through the intermediary of bonding electrons, so called J-coupling occurs [4]. This is only the case if the nuclei of a molecule are in relatively close proximity to one another, and the nuclei are chemically distinguishable. The result is a spectral line splitting. However, these phenomena do not occur in the reaction system investigated in this work. Thus, it is referred to appropriate literature ([5] for instance), if a more detailed explanation is required.

4.2. NMR tomography

Localization or spatial encoding can be achieved by superimposing the static magnetic field B_0 with a gradient field $\vec{G}$:

$$\omega = \gamma \cdot \left(B_0 + \vec{G} \cdot \vec{r}\right) \tag{4.11}$$

with

$$\vec{G} = (G_x, G_y, G_z) = (\partial B_{0z}/\partial x, \partial B_{0z}/\partial y, \partial B_{0z}/\partial z)\,. \tag{4.12}$$

The superposition leads to a linear change in the magnetic field in x, y or z direction, whereby the resonance frequencies become spatially dependent. The B_0 gradients are applied during signal detection, between RF excitation and signal detection, or during frequency selective RF pulses which results in the three principles of spatial encoding:

1. Spatially selective RF pulses

   The B_0 gradient is applied simultaneously with the RF pulse. Thus, only nuclei within a specific resonance frequency range ΔF_{RF} range are excited which leads to a selection of a specific slice perpendicular to the B_0 gradient (slice selection gradient). The slice thickness can be described by:

$$\Delta z = \frac{2 \cdot \pi \cdot \Delta F_{RF}}{\gamma \cdot G_s}. \tag{4.13}$$

2. Phase encoding

   The B_0 gradient is applied between signal excitation and signal acquisition for the duration τ_{pe}. Accordingly, the signal phase is influenced depending on the spatial position of the spins and the direction of the phase encoding gradient. To achieve spatial encoding multiple phase encoding steps must be used according to $G_{pe} = n_{pe} \cdot \Delta G_{pe}$ with $n_{pe} = -N_{pe}/2+1, ..., N_{pe}/2$ or $n_{pe} = -N_{pe}/2 +1/2, ..., -1/2, 1/2, ..., N_{pe}/2-1/2$. This leads to:

$$FOV_{pe} = \frac{2 \cdot \pi}{\gamma \cdot \Delta G_{pe} \cdot \tau_{pe}}, \tag{4.14}$$

   as well as a nominal resolution of FOV_{pe}/N_{pe}.

3. Frequency encoding

   The B_0 gradient is applied during signal acquisition (read out gradient). All spins within a specific resonance frequency range originate exclusively from a certain slice perpendicular to the direction of the gradient. According to the sampling theorem and in analogy with Eq. 4.14 for the field of view follows:

$$FOV_r = \frac{2 \cdot \pi}{\gamma \cdot \Delta G_r \cdot t_s} \tag{4.15}$$

k-space

The measured total signal is the result of integration over the signal contributions of all individual volume elements of a sample. After generation of transverse magnetization, the signal phase is systematically modulated by frequency or phase encoding B_0-gradients. Disregarding relaxation processes and chemical shift effects it results in:

$$s(t) = C \cdot \int M_{xy}(\vec{r}, t=0) \cdot \exp\left(i \int_0^t \gamma \vec{G}(\tau)\, d\tau \cdot \vec{r}\right) d\vec{r}. \tag{4.16}$$

By introducing the k-vector as an abbreviation:

$$\vec{k} = \vec{k}(t) = \int_0^t \gamma \cdot \vec{G}(\tau)\, d\tau, \tag{4.17}$$

the k-vector dependent NMR signal can be written as

$$s(\vec{k}) = C \cdot \int M_{xy}(\vec{r}, t=0) \cdot \exp\left(i\vec{k} \cdot \vec{r}\right) d\vec{r}. \tag{4.18}$$

The inverse Fourier transform of $s(\vec{k})$ leads to the desired signal distribution $M_{xy}(\vec{r}, t=0)$

$$M_{xy}(\vec{r}, t=0) = C' \cdot \int s\left(\vec{k}\right) \cdot \exp\left(-i\vec{k} \cdot \vec{r}\right) d\vec{k}. \tag{4.19}$$

Consequently, the spatial distribution of the transverse magnetization is given by:

$$M_{xy}(\vec{r}, t=0) = C' \cdot \int s(k_x, k_y, k_z) \cdot \exp\left[-i\left(k_x x + k_y y + k_z z\right)\right] dk_x dk_y dk_z. \tag{4.20}$$

Within the k-space concept, the effect of B_0 gradients for phase or frequency encoding corresponds to a movement in k-space. Thus, sampling the measured data can be described as sampling the entries of the k-space.

4.3. Magnetic resonance spectroscopic imaging (MRSI)

To achieve localized MRSI, the concept has to be extended to a further dimension to enable the encoding of the resonance frequencies ω. Every resonance signal exhibits an offset frequency with respect to a reference frequency depending on its chemical shift. In analogy to a B_0 gradient, this leads to a phase modulation of the signal. Thus, Eq. 4.18 has to be modified to

$$s(k_x, k_y, k_z, k_\omega) = C \cdot \int\int M_{xy}(\vec{r}, t=0) \cdot \exp\left(i\left(k_x x + k_y y + k_z z + k_\omega \omega\right)\right) d\vec{r} d\omega. \tag{4.21}$$

Here, due to the chemical shift, the time dependent signal development after RF pulse excitation corresponds to k_ω. The MRSI methods used

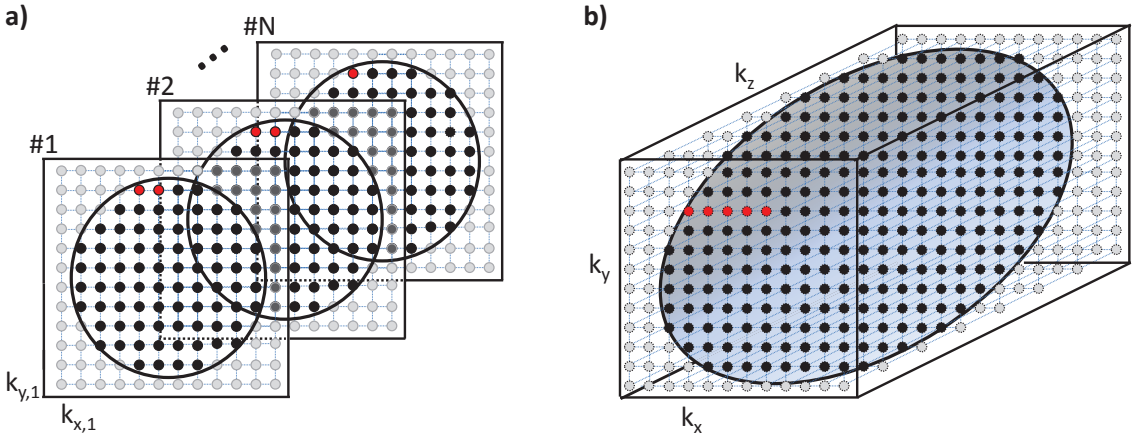

Figure 4.1.: Representation of the k-space of a two dimensional (a) and a three dimensional experiment (b). The black dots are representing k-space entries collected in a circularly reduced k-space sampling scheme of the multi slice MRSI method (a) as applied in chapter 6, and in a (b) ellipsoidal reduced sampling scheme of the 3D MRSI method applied in chapter 7 and chapter 8. The red dots exemplify the order of k-space filling of the different MRSI approaches.

to measure reaction conditions within catalytic beds follow mainly the "standard SI" method originally described by Brown et al. [6] and Maudsley et al. [7]. Since these methods do not use frequency encoding, phase encoding gradients have to be applied in all measured orthogonal spatial directions which makes them more time-consuming compared to other imaging methods. Consequently, the signal is detected as a free induction decay (FID) in the absence of an additional B_0 gradient (cf. Figure 5.1). The individual measurements are repeated with altered phase encoding gradients after the temporal distance of T_R, whereby ΔG is chosen according to the FOV so that the Nyquist theorem is satisfied (cf. Eq. 4.9).

If the required SNR is too low after sampling all k-space data once, averaging of accumulations N_A allows to increase the SNR by a factor of $\sqrt{N_A}$. Accordingly the total measurement time is

$$T_{meas} = N_A \cdot N_x \cdot N_y \cdot T_R \tag{4.22}$$

resp.

$$T_{meas} = N_A \cdot N_x \cdot N_y \cdot N_z \cdot T_R, \tag{4.23}$$

with N_i depending on the matrix size of the k-space (2 or 3 dimensional spatial resolution).

References

1. Elster, A. D. *Questions and answers in magnetic resonance imaging. St. Louis: Mosby-Year Book* 1994.
2. Van Geet, A. Calibration of the Methanol and Glycol Nuclear Magnetic Resonance Thermometers with a Static Thermistor Probe. *Analytical Chemistry* **40,** 2227–2229 (1968).
3. Kaplan, M., Bovey, F. & Cheng, H. Simplified method of calibrating thermometric nuclear magnetic resonance standards. *Analytical Chemistry* **47,** 1703–1705 (1975).
4. Ramsey, N. & Purcell, E. Interactions between nuclear spins in molecules. *Physical Review* **85,** 143 (1952).
5. Keeler, J. *Understanding NMR spectroscopy* (John Wiley & Sons, 2011).
6. Brown, T., Kincaid, B. & Ugurbil, K. NMR chemical shift imaging in three dimensions. *Proceedings of the National Academy of Sciences* **79,** 3523–3526 (1982).
7. Maudsley, A., Hilal, S., Perman, W. & Simon, H. Spatially resolved high resolution spectroscopy by "four-dimensional" NMR. *Journal of Magnetic Resonance (1969)* **51,** 147–152 (1983).

5. Experimental background

Since the previous chapters gave an overview about the chemical reaction engineering background and state-of-the-art characterization methods for gas phase processes as well as the theoretical background of MRI and MRSI, the following sections describe in detail the applied MRSI approaches (section 5.1), the benchmark reaction (section 5.2), and the experimental setup used in this work (section 5.3).

5.1. Gas phase MRSI

Two MRSI approaches are utilized within this thesis: A multislice method with slice selective excitation and 2D spatial resolution (chapter 6) and a 3D MRSI method with excitation of the total sample volume (chapter 7 and chapter 8).

These MRSI methods were optimized to enable gas phase detection which is particularly challenging, because of three major problems: low sensitivity (∼1000 times lower spin density than liquids), fast diffusion (4 orders of magnitude higher than liquids), and short relaxation times [1]. While a low SNR due to low sensitivity can be compensated to a certain extent by an increase of N_A, short relaxation times require to apply strong and rapidly switchable B_0 gradients for spatial encoding. Thus, optimized pulse sequences with ultrashort echo time (T_E) are required to enable an ultrashort delay between RF excitation and FID detection which is necessary to reduce signal losses due to the short effective transverse relaxation time T_2^*. For this purpose, asymmetric RF excitation pulses were applied.

The asymmetric shape of the RF pulse with a reduced pulse duration to 250 µs exhibits a maximum at 70 µs prior to the end of the pulse, thus reducing signal losses due to T_2^*. Immediately after the excitation pulse short triangular-shaped phase encoding gradients were applied to achieve in-plane encoding (multislice MRSI, Figure 5.1a) or 3D encoding (3D MRSI, Figure 5.1b). This permitted a delay between RF excitation and data acquisition of only 350 µs.

Although a flip angle (α) of 90° would generate the highest detectable net magnetization, the applied excitation pulses were optimized for reduced flip angles (multislice MRSI: 30°; 3D MRSI: 12.5°). Here this is also advantageous, because the time for a complete recovery of the longitudinal magnetization of the sample is reduced, thus shorter repetition times can be applied, and disturbing T_1 effects on the measured FID are reduced. If the repetition time is too low for a complete recovery of longitudinal magnetization, saturation effects occur which decrease the signal intensity and can lead to biased measurements (cf. chapter 6).

The impact of repetition time (T_R) and flip angle on the signal intensity can be described by

$$M_{xy} = M_0 \cdot \frac{1 - \exp\left(-T_R/T_1\right)}{1 - \cos\left(\alpha\right) \cdot \exp\left(-T_R/T_1\right)} \cdot \sin\left(\alpha\right) \cdot \exp\left(T_E/T_2^*\right), \quad (5.1)$$

and allows an estimation of most favorable sequence parameters. To illustrate this relation, the flip angle dependent signal intensity for a given T_R to T_1 ratio is given in Figure 5.2.

To reduce the measurement time, reduced k-space sampling was applied as proposed by Maudsley et al. [2]. Here, less points of the k-space are sampled as would be given by the FOV and the nominal voxel size ΔV. In case of k-spaces with two spatial dimensions, as in the multislice MRSI approach used in chapter 6 only k-space entries are sampled for which $\sqrt{k_x^2 + k_y^2} \leq k_{r,max}$ holds true (cf. Figure 4.1a). This reduces the measurements time by about 21.5 %. In case of a non-cubic k-space with three spatial dimensions, as in chapter 7 and chapter 8, only those k-space entries are measured which are within a respective ellipsoid (cf. Figure 4.1b). Doing so, a reduction of measurement time of almost 50 % is achieved.

In addition to the reduced measurement time, reduced k-space sampling leads to an enhanced point spread function (PSF): Although the PSF exhibits slightly increased full width at half maximum, it is isotropic and features reduced Gibbs ringing effects.

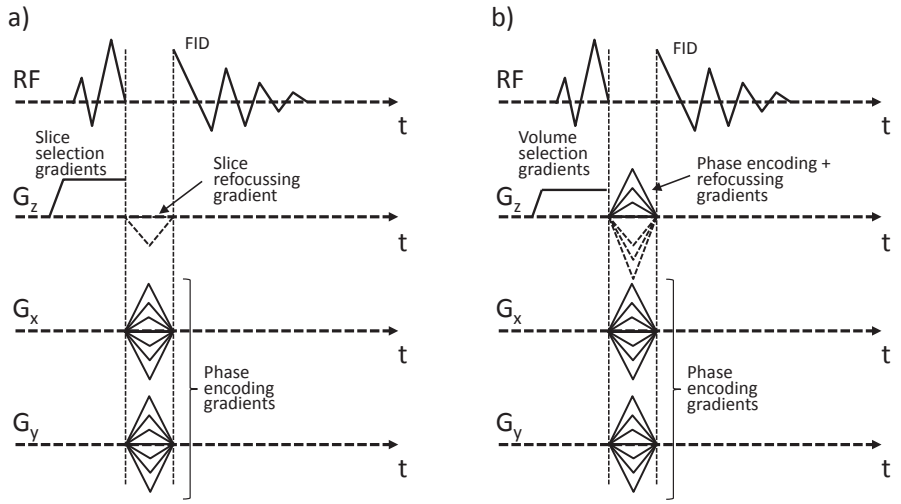

Figure 5.1.: (a)Multislice MRSI (cf. chapter 6) and (b) 3DMRSI (cf. chapter 7 and chapter 8) pulse sequences with asymmetric excitation pulses used to investigate the gas phase processes. In the multislice MRSI sequence, the RF excitation pulse was used for slice selective signal excitation, whereas in the 3D MRSI method the RF pulse excited the entire FOV in z direction.

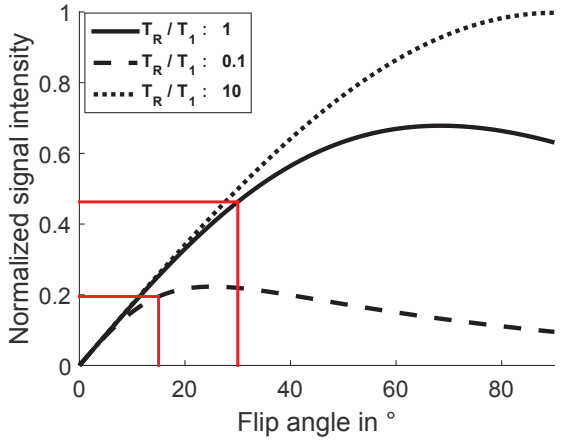

Figure 5.2.: Flip angle dependent signal intensity according to Eq. 5.1: The solid line corresponds to the resulting signal intensity for a T_R/T_1-ratio estimated for the multislice MRSI experiments (cf. chapter 6), the dashed line corresponds to signal intensity development for a T_R/T_1-ratio estimated for the 3D MRSI experiments (cf. chapter 7 and chapter 8). The dotted line shows the signal intensity for the case that the repetition time is ten times larger than the longitudinal relaxation time (full relaxation). In all cases T_E/T_2^* is assumed to be constant. It should be noted, that the actually applied flip angles were selected rather conservatively to avoid saturation effects.

5.2. Pt-catalyzed ethylene hydrogenation: The ideal benchmark reaction

The reaction between an alkene and hydrogen is a hydrogenation reaction. The process is typically exothermic. The simplest conceivable hydrogenation is the hydrogenation of ethylene which yields usually a single product: ethane (cf. Eq. 5.2). Due to the high bonding enthalpy of the H_2-bonding, this reaction is kinetically hindered under standard conditions. In presence of a catalyst which aids the cleavage of the hydrogen molecules, the ethylene hydrogenation can occur even at temperatures of only 173 K [3].

$$C_2H_4 + H_2 \longrightarrow C_2H_6 \quad \Delta H_R = -137 \text{ kJ/mol} \tag{5.2}$$

Sabatier and Senderens were the first to discover that ethylene and hydrogen, in the presence of nickel, lead to the formation of ethane [4]. Later also various other metals like Pt, Rh, Pd, Rg, Ru, Ir, Os, Cu Fe, Co, and Ag were found to catalyze the ethylene hydrogenation [5, 6]. Initially thought to be a very simple process, a deuterium based study in the 1930s gave first insights into the complex surface chemistry of this reaction [7]. In this study, Horiuti and Polanyi proposed the earliest mechanism for the ethylene hydrogenation. They assumed that ethylene adsorbs to the metal surface in the di-σ configuration, and hydrogen addition occurs stepwise to ethyl C_2H_5 and finally to ethane C_2H_6 (cf. Figure 5.3).

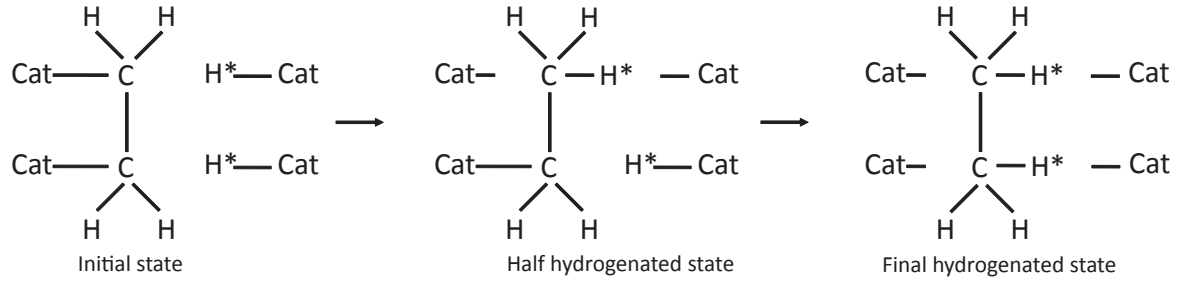

Figure 5.3.: Scheme of the mechanism of the ethylene hydrogenation proposed by Horiuti and Polanyi [7].

Their study marked a milestone in catalysis research as they could prove that an exchange reaction was taking place, and proposed a reaction mechanism, known as Horiut-Polanyi mechanism, which could satisfactorily explain the observed reaction phenomena. Their mechanism is still relevant for various heterogeneously catalyzed hydrogenation reactions [3]. Since this study, the Pt-catalyzed ethylene hydrogenation has been studied as model reaction to achieve deeper insights into the complex surface chemistry of heterogeneously catalyzed hydrogenation reactions [8–17]. The Pt-catalyzed process is of particular interest because the reaction kinetics appear to be independent of the physical form of the catalyst, but are temperature dependent [3, 13, 14].

The current mechanistic approach assumes a competitive adsorption of ethylene and hydrogen on the Pt surface, followed by elementary reactions between the adsorbed transient intermediates which leads the ethane as final product [18]. Here, two different pathways occur (cf. Figure 5.4). A major pathway, where hydrogen chemisorbs associatively. Then gaseous ethylene adsorbs at the Pt surface to become π-C_2H_4 which is subsequently hydrogenated to ethyl and finally associatively desorbs to gaseous ethane. This pathway is quite similar to the mechanism proposed by Horiuti and Polanyi with the only difference being the absorbed ethylene bond type. The second and slower pathway occurs primarily under conditions of excess ethylene. It involves the change in surface binding from π-C_2H_4 to ethylidene which can act as surface inhibitor. At higher temperatures ethylidene dehydrogenates to ethylidyne (CCH_3), which is, despite of its high binding energy, a very mobile surface species [19]. It causes less hindrance to adsorbates than ethylidene, because it can simply be pushed aside.

This change in surface coverage may explain why hydrogen reaction orders apparently increase with increasing temperature [20]. Because all steps

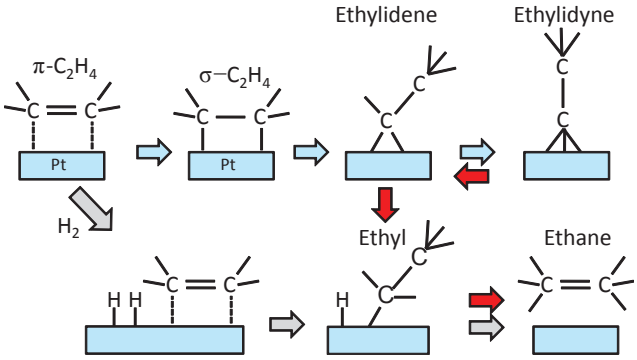

Figure 5.4.: Scheme of the reaction mechanisms involved in the catalytic hydrogenation (and decomposition) of ethylene based on [18] and [17]. The top half of the reaction sequence shows the decomposition of ethylene on a Pt-surface in the absence of H_2. The bottom half indicates the reaction sequence involved in ethylene hydrogenation over the Pt-metal in the presence of excess H_2. The red arrows depict the scenario in which hydrogenation to ethane takes place in the presence of H_2 after ethylene has decomposed into various hydrocarbonaceous species in a H_2-starved reaction.

are highly reversible, ethylidyne can also be hydrogenated again, and rejoin the major pathway to produce ethane. Due to this comparably complicated reaction mechanism it should be noted that there is no single rate-determining step valid for all possible temperature and concentration conditions, which is also the reason why apparently well suited Langmuir-Hinshelwood Hougen-Watson kinetic approaches (cf. Fig 5.3) are almost never applied in kinetic studies.

To predict reaction rates (r) for the ethylene hydrogenation reaction, the vast majority of studies apply power-law approaches of the form $r = k \cdot p_{H_2}^m p_{C_2H_4}^n$ with positive orders in hydrogen (m) in the range of unity and slightly negative orders in ethylene (n), which can also be zero. Here, p corresponds to the partial pressure and k is the rate constant. Even though the order in hydrogen suggests that a molecule or two atoms appear in the rate-determining step, and the order in ethylene

might represent competitive adsorption, these rate laws are just an approximation of a more meaningful expression, and thus are only valid for a limited pressure and temperature range [3]. These approaches, for instance, can not account for the apparent decrease of order in hydrogen observed for temperatures below 290 K. If predictions of reaction rates over a wide range of conditions are necessary, thermodynamically consistent microkinetic models have to be applied which consider the underlying mechanistic aspects of the reaction [16]. Such modeling approaches, however, increase computation time and implementation effort into reactor models enormously. Thus, in spite of the previously mentioned disadvantages power law approaches may be sufficient if the reaction conditions can be tightly defined.

In addition to the aforementioned extensive knowledge of the reaction mechanisms and kinetics which aids to develop modeling approaches enormously (see chapter 7 and chapter 8) also other features of the reaction makes it an excellent choice as a benchmark reaction to prove the applicability of MRI to characterize exothermic gas phase reaction processes:

First of all, ethylene and ethane molecules are symmetric, thus both gases give rise to single resonance lines in NMR spectra. Furthermore, the resonance frequencies of ethylene and ethane are far apart with a chemical shift difference of 4.43 ppm [21]. This facilitates signal separation, and consequently NMR based concentration measurements (cf. Fig 5.5). The selectivity towards ethane simplifies NMR data analysis even further since no side products have to be considered.

The hydrogenation is significantly exothermic (Eq. 5.2) like the industrially relevant gas phase processes mentioned in section 2.1. Hence, the process leads to a significant thermal energy input into the catalytic bed of a reactor, which likely leads to non-isothermal temperature profiles comparable to those within conventional tubular reactors.

And finally, ethylene is one of the most important building blocks in chemical industry [22]. If the NMR based characterization of the ethylene hydrogenation is possible, the characterization of other, industrially relevant gas phase processes, which include ethylene conversion, like ethylene oxide production for instance, becomes feasible.

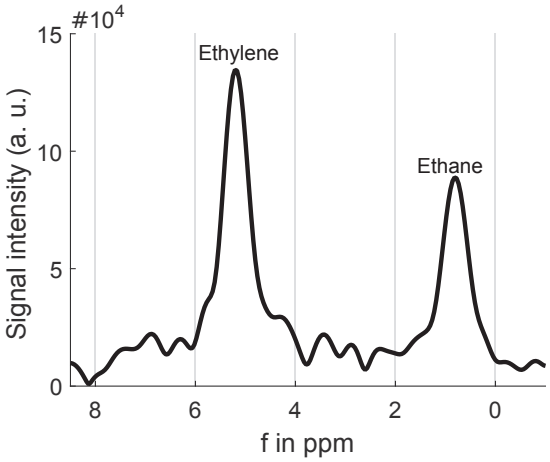

Figure 5.5.: Typical magnitude spectrum of an ethylene ethane mixture measured in an operating catalyst bed. The resonance frequencies exhibit a chemical shift difference of about 4.43 ppm [21] which facilitates signal separation, and thus allow NMR based concentration measurements.

5.3. Description of the setup used for the NMR experiments with reactive flows

To perform the experiments with reactant gaseous flows described in chapter 6 to chapter 8 an NMR compatible fixed-bed glass reactor, developed and manufactured in-house (see Figure 5.6), was used with an inner diameter of 30 mm, a typical size at industrial scale. Three mass flow controllers (F-201CV, Bronkhorst, Ruurlo, Niederlande & FMA-2618-A, Omega Engineering, Stamford, USA) enabled to feed the reactant gases (H_2 and C_2H_4) and the the inert gases (N_2 or Ar) to the reactor. The reactants passed the catalytic bed of the NMR reactor that was positioned in the FOV of the NMR tomograph (cf. Fig 5.7). A specially designed mounting system with an integrated guide rail (not shown) allowed the precise and repeatable positioning of the NMR reactor inside the tomograph. Downstream, the product gas flow was monitored by a flow meter (VAF Fluid-Technik GmbH, Lichtenau, Germany) and the pressure was controlled by a regulation valve. Before it proceeded to the exhaust, the composition of the product gas was analyzed with a process mass spectrometer (pMS, GAM 200, InProcess Instruments, Bremen, Germany) every 5 seconds. To monitor reactant gas concentrations, the inlet gas composition was measured by the pMS before each experiment by using a bypass system.

To prevent damage of the NMR system due to overheating, the reactor was cooled with a continuous flow of pressurized air, and insulated with glass fiber mat. Dried air was used as a cooling agent, because it is invisible to the NMR system, and thus can not distort the NMR measurements. The surface temperature of the NMR detection coil was monitored by a fiberoptic thermometer (Luxtron 504, Polytec, Waldheim, Germany). The mass flow controllers were controlled by a Labview interface, which also recorded flow rate data and coil surface temperatures.

The NMR imaging system used in this work is a BioSpec 70/20 USR manufactured by Bruker (Bruker Biospin MRI GmbH, Ettlingen, Germany). A picture of the system is given in Figure 5.6. In general the BioSpec series is designed for small animal imaging applications in life science, biomedical and preclinical research and is widely distributed in biomedical research groups.

The BioSpec 70/20 is equipped with a superconducting magnet system with a field strength of 7 T. The magnet system has a horizontal bore with a diameter of 200 mm. The total length of the NMR tomograph is 1.312 m with a diameter of 1.12 m. The system is equipped with a B-GA 12S2 gradient system with room temperature shim coils and related power supplies.

The gradient system has a slew rate of 3440 T/m/s and maximum gradient strength is 441 mT/m per spatial direction. It enables a switching time of 130 µs. For the experiments a quadrature birdcage RF coil with an inner diameter of 72 mm was used for both RF transmission and signal reception.

References

1. Glover, P. & Mansfield, P. Limits to magnetic resonance microscopy. *Reports on Progress in Physics* **65,** 1489 (2002).
2. Maudsley, A., Matson, G., Hugg, J. & Weiner, M. Reduced phase encoding in spectroscopic imaging. *Magnetic Resonance in Medicine* **31,** 645–651 (1994).
3. Bond, G. *Metal-Catalysed Reactions of Hydrocarbons* (eds Twig, M. V. & Spencer, M. S.) (Springer Science+Business Media, Inc., 2005).
4. Sabatier, P. & Senderens, J. Action du nickel sur l′ethylène. Synthèse de l′ethane. *Comptes rendus de l′Academie des sciences* **124,** 1358–1360 (1897).
5. Sabatier, P. Hydrogénations et deshydrogénations par catalyse. *European Journal of Inorganic Chemistry* **44,** 1984–2001 (1911).
6. Horiuti, J. & Miyahara, K. *Hydrogenation of ethylene on metallic catalysts* (US Department of Commerce, National Bureau of Standards, 1968).
7. Horiuti, I. & Polanyi, M. Exchange reactions of hydrogen on metallic catalysts. *Transactions of the Faraday Society* **30,** 1164–1172 (1934).
8. Kemball, C. 146. The deuteration and exchange of ethylene on evaporated metal catalysts at low temperatures. *Journal of the Chemical Society (Resumed),* 735–743 (1956).
9. Bond, G., Phillipson, J., Wells, P. & Winterbottom, J. Hydrogenation of olefins. Part 1.-Hydrogenation of ethylene, propylene and the n-butenes over alumina-supported platinum and iridium. *Transactions of the Faraday Society* **60,** 1847–1864 (1964).
10. Dorling, T., Eastlake, M. & Moss, R. The structure and activity of supported metal catalysts: IV. Ethylene hydrogenation on platinum/silica catalysts. *Journal of Catalysis* **14,** 23–33 (1969).
11. Kesmodel, L., Dubois, L. & Somorjai, G. LEED analysis of acetylene and ethylene chemisorption on the Pt (111) surface: Evidence for ethylidyne formation. *The Journal of Chemical Physics* **70,** 2180–2188 (1979).
12. Zaera, F. & Somorjai, G. Hydrogenation of Ethylene over Platinum (111) Single-Crystal Surfaces. *Journal of the American Chemical Society* **106,** 2288–2293 (1984).
13. Cortright, R., Goddard, S., Rekoske, J. & Dumesic, J. Kinetic study of ethylene hydrogenation. *Journal of Catalysis* **127,** 342–353 (1991).
14. Cremer, P., Stanners, C., Niemantsverdriet, J., Shen, Y. & Somorjai, G. The conversion of di-σ bonded ethylene to ethylidyne on Pt(111) monitored with sum frequency generation: evidence for an ethylidene (or ethyl)

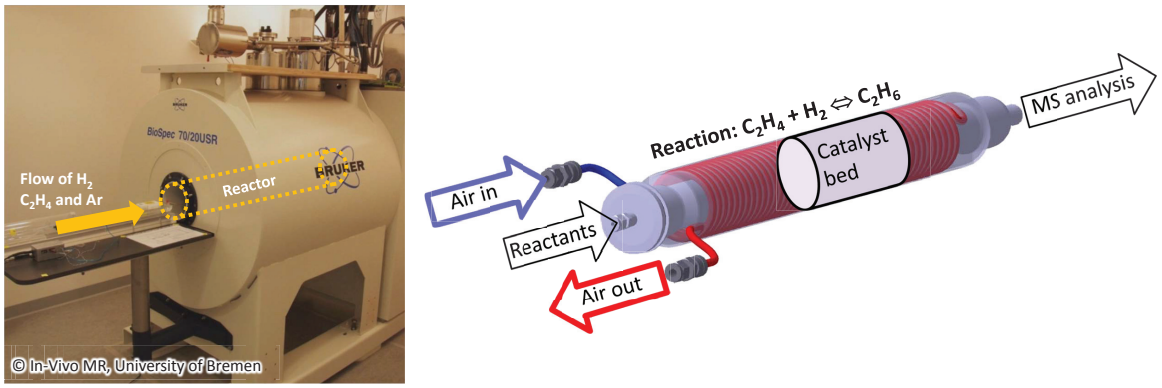

Figure 5.6.: NMR Tomograph Biospec 70/20 USR (Bruker Biospin MRI GmbH, Ettlingen, Germany) and a CAD drawing of the NMR reactor

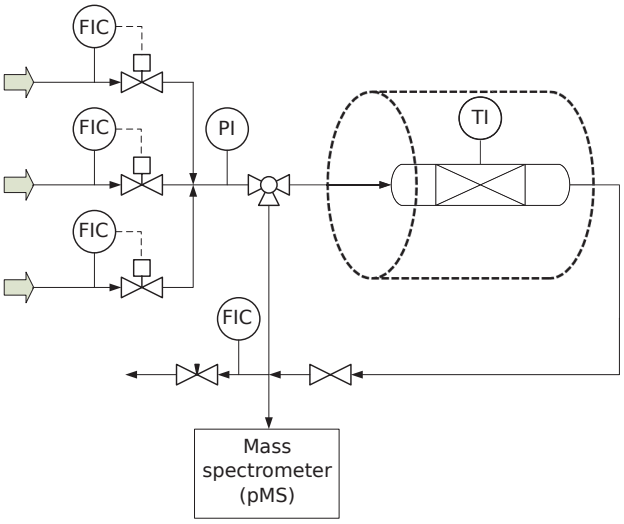

Figure 5.7.: Process flow diagram of the NMR setup used for all NMR experiments with reactive gaseous flows. An illustration of the reactor is shown in Figure 5.6.

intermediate. *Surface Science* **328,** 111–118 (1995).

15. Deng, R., Herceg, E. & Trenary, M. Formation and hydrogenation of ethylidene on the Pt (111) surface. *Surface science* **560,** L195–L201 (2004).

16. Salciccioli, M., Chen, Y. & Vlachos, D. Microkinetic modeling and reduced rate expressions of ethylene hydrogenation and ethane hydrogenolysis on platinum. *Industrial & Engineering Chemistry Research* **50,** 28–40 (2010).

17. Ghosh, A., Hsu, B., Dougal, S., Afeworki, M., Stevens, P. & Yeganeh, M. Effects of Gas Feed Ratios and Sequence on Ethylene Hydrogenation on Powder Pt Catalyst Studied by Sum Frequency Generation and Mass Spectrometry. *ACS Catalysis* **4,** 1964–1971 (2014).

18. Cremer, P., Su, X., Shen, R. & Somorjai, G. Ethylene hydrogenation on Pt (111) monitored in situ at high pressures using sum frequency generation. *Journal of the American Chemical Society* **118,** 2942–2949 (1996).

19. Nomikou, Z., Van Hove, M. & Somorjai, G. Molecular Modeling of Ethylidyne Adsorption and Diffusion on Pt(111). *Langmuir* **12,** 1251–1256 (1996).

20. Rekoske, J., Cortright, R., Goddard, S., Sharma & Dumesic, J. Microkinetic analysis of diverse experimental data for ethylene hydrogenation on platinum. *Journal of physical chemistry* **96,** 1880–1888 (1992).

21. Ebrahimi, H., Shaghaghi, H. & Tafazzoli, M. Gauge invariant atomic orbital-density functional theory prediction of accurate gas phase ^{1}H and ^{13}C NMR chemical shifts. *Concepts in Magnetic Resonance Part A* **38A,** 269–279 (2011).

22. Zimmermann, H. & Walzl, R. Ethylene. *Ullmann's Encyclopedia of Industrial Chemistry* (Wiley-VCH Verlag GmbH & Co. KGaA, 2000).

6. NMR imaging of gas phase reaction processes

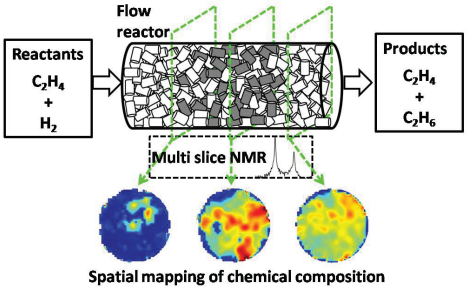

Adapted from:
NMR imaging of gas phase hydrogenation in a packed bed flow reactor
Published in:
Applied Catalysis A, Received 07.04.2015, Revised 11.06.2015, Accepted 12.06.2015
DOI: 10.1016/j.apcata.2015.06.011
Authors:
Jürgen Ulpts[a], Wolfgang Dreher[b,*], Miriam Klink[c] and Jorg Thöming[a]

[a] University of Bremen, Center for Environmental Research and Sustainable Technology (UFT), Leobener Str. 6, 28359 Bremen, Germany
[b] University of Bremen, Department of Chemistry (FB2), in vivo MR Group, 28359 Bremen, Leobener Str. 2, Germany
[c] University of Bremen, Department of Chemistry (FB2), Institute of Applied and Physical Chemistry, Leobener Str. 6, Germany
[*] Corresponding author. Phone: +49 421 218 63090, E-Mail: wdreher@Uni-Bremen.de

Abstract: In situ analysis of heterogeneously catalyzed gas phase reaction systems is becoming a valuable aid to their modeling and optimization. The commonly applied methods are either invasive, do not provide spatial information or are not applicable for optically inaccessible systems. This work investigates the possibility to use NMR imaging to study gas phase reaction processes in situ, spatially resolved and non-invasively.

A multislice NMR spectroscopic imaging pulse sequence, which was optimized to realize ultrashort echo time T_E, was employed to study the ethylene hydrogenation reaction in an NMR-compatible packed bed flow reactor. The catalyst bed, containing inactive γ-Al_2O_3-pellets and Pt-Al_2O_3-pellets, was subdivided into several sections in order to identify reaction zones that depend on initial conditions. Spatial mapping of the chemical composition was demonstrated on the basis of two experiments with varying initial volume flow and ethylene conversion. The inlet and outlet temperature of the catalyst bed was simultaneously detected by analyzing the spectra of inserted glycol capsules.

The resulting spatial shift of the reactive zones in both experiments could be proven by the spatially resolved concentration measurements and the temperature measurements. The locations of single active catalyst pellets were also detectable by the same measure. The quantitative results of product gas composition of both experiments were in good agreement with accompanying mass spectrometric measurements.

The results demonstrate the applicability of NMR imaging methods to investigate gas phase reaction processes and can help to establish these methods as a standard tool to map chemical transformations in gas flow reactors.

6.1. Introduction

Heterogeneously catalyzed gas phase reactions have a substantial relevance for the chemical and energy industry. Prominent examples are the Sabatier reaction, the hydrogenation of alkines, the partial oxidation of alkenes or the oxidative dehydrogenation of alkanes. Due to the high potential of these reactions, performance enhancements of these processes are of high interest as even small improvements can already be economically viable [1].

A well established way to achieve significant enhancements is to optimize mass and heat transport within a catalyst bed, which are known to influence parameters like activity and selectivity drastically [2–5]. To optimize the processes within a reactor, knowledge about the inner conditions of a reactor is needed. However, techniques that provide integral information about chemical composition like online gas chromatography (GC) analysis or invasive measurements like probe thermometers, which provide a rather coarse spatial resolution at selected positions, are still state-of-the-art and are widely used to validate modeling approaches [6–8]. While these methods have clearly proven their value, methods which allow to non-invasively obtain information about temperature and chemical composition combined with high spatial and temporal resolution have gained considerable attention [9–13]. These methods are particularly suitable for the investigation of microscopic processes, such as adsorption reactions and the determination of reaction intermediates. However, the investigated reaction systems have to be optically accessible, which makes these methods not applicable when information about reaction processes within opaque environments, like porous catalyst beds, should be acquired.

Another approach to map chemical compositions and temperature, particularly in optically opaque reactors, is to apply nuclear magnetic resonance (NMR) based methods, i.e. magnetic resonance imaging (MRI), localized NMR spectroscopy (MRS) or magnetic resonance spectroscopic imaging (MRSI) [14, 15]. These NMR based methods are not only well established and widely used diagnostic tools for medical and biomedical applications, but have also found various applications in material sciences and chemical engineering [16]. NMR based methods offer a lot of advantages compared to other methods. They are not only non-invasive, but additionally provide a whole realm of contrast mechanisms such as concentration, relaxation times, flow, diffusion, temperature or magnetization transfer. In particular, they allow to simultaneously measure parameters like chemical composition and temperature with both high spatial and temporal resolution, which is crucial to validate spatially resolved simulations of catalytic reactors.

Nowadays, suitable NMR imaging systems are widely available, although often in research facilities focusing on biomedical research, and not on material sciences or catalysis. Thus, MRI and MRSI might appear to be ideal tools to non-invasively investigate macroscopic transport processes within chemical reactors in situ. However, scientific publications on this topic are still rather rare, which is due to several reasons.

(i) A reactor designed for operation within an MRI magnet has to be made of NMR-compatible materials. The use of metals is limited, even if non-magnetic, as they would distort the static magnetic field B_0 and/or screen the radio frequency (RF) field B1, thus making MRI measurements impossible. Therefore, the design of NMR compatible reactors is challenging, particularly for high temperature and high pressure.

(ii) The interaction between molecules of liquids or gases, which are to be measured, and the porous carrier material with the catalyst shortens the effective transverse relaxation time T_2^*. Thus the transverse magnetization decays rapidly after RF excitation, resulting in a decreased signal-to-noise ratio (SNR). Additionally, short T_2^* values require to apply strong and rapidly switchable B_0 gradients for spatial resolution as well as optimized pulse sequences with ultrashort echo time (T_E), i.e. an ultrashort delay between RF excitation and signal detection.

(iii) NMR is an inherently insensitive method with respect to SNR, e.g., as compared to mass spectrometry. This fact limits the detection of samples with low concentration of NMR active nuclei as well as the achievable spatial resolution. Solutions to this problem comprise the use of hyperpolarization [17, 18] or special detection techniques such as "remote detection" [19, 20].

(iv) Most of the suitable modern NMR imaging systems are available in a biomedical research environment and not in engineering departments. Considering the difficulties mentioned above and the high prices of NMR imaging systems, initial MRI or MRSI experiments for characterizing cat-

alytic reaction will most likely require a multidisciplinary cooperation. However, this may be difficult to establish because of the considerable experimental requirements and the remaining risks of such projects.

Nevertheless, excellent work on investigating 3-phase reaction systems with MRI methods has been published, e.g., on octene hydrogenation and alpha-methylstyrene hydrogenation [21–25]. Furthermore, a method using the temperature dependence of chemical shift difference between the two signals of ethylene glycol, well known from high resolution NMR spectroscopy [26], was adapted for temperature measurements within an NMR compatible reactor [27]. Even gas phase reactions were investigated by using hyperpolarization or remote detection techniques [28–30]. Recently, an investigation of ethylene polymerization at industrial conditions in a specially designed NMR compatible reactor has been reported [31].

Along with the general requirements for investigating reaction processes by NMR based methods, the analysis of gas phase reactions provides further challenges [32, 33]. The signal intensity of gases is much lower than the intensity of liquids because of the lower spin density (factor ∼1000), especially at low pressure and high temperature. The spin-spin relaxation times T_2 of gases are rather short, which decreases the SNR and complicates signal detection. Additionally, the short T_2 and T_2^* relaxation times as well as the much higher diffusion constants of gases as compared to liquids hamper spatial encoding achieved by spatially selective RF pulses, phase encoding B_0 gradients or readout B_0 gradients.

To address these problems, this work investigates the possibilities to apply NMR based methods to heterogeneously catalyzed gas phase processes within reactors of conventional dimensions at ambient reaction conditions. It was the aim of this study to provide a methodology for observing chemical reactions and temperature changes in a rather large reactor over a longer time (typically hours) and with low flow velocity. Therefore, the conventional approach of using a standard volume RF coil for signal detection and exploiting thermal nuclear polarization was preferred, despite the attractive features of hyperpolarization and remote detection. An NMR compatible reactor was developed for use within a standard quadrature RF volume coil of 72 mm inner diameter. For simultaneously observing the chemical reaction and temperature changes within the reactor, an optimized pulse sequence for multislice ultrashort echo time MRSI was developed. As an example, the ethylene hydrogenation reaction was chosen. Measurements were performed for different flow rate and concentration ratios. The MRSI results were compared with mass spectrometric measurements of the products.

6.2. Experimental

6.2.1. Materials

For the preparation of Pt-Al_2O_3 catalyst, commercial cylindrical γ-Al_2O_3-pellets (length: ∼ 8 mm; diameter: 3.2 mm; BET: 220 m^2/g; Alfa Aesar GmbH) were impregnated with a solution of water and Tetraammineplatinum(II)chloride hydrate (Sigma Aldrich).
In a first step, the pore volume of the Al_2O_3-pellets was calculated by adding water step by step to the porous material. The amount of water, which could be completely adsorbed, was 40 % of the pellet mass. To get 1 wt.% homogeneously distributed Platinum on the pellets, Tetraammineplatinum(II)chloride hydrate was dissolved in the amount of water, which corresponds to the pore volume. After adding the platinum solution to the pellets, they were dried at 120 °C and calcined at 400 °C for 3 h. Before the experiments, the catalyst was activated at a gas flow of 2.5 Nl/min (H_2:N_2 1:5) at a temperature of 400 °C for about 2 h.

6.2.2. Temperature measurements

To measure the temperature level during the experiments at the inlet and outlet of the catalyst bed, cylindrical glass capsules (outer diameter 3 mm; length ca. 10 mm) were manufactured, filled with ethylene glycol (99.5 % purity, Fluka) and fused. The chemical shift difference between the -OH and -CH_2 peaks of ethylene glycol is known to correlate well with temperature within a range of 20 °C and 140 °C [26, 34]. The temperature can be expressed as a function of the chemical shift difference $\Delta\delta$ in ppm [26]:

$$T\,(\mathrm{C}^\circ) = 192.85 - 101.64\ \Delta\delta. \qquad (6.1)$$

The ethylene glycol capsules were placed in front of and behind the reactive zone of the catalyst bed surrounded by inert Al_2O_3-pellets (cf. Figure 6.1)

Table 6.1.: Experimental parameters (volume flow, concentration) of experiment A and B. The volumetric concentrations were measured with a pMS behind the outlet of the reactor. The concentration measurements were performed at steady state conditions. The measurement uncertainty of the pMS was for all experiments below 1 %.

	Experiment A	Experiment B
$\dot{v}_{N_2}$ (Inlet)	0.175 l/min	0.4 l/min
$\dot{v}_{C_2H_4}$ (Inlet)	0.25 l/min	0.5 l/min
$\dot{v}_{H_2}$ (Inlet)	0.075 l/min	0.1 l/min
c_{N_2}	41.3 vol.%	44.2 vol.%
$c_{C_2H_4}$	40.0 vol.%	44.1 vol.%
$c_{C_2H_6}$	18.0 vol.%	11.0 vol.%
c_{H_2}	0.7 vol.%	0.7 vol.%

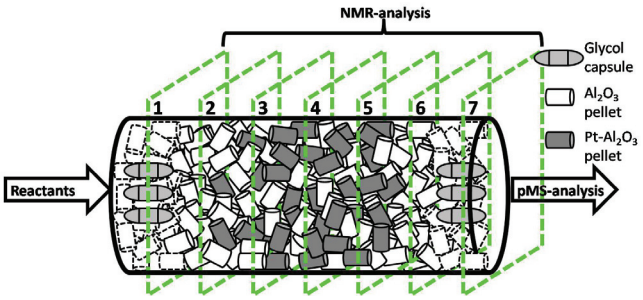

Figure 6.1.: Schematic representation of the structured catalyst bed: The amount of active catalyst pellets was increased from slice 2 to slice 6. The areas around slice 1 and 7 were filled with inert Al_2O_3-pellets containing 3 capsules with ethylene glycol. The slice centers were positioned at -33 mm (#1), -24 mm (#2), -14 mm(#3), -4 mm (#4), 6 mm(#5), 16 mm(#6), 30 mm (#7).

to avoid information loss by crosstalk of the ethylene glycol signal into the gas signal. Before insertion into the catalyst bed, all capsules were tested by MRSI measurements at room temperature. Additionally, one glycol capsule was measured by the MRSI method at four constant temperature values in the range from 19 °C to 44 °C. For these measurements, the glycol capsule was inserted in a beaker filled with perfluoropolyether (Fomblin, Solvay Solexis, Bollate, Italy), in which the temperature was measured by a fiberoptic thermometer (Luxtron 504, Polytec, Waldheim, Germany). The temperature values determined from the chemical shift difference between the two NMR signals of ethylene glycol using Eq. 6.1 were compared with the values measured by the fiberoptic thermometer yielding a largest difference of only 0.6 K.

6.2.3. Ethylene hydrogenation

The investigated gas phase reaction is the hydrogenation of ethylene (see Eq. 6.2). It has been chosen, because it is a well investigated reaction process [35] and offers several favorable characteristics, which makes it a good choice for a model reaction for benchmarking measurements:

$$C_2H_4 + H_2 \longrightarrow C_2H_6 \quad \Delta H_R = -137\,\mathrm{kJ/mol} \tag{6.2}$$

(i) It is nearly irreversible. (ii) It can be run at ambient conditions in presence of a Pt-catalyst. (iii) It is highly exothermal like many of the industrially relevant heterogeneously catalyzed gas phase reactions. (iv) No side products are expected, which facilitates the analysis of reaction products. (v) As ethylene and ethane are symmetric molecules, both gases give rise to single resonance lines. The chemical shift difference between the two signals is larger than 4 ppm [36], which facilitates signal separation.

The reaction was run within a glass tube reactor specially designed for MRI purposes. The reactor had an inner diameter of 30 mm and the catalyst bed a length of 80 mm. The catalyst bed was structured as follows: first a 20 mm thick layer of Al_2O_3-pellets was piled up containing 3 capsules filled with ethylene glycol (cf. Figure 6.1). Then a ca. 40 mm thick layer consisting of a mixture of catalytically active Pt-Al_2O_3-pellets and inert Al_2O_3-pellets were placed inside the reactor. In this layer the amount of catalytically active pellets gradually increased, beginning with very few Pt-Al_2O_3-pellets (just 2-3 in slice #2) up to 50 % of the total volume in slice #5. The last layer (thickness ca. 20 mm, including slice #6 and #7) consisted of inert Al_2O_3-pellets. In slice #7, three ethylene-glycol-capsules were placed for temperature measurements.

The supply of the reactor with nitrogen, hydrogen and ethylene was realized by mass flow controllers (F-201CV, Bronkhorst, Ruurlo, Niederlande & FMA-2618-A, Omega Engineering, Stamford, USA). The total initial volume flow varied between 0.5 l/min and 1.0 l/min with varying hydrogen content of the reactant gases (see Table 6.1). The outlet pressure was held at a constant level of 1.3 bar (abs). Behind the reactor outlet, the composition of the product gases was analyzed by a process mass spectrometer (pMS, GAM 200, In-Process Instruments, Bremen, Germany).

To ensure process safety and avoid any damage to the detection coil, the reactor was cooled with a steady flow of pressurized air and insulated with a glass fiber mat.

6.2.4. MRSI experiments

All NMR experiments were performed on a small-bore NMR imaging system Biospec 70/20 USR (Bruker Biospin MRI GmbH, Ettlingen, Germany) equipped with a horizontal 7-Tesla magnet and a magnetic field gradient insert BGA12S2 (inner diameter: 116 mm, maximum gradient strength: 441 mT/m per spatial direction, switching time: 130 µs). A quadrature birdcage RF coil with an inner diameter of 72 mm was used for both RF transmission and signal reception.

For orientation, a multislice FLASH [37] sequence was applied with the following parameters: repetition time T_R: 500 ms, echo time T_E: 3 ms, 31 slices, slice thickness: 2.5 mm, slice distance (center-to-center): 3 mm, field-of-view (FOV): 48 mm × 48 mm, 256 × 256 matrix size, total measurement time: 2 min 8 s. In these images, the position of the glycol containing capsules was determined, while signals from the gases were lost because of the rather long T_E of 3 ms and the low gas concentration.

For the subsequent multislice MRSI experiments [38, 39], the position of the outer slices (slice #1 and #7) were chosen for measuring signals from the glycol capsules, while the inner five slices were used to detect the gases (cf. Figure 6.1). An optimized multislice MRSI pulse sequence was developed to realize an ultrashort echo time T_E, i.e. a delay between RF excitation and data acquisition, of only 350 µs. Thus, signal losses due to short effective transverse relaxation time T_2^* are reduced ($S(T_E) \sim \exp(-T_E/T_2^*)$). The asymmetric RF excitation pulse used for slice selective signal excitation was calculated by a Shinnar-Le Roux algorithm [40, 41] using the module of the Vespa suite for RF pulse design (available via: http://scion.duhs.duke.edu/vespa/). The pulse was optimized for a flip angle of 30°. The pulse duration was 250 µs and the maximum was about 70 µs prior to the end of the pulse. Immediately after the RF Pulse, short triangular-shaped phase encoding gradients (130 µs switch on, 130 µs switch off), were applied for in-plane resolution using a FOV of $63 \times 63\,mm^2$ and 42×42 phase encoding steps with circularly reduced k-space sampling [42]. Data acquisition was performed using 1 Ki complex data points and a spectral width of 50 kHz. Using a repetition time T_R of 155 ms the total time per SI measurement was about 3.5 minutes. Within each T_R, seven slices were sequentially measured with slice centers at -33 mm (#1), -24 mm (#2), -14 mm(#3), -4 mm (#4), 6 mm(#5), 16 mm(#6), 30 mm (#7) along the axial direction (z) of the reactor (cf. Figure 6.1) with higher z values pointing from the front side into the magnet. The slice order within T_R was #7, #6, ... , #1, i.e. opposite to the direction of the gas flow, to reduce saturation effects across the slices.

The temperature at the inner surface of the RF coil, measured by a fiberoptic thermometer (cf. section 6.3.1), increased during the observation of the gas reaction despite the thermal insulation between gas reactor and RF coil. Therefore, tuning and matching of the RF coil were manually readjusted after the temperature had changed by 3 K. Because of these interruptions (each lasting 1-2 minutes), MRSI data sets were not measured at equidistant time points.

MRSI data sets were processed using in-house developed IDL (Interactive Data Language, version 7.0, Exilis Visual Information Solutions, Bolder, USA) and Matlab (version 7.11.0, The MathWorks, Inc., Natick, MA, USA) programs. The measured k-space data were apodized with a Hamming function in the phase encoding direction (kx, ky) and zero filled to a matrix size of $64 \times 64 \times 1$ Ki. Zero filling to 8 Ki was also applied in the time domain prior to the 3D Fourier transformation (FT) of the data sets of all slices. Magnitude spectra were calculated for visual inspection of the data.

To approximate the volumetric fraction of ethylene and ethane, the peak area of both signals (I) were determined by integration, normalized by the number of attached hydrogen atoms per molecule and put into relation with each other:

$$\frac{c_{C_2H_6}}{c_{C_2H_4} + c_{C_2H_6}} \approx \frac{\frac{I_{C_2H_6}}{6}}{\frac{I_{C_2H_4}}{4} + \frac{I_{C_2H_6}}{6}}. \qquad (6.3)$$

A simple peak area integration in the magnitude spectra was not sufficient to reliably separate the ethylene from the ethane signals. Therefore, data was fitted in each voxel using the matrix pencil method (MPM) [43], which performs data fitting in the time domain by using a sum of exponentially decaying signals each being characterized by four parameters (amplitude, frequency, phase, decaying constant). While the maximum number

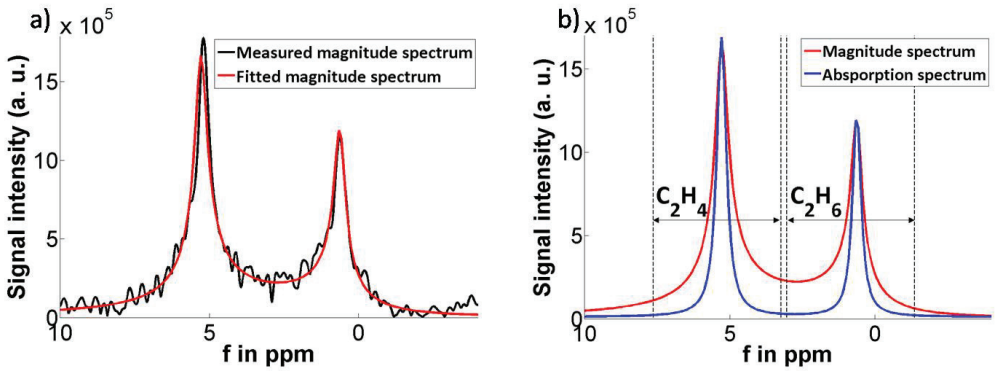

Figure 6.2.: (a) Typical magnitude spectrum measured of ethylene and ethane with superimposed MPM-fitted magnitude spectrum. (b) Fitted magnitude spectrum and the absorption spectrum to enhance signal separation: The signal peak of ethylene (C_2H_4) was integrated from 7.6 ppm to 3.2 ppm, the signal peak of ethane (C_2H_6) was integrated from 3.0 ppm to -1.4 ppm

of signals was set to two (ethylene, ethane), the number of signals was automatically determined to account for voxels with low signal-to-noise ratio (SNR) (e.g., outside the reactor or prior to the formation of ethane). Thus, for quantitative data analysis, data processing consisted of apodization and FT in phase encoding directions, MPM in all voxels, zero filling of the fitted and phase corrected data to 8 Ki data points, and FT in the time domain. As the phases of the fitted signals were set to zero, the real part of the complex FT spectrum corresponds to the absorption spectrum yielding better signal separation than the magnitude spectrum (cf. Figure 6.2). Images of the ethylene or ethane gas were calculated by peak area integration of these fitted absorption spectra. An alternative and more straightforward way for data quantification is, of course, to directly evaluate the amplitudes determined by the fitting routine. However, in individual voxels of some data sets, fitted noise peaks caused problems for the automatic signal assignment. Therefore, peak area integration in defined spectral regions of the FT spectra of the fitted time domain data was preferred to ensure a robust data quantification for the long series of 3D data sets.

For accurate temperature measurements by determining the chemical shift difference between the two glycol peaks, 8 Ki data points for a spectral width of 50 kHz are not sufficient. Therefore, the data for slices #1 and #7, were reconstructed by undersampling the time domain signal by a factor of 8 resulting in 8 Ki spectra for a spectral width of 6.25 kHz. Because of the very high SNR of the glycol signals, the corresponding SNR loss was not an issue. The straightforward alternative of zero filling to 64 Ki prior to FT would prolong data processing and may cause memory problems of the computer.

6.3. Results and discussion

The hydrogenation experiments were performed at different flow rates and initial hydrogen concentrations (cf. Table 6.1). Figure 6.3 shows a typical map of spectra measured during steady state operation mode in the middle of the catalyst bed. Only the inner 42×42 spectra of the reconstructed 64×64 matrix are shown to maintain visibility of the single spectra. Additionally, the spectra are scaled up by a factor of two to improve readability of spectra with broad resonance lines resulting from low B_0 homogeneity.

The map clearly shows the circular cross section of the catalyst bed. Despite intensity differences of up to a factor of ten, all voxels within the cross section are analyzable. The intensity differences arise from B_0 field inhomogeneities due to varying composition of the catalyst bed and temperature gradients along the cross section of the reactor. The chemical shift difference between the peaks of ethylene and ethane are in accordance with the expected values reported in literature [36]. During all experiments neither significant shifts of the peak positions nor exaggerated peak broadening was observed (cf. Figures 6.2 - 6.4). Outside the catalyst bed just noise is detected apart from a small circular area beneath the catalyst bed. We assume that this signal arises from small amounts of condensed water steam which could be carried by the

Table 6.2.: Results of the averaged volumetric concentration of ethane of experiment A and B measured by MRSI and pMS.

	Experiment A		Experiment B	
	t=1:31:52 h	t=1:43:15 h	t=1:13:52 h	t=1:21:29 h
Slice 5	16.1 vol.%	16.4 vol.%	9.8 vol.%	9.5 vol.%
Slice 6	14.4 vol.%	14.5 vol.%	10.0 vol.%	10.2 vol.%
pMS	18.0 vol.%	18.0 vol.%	11.0 vol.%	11.0 vol.%

pressurized air of the cooling circuit. Thus, the map of spectra and the achieved SNR clearly show that in spite of reactant flow conditions slice selective excitation and in-plane resolution by phase encoding is feasible by using the optimized ultrashort T_E MRSI pulse sequence.

To demonstrate that it is possible to detect the reaction progress along the catalyst bed, Figure 6.4 shows single spectra of the 5 inner slices at the same voxel position along the longitudinal axis of the reactor. It can be seen that the MPM fitting algorithm performs well in regard to the application case: The NMR signals are fitted as single peaks, however, only if the signal exceeds the noise level to a certain extent (cf. Figure 6.4a and 6.4b). For automatically determining the number of peaks, the AIC criterion of the MPM algorithm performed better than the MDL criterion [43], because the latter tended to miss peaks at lower SNR.

The progress of the reaction can be tracked along the spectra: in Figure 6.4a no ethane peak could be spotted. The ethane signal appears the first time in Figure 6.4b, increases in Figure 6.4c and stays stable in Figure 6.4d and 6.4e. The variation corresponds to the expected reaction progress along the catalyst bed.

Beside the variation of the peak ratios significant differences in signal intensity along the longitudinal axis of the reactor are noticeable. To investigate the signal intensity pattern, the peak areas of ethylene and ethane were added and plotted along the horizontal plane of symmetry. The resulting signal intensity profile of an experiment detected under steady state conditions (Experiment A, cf. Table 6.1) is shown in Figure 6.5. The signal intensity profile of a single slice shows significant similarities to the profile along all slices: both increase from the inside to the outside. This can be explained by the corresponding temperature profile along the axial and the radial direction of the catalyst bed: Due the structure of the catalyst bed, the conversion is mainly expected to take place within slices #3 to #5 and thus leading to higher temperature levels than in slices #2 and #6. Additionally, the peripheral zones of the catalyst bed are cooled by the cooling circuit. Both effects lead to u-shaped temperature profiles along the radial and longitudinal axis of the catalyst bed. Considering that the nuclear magnetization of a sample decreases with increasing temperature due to the Boltzmann distribution ($M_0 \sim \exp(-\Delta E/kT)$ with ΔE being the difference between the adjacent energy levels, k the Boltzmann constant and T the absolute temperature), the signal intensity should be lower in areas of elevated temperature.

Furthermore, the effect of isobaric conditions of the hydrogenation process has to be considered. In areas of elevated temperatures, the gas density and thus the spin density drops leading to an additional signal decrease. In the data set used Figure 6.5, the averaged total signal intensities of slice #2 and slice #4 differ by about 24 %. The temperature difference measured with a thermal couple at comparison measurements outside the reactor yielded about 45 K (110 °C, 65 °C; data not shown). If one calculates the expected intensity loss caused by decreased nuclear magnetization and density loss (assumption: ideal gas) alone, one would expect a signal difference of about 22 %. However, at least two further aspects have to be considered when explaining the observed regional differences in the NMR signals. First, for the MRSI pulse sequence used, the protons of the H_2 gas are NMR invisible due to the very short T_2^* relaxation time (e.g., $T_2^* \sim 200\,\mu s$ measured in separate experiments in a gas mixture of H_2 and CH_4 at room temperature, data not shown) and the strong diffusion [44] during the slice selective RF

pulse causing dephasing of the transverse magnetization. However, as part of the ethane molecule they become NMR visible and contribute to the measured spectra. Second, the T_1 and T_2 relaxation times may also be temperature dependent and could thus influence the observed signal profiles across the reactor because of saturation effects and signal losses during the echo time T_E.

6.3.1. Temperature measurements

Knowledge about the temperature conditions within a catalyst bed is crucial to evaluate process performances. To get information about inlet and outlet temperature of the catalyst bed, the spectra of ethylene glycol were measured in slices #1 and #7 by the multislice MRSI pulse sequence. As outlined above, the time domain data was fitted by the MPM algorithm and the absorption-like spectra were used for determining the chemical shift difference.

At least 16 ethylene glycol spectra of each capsule could be detected. The inner four spectra were used for temperature determination and the values were averaged (cf. Figure 6.6a). The resulting temperatures corresponded well to those measured with conventional thermocouples during comparison measurements outside the magnet. The temporally resolved temperature profiles of two experiments are shown in Figure 6.6b. The experiments A and B differ in regard to the volume flow and hydrogen content of the reactant gas (see. Table 6.1). As expected, the temperature profiles of both experiments differ considerably. The inlet temperature of experiment A is higher than the outlet temperature, with the difference being lower than 10 K. Opposite conditions are found in experiment B: Here the inlet temperature just increases slightly, whereas the outlet temperature is more than 50 K higher. The opposing temperature profiles are to be expected, because on the one hand the lower flow rate of experiment A promotes compensatory diffusional processes, which lead to lower temperature gradients. On the other hand the higher flow velocity of experiment B shifts the reactive zone, and thus higher temperatures, towards the outlet of the catalyst bed. These results demonstrate that the ethylene glycol capsules respond sensitively enough to temperature changes to map the temperature profiles within a catalyst bed. Due to the dimensions of the capsules, which are in the same order of magnitude as the catalyst pellets, we further assume no significant distortion impact on the flow pattern of the reactant gases.

As the gas composition was simultaneously measured in slices #2 to #6, this multislice MRSI approach yields information both on the spatial distribution of gases and on the temperature in the reactor. In the alternative case of temporally alternating measurements of gas distribution and temperature, one could perform the temperature measurements by volume selective spectroscopy measurement as demonstrated by Gladden et al. [27] in well defined voxels, allowing optimized shim values, i.e. better local B_0 homogeneity. However, using the global shim values used for multislice MRSI allowed precise and reproducible temperature measurements (cf., Figure 6.6). Therefore, the integration of gas distribution and temperature measurements within a multislice MRSI sequence was preferred to avoid any time delay between gas and temperature measurements.

6.3.2. Gas composition measurements

To estimate the gas composition in every voxel, the hydrogen conversion was calculated based on the ratio of the ethane peak area normalized to the number of attached hydrogen molecules divided by the sum of the normalized peak areas of ethane and ethylene (see Eq. 6.3). In each voxel, this ratio of normalized peak areas corresponds to the ratio between the volumetric concentration ethane and the sum of the volumetric concentrations of ethylene and ethane.

In pMS measurements only insignificant amounts of hydrogen were found at the outlet (Table 6.1). With this information the NMR pattern could be quantified in terms of hydrogen conversion X_{H_2}:

$$\frac{c_{C_2H_6}}{c_{C_2H_4} + c_{C_2H_6}} \cdot \alpha \approx X_{H_2}, \tag{6.4}$$

where α is a proportionality constant which can be calculated from the ratio of ethane concentration to the sum of ethene and ethane concentration at a known hydrogen conversion. Here the factor α was calculated based on the concentration conditions at the outlet measured by the pMS. By taking the inlet conditions into account (cf. Table 6.2), balance equations of each component, depending on the hydrogen conversion, can be set up:

$$\dot{v}_i = \dot{v}_{i,0} + \nu_i X_{H_2} \cdot \dot{v}_{H_2,0}, \tag{6.5}$$

where i refers to the chemical components present in the system (N_2, H_2, C_2H_4,C_2H_6), 0 indicates

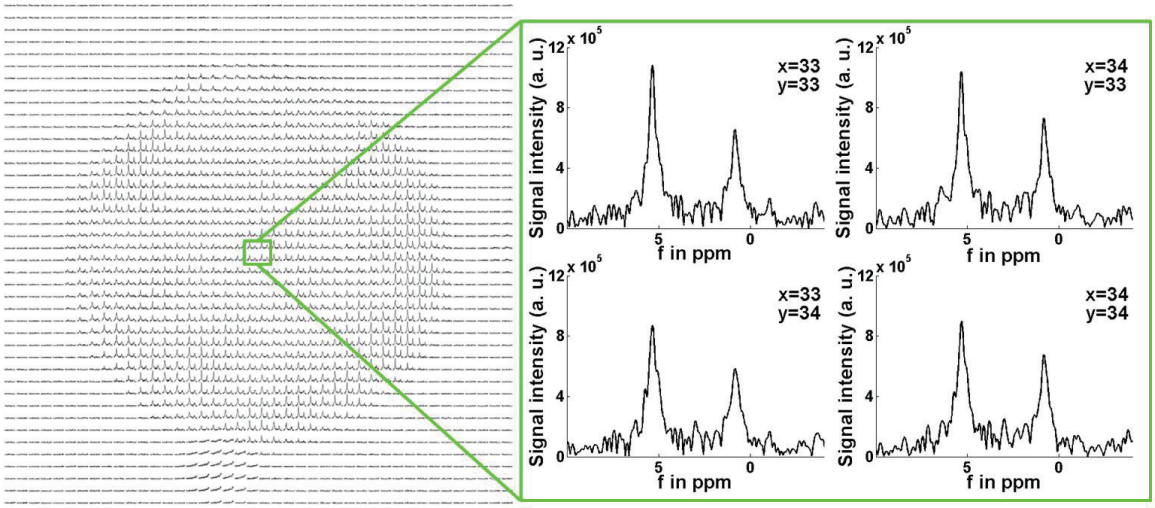

Figure 6.3.: Representative spectral map measured at steady state conditions: for improved readability only the inner 42×42 spectra of the measured 64×64 matrix is shown and the spectra are scaled up by a factor of 2.

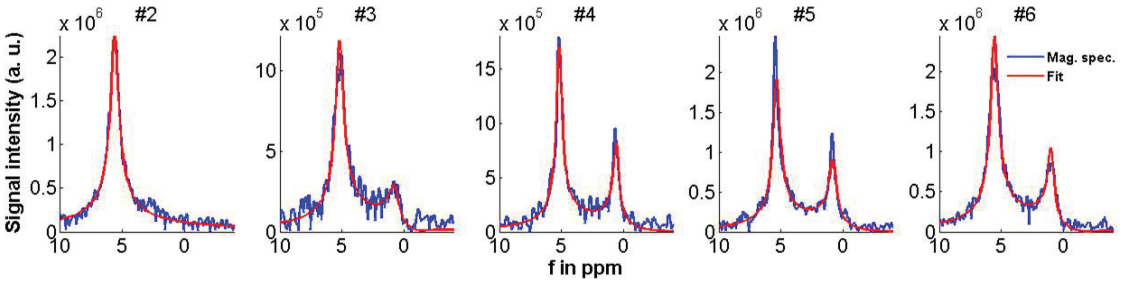

Figure 6.4.: Single spectra of the 5 inner slices at the same voxel position along the longitudinal axis of the reactor at reaction conditions with superimposed MPM-fits.

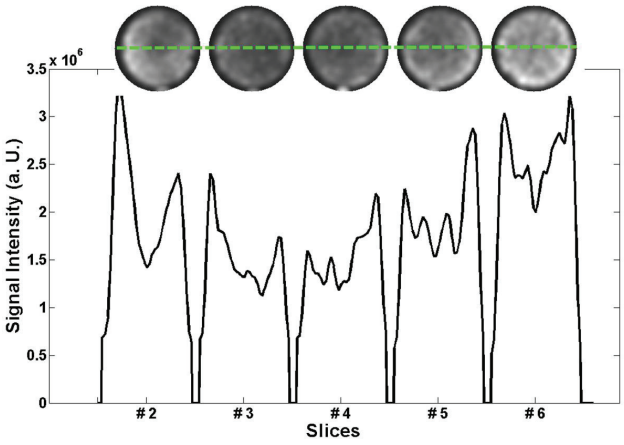

Figure 6.5.: Signal intensity of the sum of the peak area of ethylene and ethane added and plotted along the horizontal plane of symmetry.

the inlet conditions, $\dot{v}_i$ is the corresponding volume flow, and ν_i the stoichiometric factor of component i. Thus the volumetric concentration of ethane can be calculated in each voxel. The resulting concentration distribution of ethane for experiments A and B are shown in Figures 6.7 and 6.8, respectively.

For both experiments the spatial distribution of ethane is shown for four different points in time:

a) Only nitrogen and ethylene are flowing through the reactor. No hydrogenation should take place
b) Hydrogen is switched on. First measurement at transient reaction conditions
c) Measurement at steady state conditions as assumed from the temperature profile (Figure 6.6)
d) Comparison measurements at steady state conditions

The corresponding temperature measurements are shown in Figure 6.6 and the time points used for the data presented in Figure 6.7 and 6.8 are marked with red circles. The results of experiment A show clearly that a good signal separation is

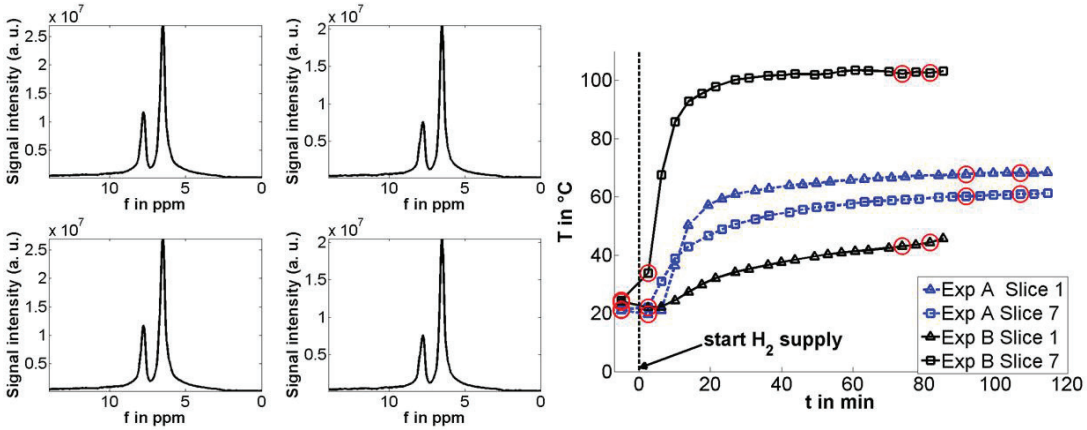

Figure 6.6.: Temperature profiles of the inlet and outlet of the catalyst bed of experiment A and experiment B. The temperatures were averaged over the four inner ethylene glycol spectra of the central capsule. All time information corresponds to the middle of the measurement duration.

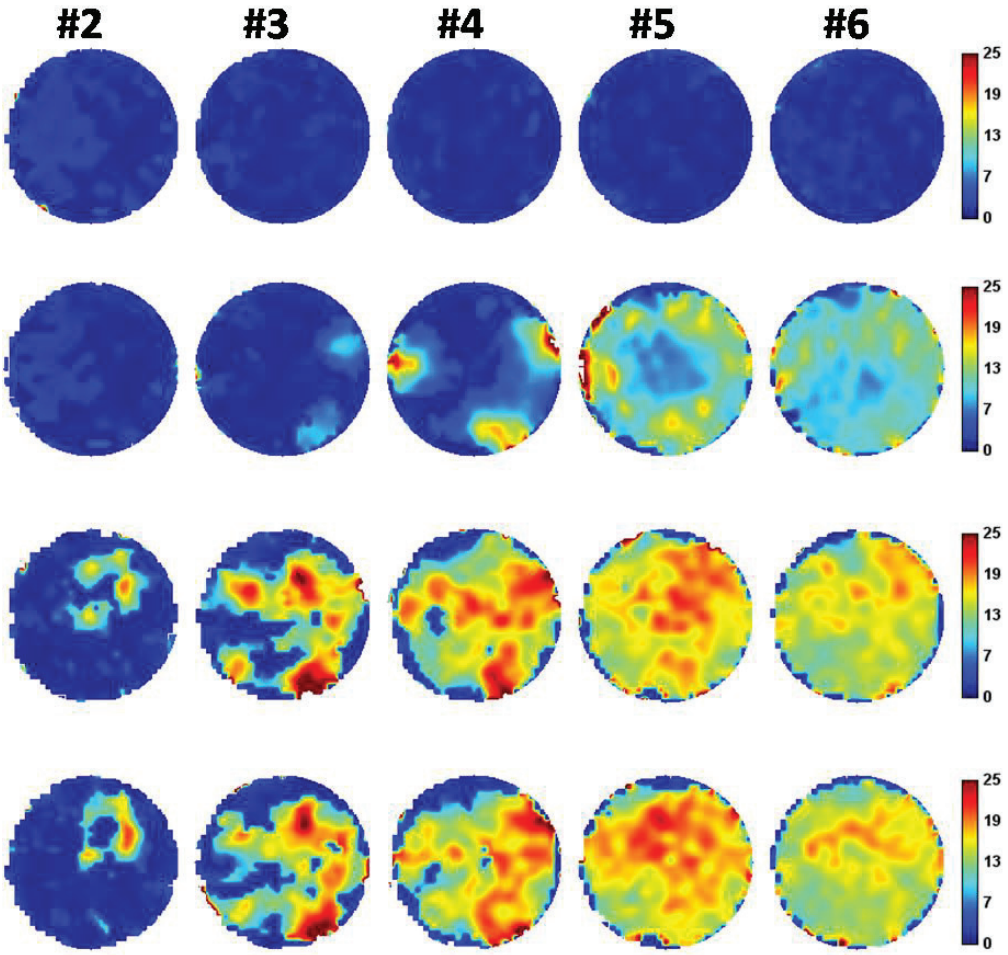

Figure 6.7.: Volumetric concentration maps of ethane of experiment A given in vol.%. The measurements (a–d from top to bottom) were performed at a. t = -5 min, b. t = 2:30 min, c. t = 1:31:52 h, and d. t = 1:43:15 h; All time information corresponds to the middle of the measurement duration.

achieved by fitting and phase correcting the signal: nearly no ethane is detected within the slices at t = -5 min. The next set of measurements (Figure 6.7b) presents the ethane concentration at transient reaction conditions: First small amounts of ethane can be detected in slice #3 and are in-

creasing towards the outlet of the catalyst bed. A detailed quantification of these amounts is not useful because the hydrogen conversion increased from 0 % to 80 % during the measurement time of about 3.5 minutes. The ethane concentration profile of a steady state measurement can be seen in Figure 6.7c. First locally limited zones with elevated ethane concentration can be detected in slice #2. Shape and position of these zones within the catalyst bed correspond to shape and position of single Pt-Al_2O_3-pellets that are surrounded by inert Al_2O_3-pellets which were inserted there.

With increasing ratio of catalyst pellets from slice #2 to #4 the number of active zones of the catalyst bed increase, but in all cases the active zones can still be clearly separated from each other. Thus it can be assumed that the zones of elevated ethane concentration are the active zones of the catalyst bed. Along the next two slices the amount of ethane increases, whereas the concentration gradients along the cross section decrease.

Slice #6 shows the most homogeneous concentration distribution. The concentration gradients are less pronounced compared to the previous slices. This reflects that a homogenization by mixing of the gases within the inert layer is achieved. The similarity of pattern in Figure 6.7c and 6.7d confirm the steady state assumption. Active zones can be detected at similar locations of the catalyst in all the slices. This demonstrates the reproducibility of the MRSI measurements.

Surprisingly, it appears that the averaged concentration of ethane decreases from slice #5 to slice #6. If one compares the averaged ethane concentration of slices #5 and #6, the apparent decrease of ethane content is confirmed (cf. Table 6.2). Whereas the averaged volumetric ethane concentration of slice #5 corresponds to the pMS measurements better than 90 %, the correspondence drops in slice #6 to 80 %. This can not be explained by an actual decrease of ethane, because the reverse reaction does not occur at the present reaction conditions and the pMS measures the gas composition behind the outlet of the reactor. This effect was also detected in different experiments with the same volume flow but varying hydrogen contents (data not shown). Additionally, flow effects like bypass flows at the wall area of the catalyst bed are also unlikely the reason for the apparent ethane decrease, since the ethane concentration is averaged across the overall cross section area of the catalyst bed. Thus, such an effect would have the same impact on the NMR based ethane concentration of slice #5, which was not noticed.

We hypothesize an NMR artifact, caused by saturation effects, leads to the apparent ethane decrease. With increasing slice index (in flow direction) the probability increases that spins that are to be measured have already been measured at an earlier time point in an adjacent slice. In particular, this applies to the ethane signal, which is only formed in the center of the reactor, and could thus suffer saturation. Thus an increasing percentage of ethane could be partially saturated, causing a signal decrease. However, we tried to minimize saturation effects by using 30° excitation pulses and measuring slices of 3 mm thickness with 10 mm center-to-center distance. In future experiments, we plan to examine the influence of saturation effects by performing single slice MRSI or using multislice MRSI with longer repetition time.

Additionally, measurements of the T_1 relaxation times of the gases will help to estimate saturation effects.

The results of experiment B (Figure 6.8a to 6.8d) demonstrate the influence of flow rate on spatial and temporal differences in the volumetric ethane concentration. In this experiment, the signal level of ethane is lower because of the lower hydrogen content in the reactant gas flow and the higher temperature in the reaction zones (cf. Figure 6.6) resulting from the higher flow velocity. Due to the lower SNR compared to experiment A, the fitting procedure failed to find an ethane peak in some voxels, particularly in slices #2 and #3. Nevertheless the experiment could be analyzed allowing the observation of the temporal and regional development of the ethane concentration in the reactor. Compared to Experiment A the reactive zones are shifted towards the outlet of the catalyst bed. This corresponds to the temperature profiles of Figure 6.6.

Apart from the lower amount of ethane present in the system, the active zones of the catalyst bed of experiment A and experiment B follow comparable pattern: The active zones of the transient measurement of experiment B are in the same position as in experiment A (cf. Figure 6.7b with Figure 6.8b, slices #3 and #4). The stationary measurements show also comparable active zones at the same position (cf. slice #3 and #4 of Figure 6.7c and 6.8d and slice #3 and #4 of Figure 6.8c and 6.8d). In accordance with experiment A

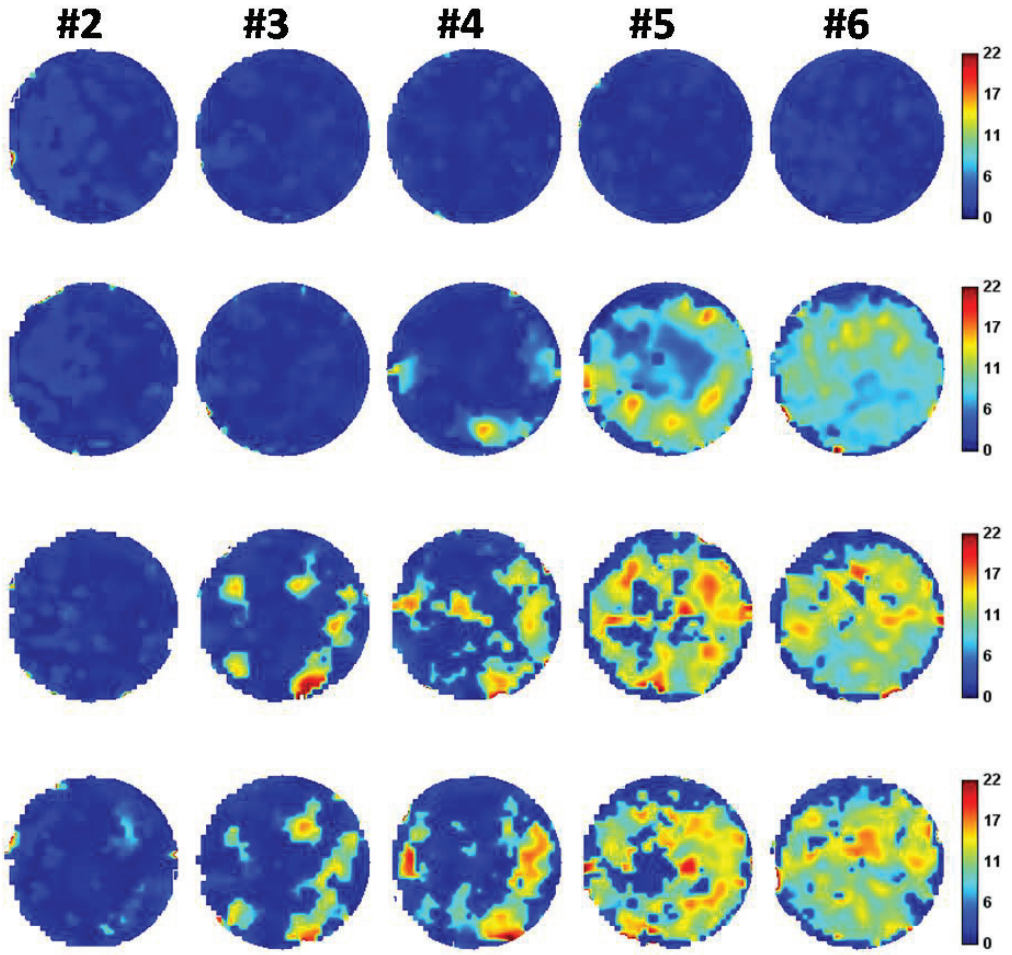

Figure 6.8.: Volumetric concentration maps of ethane of experiment B given in vol.%. The measurements (a–d from top to bottom) were performed at a. t = -5 min, b. t = 2:30 min c. t = 1:13:52 h and d. t = 1:21:29 h; All time information corresponds to the middle of the measurement duration.

both steady state measurements are comparable with each other. Both measurements show similar reaction zones and the averaged volumetric ethane contents of slices #5 and #6 deviate only slightly from each other (see Table 6.2), which underlines the reproducibility of the measurements.

The major difference between experiment A and experiment B is that in experiment B no decrease of ethane content between slices #5 and #6 was detected. The averaged volumetric ethane content of slice #6 corresponds to the pMS measurements better than 90 %. This might be a hint that saturation effects are the main reason for the apparent ethane decrease. Due the fact that the reaction zone is shifted towards the outlet of the catalyst bed, more ethane is produced between slices #5 and #6 and thus the extend of ethane saturation is lower than in experiment A, leading to lower deviation from the ethane concentration measured with the pMS. Nevertheless this effect will be addressed in the next experimental campaign as discussed above. Alternatively, measurements on non-reactive ethane/ethylene flows may help to explain why differences in the volumetric ethane concentrations between slices #5 and #6 were observed in experiments A, but not in experiment B.

6.4. Conclusion

The presented results prove that optimized ultrashort echo time multislice MRSI can successfully be applied to analyze heterogeneously catalyzed gas phase reaction systems at ambient conditions, despite the disadvantageous NMR properties of gaseous flows. Using the hydrogenation of ethylene as benchmark process, simultaneous spatial mapping of the chemical composition was demonstrated within five 3-mm-slices across a model reactor, an in-plane resolution of about 1.5 mm, and

a time resolution of about 3.5 minutes. It was possible to clearly and reproducibly identify the active zones of a catalyst bed, to follow the progress of the reaction along its longitudinal axis, and to separate and quantify the observed gases by using the matrix pencil method, a fast and robust time domain fitting algorithm. Further the multislice MRSI method allows to simultaneously measure the temperature within the catalyst bed. Expected temperature changes could be observed immediately in front of and after the active reaction zone, and characteristic differences between measurements with different hydrogen content and different volume flow were detected. Therefore, we are confident that ultrashort T_E multislice MRSI will be a powerful tool for optimizing heterogeneously catalyzed gas phase processes in model reactors and for validating modeling approaches.

There are certainly also a number of general disadvantages and technical challenges of the presented methodology. Compared to other methods used for NMR signal enhancing like remote detection or hyperpolarization, the presented approach suffers from lower SNR, particularly for higher temperatures. Nevertheless, it may be a method of choice for investigating gas phase reaction systems of larger macroscopic scale over longer time periods, because the experimental effort and the costs are rather low compared to approaches exploiting hyperpolarization, and the methods can be applied for slow flow through long reactors, unlike techniques using remote detection.

Additionally, the implemented method can be improved in several ways. Thus, an SNR increase will be possible if excitation RF pulses with optimized flip angle will be used based on knowledge on T_1 relaxation times and flow velocities. A further reduction of the echo time can be achieved, either by methodological improvements or improved hardware components, particularly faster B_0 gradients. Furthermore, data processing and quantification can be improved by adjusted and optimized procedures, e.g. by using prior knowledge about the chemical shifts.

The development of new NMR compatible reactors should focus on enabling measurements at higher temperature and higher pressure. Additionally, improving the thermal insulation and or the cooling of the outer reactor wall will be essential to avoid readjustments of the RF coil, and to allow a smaller distance between reactor and RF coil, thus yielding a higher filling factor and consequently a higher SNR.

We hope that the described methodology and the presented results will foster the application MRSI methods to investigate other heterogeneously catalyzed gas phase reaction systems and encourage multidisciplinary cooperation between researchers focusing on chemical engineering and NMR imaging methods.

Acknowledgment

We would like to thank Roswita Krebs-Goldbecker from the glass workshop of the University of Bremen for her obliging assistance with the manufacturing of the experimental setup. This work was in part supported by the German Research Foundation (DFG) within the Research Training Group GRK 1860 “Micro-, meso- and macroporous nonmetallic Materials: Fundamentals and Applications” (MIMENIMA).

References

1. Boudart, M., Davis, B. & Heinemann, H. in *Handbook of Heterogeneous Catalysis* (eds Ertl, G., Knözinger, H., Schüth, F. & Weitkamp, J.) 1–48 (Wiley-VCH Verlag GmbH, 2008).
2. LePage, J., Schlögl, R., Wainwright, M., Schü, F., Unger, K., Ko, E., Jacobsen, H., Kleinschmit, P., Menon, R. G., Delmon, B., Lee, K.-Y., Misino, M. & Oyama, S. in *Handbook of Heterogeneous Catalysis* (eds Ertl, G., Knözinger, H., Schüth, F. & Weitkamp, J.) 49–138 (Wiley-VCH Verlag GmbH, 2008).
3. Heck, R., Gulati, S. & Farrauto, R. The application of monoliths for gas phase catalytic reactions. *Chemical Engineering Journal* **82,** 149–156 (2001).
4. Chen, J., Yang, H., Wang, N., Ring, Z. & Dabros, T. Mathematical modeling of monolith catalysts and reactors for gas phase reactions. *Appl. Catal. A: General* **345,** 1–11 (2008).
5. Tronconi, E., Groppi, G. & Visconti, C. Structured catalysts for non-adiabatic applications. *Current Opinion in Chemical Engineering* **5,** 55–67 (2014).

6. Schildhauer, T., Pangarkar, K., van Ommen, J., Nijenhuis, J., Moulijn, J. & Kapteijn, F. Heat transport in structured packings with two-phase co-current downflow. *Chemical Engineering Journal* **185-186,** 250–266 (2012).

7. Vervloet, D., Kapteijn, F., Nijenhuis, J. & van Ommen, J. A convection-based single-parameter model for heat transport in multiphase tubular reactors packed with closed cross flow structures. *Chemical Engineering Journal* **233,** 265–273 (2013).

8. Gräf, I., Rühl, A.-K. & Kraushaar-Czarnetzki, B. Experimental study of heat transport in catalytic sponge packings by monitoring spatial temperature profiles in a cooled-wall reactor. *Chemical Engineering Journal* **244,** 234–242 (2014).

9. Mantzaras, J. New Directions in Advanced Modeling and in Situ Measurements Near Reacting Surfaces. English. *Flow, Turbulence and Combustion* **90,** 681–707 (2013).

10. Schneider, A., Mantzaras, J., Bombach, R., Schenker, S., Tylli, N. & Jansohn, P. Laser induced fluorescence of formaldehyde and Raman measurements of major species during partial catalytic oxidation of methane with large H_2O and CO_2 dilution at pressures up to 10 bar. *Proceedings of the Combustion Institute* **31,** 1973–1981 (2007).

11. Gross, E., Shu, X.-Z., Alayoglu, S., Bechtel, H., Martin, M., Toste, F. & Somorjai, G. In Situ IR and X-ray High Spatial-Resolution Microspectroscopy Measurements of Multistep Organic Transformation in Flow Microreactor Catalyzed by Au Nanoclusters. *Journal of the American Chemical Society* **136,** 3624–3629 (2014).

12. Zellner, A., Suntz, R. & Deutschmann, O. Two-Dimensional Spatial Resolution of Concentration Profiles in Catalytic Reactors by Planar Laser-Induced Fluorescence: NO Reduction over Diesel Oxidation Catalysts. *Angewandte Chemie International Edition* **54,** 2653–2655 (2015).

13. Zaera, F. New advances in the use of infrared absorption spectroscopy for the characterization of heterogeneous catalytic reactions. *Chemical Society Reviews* **43,** 7624–7663 (2014).

14. Koptyug, I. in *Spectroscopic Properties of Inorganic and Organometallic Compounds: Volume 45* (eds Yarwood, J., Douthwaite, R. & Duckett, S.) 1–42 (The Royal Society of Chemistry, 2014).

15. Gladden, L. Magnetic resonance in reaction engineering: beyond spectroscopy. *Current Opinion in Chemical Engineering* **2,** 331–337 (2013).

16. Stapf, S. & Han, S.-I. *NMR imaging in chemical engineering* (John Wiley & Sons, 2006).

17. Abragam, A. & Goldman, M. Principles of dynamic nuclear polarisation. *Reports on Progress in Physics* **41,** 395–395 (1978).

18. Bowers, C. & Weitekamp, D. Parahydrogen and synthesis allow dramatically enhanced nuclear alignment. *Journal of the American Chemical Society* **109,** 5541–5542 (1987).

19. Moulé, A., Spence, M., Han, S.-I., Seeley, J., Pierce, K., Saxena, S. & Pines, A. Amplification of xenon NMR and MRI by remote detection. *Proceedings of the National Academy of Sciences of the United States of America* **100,** 9122–9127 (2003).

20. Seeley, J., Han, S.-I. & Pines, A. Remotely detected high-field MRI of porous samples. *Journal of Magnetic Resonance* **167,** 282–290 (2004).

21. Koptyug, I., Lysova, A., Kulikov, A., Kirillov, V., Parmon, V. & Sagdeev, R. Functional imaging and NMR spectroscopy of an operating gas-liquid-solid catalytic reactor. *Applied Catalysis A: General* **267,** 143–148 (2004).

22. Gladden, L., Mantle, M. & Sederman, A. Magnetic resonance imaging of catalysts and catalytic processes. *Advances in Catalysis* **50,** 1–75 (2006).

23. Gladden, L., Akpa, B., Anadon, L., Heras, J., Holland, D., Mantle, M., Matthews, S., Mueller, C., Sains, M. & Sederman, A. Dynamic Mr Imaging of Single- and Two-Phase Flows. *Chemical Engineering Research and Design* **84,** 272–281 (2006).

24. Koptyug, I., Lysova, A., Sagdeev, R. & Parmon, V. Application of multinuclear MRI and solid state MRI in heterogeneous catalysis. *Catalysis Today* **126,** 37–43 (2007).

25. Lysova, A., Koptyug, I., Kulikov, A., Kirillov, V. & Sagdeev, R. An NMR Imaging Study of Steady-State and Periodic Operation Modes of a Trickle Bed Reactor. *Topics in Catalysis* **52,** 1371–1380 (2009).

26. Van Geet, A. Calibration of the Methanol and Glycol Nuclear Magnetic Resonance Thermometers with a Static Thermistor Probe. *Analytical Chemistry* **40,** 2227–2229 (1968).

27. Gladden, L., Abegao, F., Dunckley, C., Holland, D., Sankey, M. & Sederman, A. MRI: Operando measurements of temperature, hydrodynamics and local reaction rate in a heterogeneous catalytic reactor. *Catalysis Today* **155,** 157–163 (2010).

28. Bouchard, L., Burt, S., Anwar, M., Kovtunov, K., Koptyug, I. & Pines, A. NMR Imaging of Catalytic Hydrogenation in Microreactors with the Use of para-Hydrogen. *Science* **319,** 442–445 (2008).

29. Kovtunov, K., Beck, I., Zhivonitko, V., Barskiy, D., Bukhtiyarov, V. & Koptyug, I. Heterogeneous addition of H_2 to double and triple bonds over supported Pd catalysts: a parahydrogen-induced polarization technique study. *Physical Chemistry Chemical Physics* **14,** 11008–11014 (2012).

30. Zhivonitko, V., Telkki, V.-V., Leppaniemi, J., Scotti, G., Franssila, S. & Koptyug, I. Remote detection NMR imaging of gas phase hydrogenation in microfluidic chips. *Lab on a Chip* **13,** 1554–1561 (2013).

31. Roberts, S., Renshaw, M., Lutecki, M., McGregor, J., Sederman, A., Mantle, M. & Gladden, L. Operando magnetic resonance: monitoring the evolution of conversion and product distribution during the heterogeneous catalytic ethene oligomerisation reaction. *Chemical Communications* **49,** 10519–10521 (2013).

32. Jameson, C. Gas-phase NMR spectroscopy. *Chemical Reviews* **91,** 1375–1395 (1991).

33. Glover, P. & Mansfield, P. Limits to magnetic resonance microscopy. *Reports on Progress in Physics* **65,** 1489 (2002).

34. Ammann, C., Meier, P. & Merbach, A. A Simple Multinuclear NMR Thermometer. *Journal of Magnetic Resonance* **46,** 319–321 (1982).

35. Zaera, F. & Somorjai, G. Hydrogenation of Ethylene over Platinum (111) Single-Crystal Surfaces. *Journal of the American Chemical Society* **106,** 2288–2293 (1984).

36. Ebrahimi, H., Shaghaghi, H. & Tafazzoli, M. Gauge invariant atomic orbital-density functional theory prediction of accurate gas phase ^{1}H and ^{13}C NMR chemical shifts. *Concepts in Magnetic Resonance Part A* **38A,** 269–279 (2011).

37. Haase, A., Frahm, J., Matthaei, D., Hanicke, W. & Merboldt, K.-D. FLASH imaging: Rapid NMR imaging using low flip-angle pulses. *Journal of Magnetic Resonance* **213,** 533–541 (2011).

38. Brown, T., Kincaid, B. & Ugurbil, K. NMR chemical shift imaging in three dimensions. *Proceedings of the National Academy of Sciences* **79,** 3523–3526 (1982).

39. Maudsley, A., Hilal, S., Perman, W. & Simon, H. Spatially resolved high resolution spectroscopy by "four-dimensional" NMR. *Journal of Magnetic Resonance (1969)* **51,** 147–152 (1983).

40. Shinnar, M., Bolinger, L. & Leigh, J. The synthesis of soft pulses with a specified frequency response. *Magnetic Resonance in Medicine* **12,** 88–92 (1989).

41. Pauly, J., Le Roux, P., Nishimura, D. & Macovski, A. Parameter relations for the Shinnar-Le Roux selective excitation pulse design algorithm (NMR imaging). *IEEE Transactions on Medical Imaging* **10,** 53–65 (1991).

42. Maudsley, A., Matson, G., Hugg, J. & Weiner, M. Reduced phase encoding in spectroscopic imaging. *Magnetic Resonance in Medicine* **31,** 645–651 (1994).

43. Lin, Y.-Y., Hodgkinson, P., Ernst, M. & Pines, A. A Novel Detection-Estimation Scheme for Noisy NMR Signals: Applications to Delayed Acquisition Data. *Journal of Magnetic Resonance* **128,** 30–41 (1997).

44. Marrero, T. & Mason, E. Gaseous Diffusion Coefficients. *Journal of Physical and Chemical Reference Data* **1,** 3–118 (1972).

7. NMR imaging of gas phase reaction processes within monolithic catalyst supports

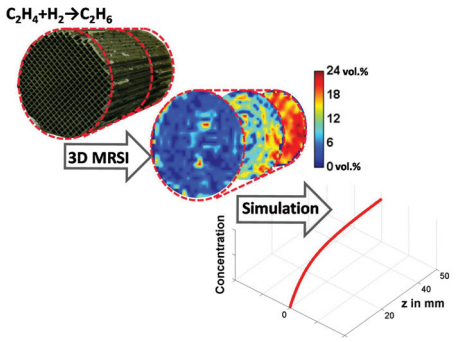

Adapted from:
In situ Analysis of Gas Phase Reaction Processes within Monolithic Catalyst Supports by applying NMR Imaging Methods
Published in:
Catalysis Today, Received 11.12.2015, Revised 08.02.2016, Accepted 10.02.2016
DOI: 10.1016/j.cattod.2016.02.062
Authors:
Jürgen Ulpts[a,*], Wolfgang Dreher[b], Lars Kiewidt[a], Miriam Schubert[a] and Jorg Thöming[a]

[a] University of Bremen, Center for Environmental Research and Sustainable Technology (UFT), Leobener Str. 6, 28359 Bremen, Germany
[b] University of Bremen, Department of Chemistry (FB2), in vivo MR Group, 28359 Bremen, Leobener Str. 2, Germany
[*] Corresponding author. Phone: +49 421 218 63466, E-Mail: julpts@Uni-Bremen.de

Abstract: Measuring spatially resolved concentration distributions in gas phase reaction systems is an important tool to validate simulation calculations, improve the understanding of transport processes within the catalyst, and identify potentials for improvements of monolithic catalyst supports. The commonly used measurement methods for such opaque systems are invasive and, thus, might be misleading due to alteration of the system.

To overcome this issue, a 3D magnetic resonance spectroscopic imaging (MRSI) method was developed and implemented on a 7-Tesla NMR imaging system to map the concentration distributions within opaque monolithic catalysts using the ethylene hydrogenation process as case study. The reaction was catalyzed by a coated sponge packing or a honeycomb monolith within an NMR compatible packed bed reactor. Temperatures at the inlet and the outlet of the catalyst beds were simultaneously determined by analyzing the spectra of inserted ethylene glycol filled glass capsules. Steady state concentration profiles and temperature levels were measured at different reaction conditions. In order to prove the plausibility of the measured spatial distributions of compound concentrations, the experimental results were compared to a 1D model of the reactor based on kinetic data from literature. Furthermore, a comparison with integral concentration measurements using a mass spectrometer demonstrated deviations below 5 %. The results show that 3D MRSI is a valuable and reliable tool to non-invasively measure spatially resolved process parameters within optically and/or mechanically inaccessible structured monolithic catalyst supports, even if only standard thermal polarization is exploited and the use of expensive and technically challenging signal enhancement techniques (hyperpolarization) is avoided. We expect that 3D MRSI can pave the way towards deeper insight into the interactions between catalyst, catalyst support, and gas phase.

7.1. Introduction

Within the last decades structured catalyst supports became a valuable option to enhance the performance of heterogeneously catalyzed reaction processes. Their beneficial properties, like low pressure drop and adjustable heat transport characteristics, are especially suitable to intensify gas phase reaction processes with elevated exothermicity [1–3]. Despite the wide application of monolithic catalysts in environmental catalysis, reliable and validated reactor models are still necessary to identify enhancement potentials when applying structured catalysts. However, the validation of modeling approaches of reaction systems with structured catalyst supports is still challenging due to the typically inaccessible and opaque nature of these supports, which makes non-invasive measurements of temperature and chemical concentration of the reactive flow within the catalyst bed rather difficult.

Although invasive methods such as suction probe techniques and thermometers provide only low spatial resolution and might lead to significant increase of the local residence time when applied for monolithic catalysts [4], they are still state-of-the-art and frequently applied in current research [3, 5, 6]. Another approach to map chemical compositions and temperature non-invasively, particularly in optically opaque reaction systems, are nuclear magnetic resonance (NMR) based methods, which are well established in biomedical diagnostics and analytical chemistry, and have also found various applications in material sciences and chemical engineering [7]. Several studies on investigating 3-phase reaction systems [8–10] with NMR techniques have been published, in which signal detection was mainly based on the liquid phase. Also gas phase processes have been investigated by NMR imaging and spectroscopy. In addition to the general difficulties associated with NMR measurements, like low inherent sensitivity and the required NMR compatibility of the reactor, the low spin density and rather short transverse relaxation times of gases make such measurements particularly challenging [11, 12]. To overcome this issue, signal enhancement can be achieved by para-hydrogen induced hyperpolarization [13, 14] or remote detection techniques [15, 16], which are of particular interest for microreactors and systems with rather short residence times of the gas molecules. However, macroscopic reaction systems can also be investigated by using thermal polarization and standard volume radiofrequency (RF) coils, as recently demonstrated by applying ultrashort echo time multislice magnetic resonance spectroscopic imaging (MRSI). In that study a gas phase hydrogenation was characterized in a packed bed flow reactor containing Pt-Al_2O_3 pellets [17].

In this study, we demonstrate that MRSI can be successfully applied to look inside ceramic monolithic catalysts of macroscopic scale (Ø> 20 mm) under reaction conditions. We show how NMR measurements can help to understand the influence of the monolithic catalyst support on heat and mass transport in a gas phase process. To this end, we optimized and applied a 3D MRSI method. This approach allowed to measure both the spatial distribution of the reactants and products within two different monolithic catalyst supports using the ethylene hydrogenation as a model reaction, and the temperature at the inlet and outlet of the reaction zone. Furthermore, the experimental results are compared to predictions of a 1D model of the reactor.

7.2. Experimental

7.2.1. Materials

Three stacked γ-Al_2O_3-sponge segments (length: ∼20 mm front and back segment and ∼10 mm central segment (cf. Figure 7.1a), diameter: 25 mm, 10 PPI; open porosity: 81 %, Drache GmbH, Diez, Germany) and a cordierite honeycomb monolith (length: 50 mm, diameter: 25 mm, 600 cpsi, NGK, Poland) were used as monolithic catalyst supports.

All monoliths were coated with a 1 wt.% Pt/Al_2O_3 catalyst layer. To this end, tetraammine -platinum(II)chloride hydrate (Sigma-Aldrich, St. Louis, USA) was dissolved in water and mixed with an aqueous suspension containing γ-Al_2O_3 (BASF Catalyst Germany GmbH, Nienburg). After stirring the suspension for about 5 minutes, the monoliths were dipped into the suspension. Then, excessive material was blown off with compressed air. All samples were dried first at 120 °C and then at 490 °C, each for 3 h. The amount of catalytic material coated on the surface of the catalyst substrates was determined by weighting the substrates before and after coating and calcinating: The amount of coating material was approximately 1.6 g at the sponge segments and about 1.5 g at the honeycomb monolith. Prior to the experiments, the catalysts were activated using a gas flow of 2.5 Nl/min (H2:N2 1:5) at a temperature of 400 °C for about 2 h.

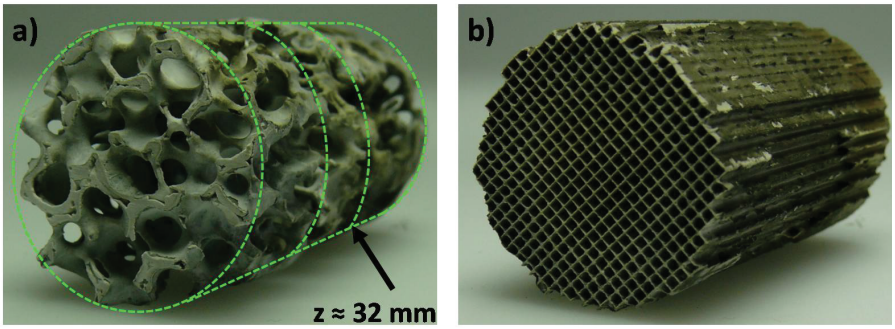

Figure 7.1.: (a) The monolithic sponge packing used in the first set of experiments consisted of three stacked 10 PPI sponge segments with 25 mm diameter and 20 mm (front and back segment) resp. 10 mm (central segment) length; the green dotted lines indicate the positions of the segments. The arrow indicates the position of the sponge cross section shown in Figure 7.4a. (b) Picture of the coated cordierite honeycomb monolith (600 cpsi) used in the second set of experiments.

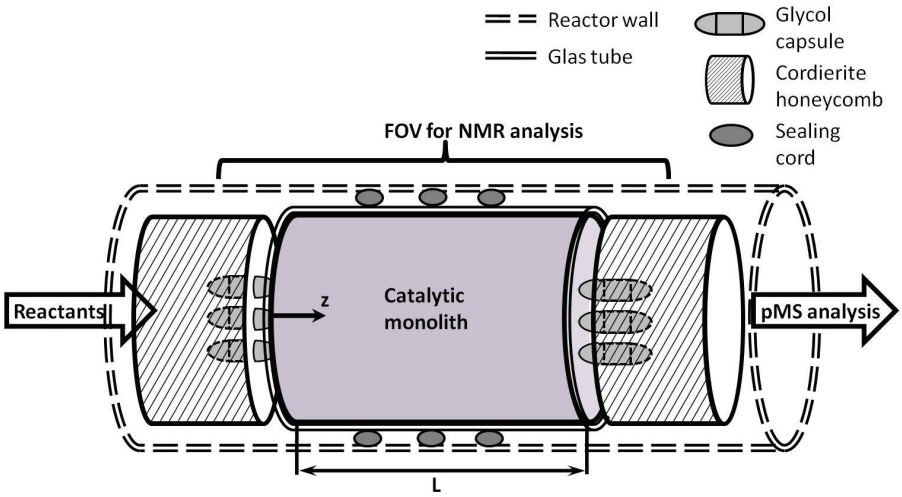

Figure 7.2.: Scheme of the experimental setup. The flow direction was from left to right.

7.2.2. Ethylene hydrogenation

The reaction of choice was the exothermal hydrogenation of ethylene (ΔHR = -137 kJ/mol at 298 K) because it can be operated at ambient conditions, it selectively yields a single product (ethane), and, due to the symmetry of ethylene and ethane, both gases give rise to single resonance lines in ^{1}H NMR spectra. In addition, the chemical shift difference between the two signals is larger than 4 ppm [18], which facilitates signal separation. Furthermore, the availability of a broad set of kinetic data [19–21] for the Pt catalyzed ethylene hydrogenation allows the formulation of a simple rate expression which should meet a good level of accuracy for the applied reaction conditions (cf. section 7.2.4).

The hydrogenation reaction was carried out within an NMR compatible glass reactor, which was cooled with pressurized air. The measurement range was arranged as follows (cf. Figure 7.2): For constraining the reactive zone to a given area without any bypass flows or dead zones, the catalytic monoliths were tightly fitted into a glass tube (inner diameter: 25 mm; wall thickness: 1.5 mm; length: 51 mm). The tube containing the catalytic monolith was in turn positioned inside the NMR compatible reactor. The resulting gap between glass tube and inner reactor wall was sealed with glass fiber sealing cord.

To measure the temperature at reproducible positions at the inlet and the outlet, ethylene glycol filled glass capsules were inserted into uncoated honeycomb segments (Ø25 mm; length 25 mm; 600 cpsi), which were placed in front of and behind the catalytic monolith. Details of this temperature measurement method were described in a previous study [17]. To avoid flow disturbances and crosstalk of the ethylene glycol signal into the reactive zones, a gap of about 3 mm was left be-

Table 7.1.: Experimental parameters (volume flow, concentration, temperature, velocity) of the low and high flow rate experiments on the sponge packing and the honeycomb. The volumetric concentrations were measured with a pMS behind the outlet of the reactor. The concentration measurements were performed at steady state conditions. For all experiments the measurement uncertainty of the pMS was below 0.5 %. The measurement uncertainty of the temperature measurements derived from the ethylene glycol spectra and was below 1.5 °C.

	Low flow rate experiment (sponge)	High flow rate experiment (sponge)	Low flow rate experiment (honeycomb)	High flow rate experiment (honeycomb)
Inlet:				
$\dot{v}_{Ar}$ in Nl/min	0.175	0.40	0.175	0.40
$\dot{v}_{C_2H_4}$ in Nl/min	0.22	0.50	0.25	0.50
$\dot{v}_{H_2}$ in Nl/min	0.078	0.10	0.075	0.10
Linear velocity in cm/s	1.6	3.4	1.7	3.4
T in °C (on rotational axis)	56	32	50	32
Outlet:				
c_{Ar} in vol.%	41.6	44.0	41.8	44.4
$c_{C_2H_4}$ in vol.%	39.6	44.3	39.4	43.9
$c_{C_2H_6}$ in vol.%	18.0	11.0	18.0	11.0
c_{H_2} in vol.%	0.8	0.7	0.8	0.7
T in °C (on rotational axis)	65	117	61	106

tween the uncoated honeycomb segments and the catalytic monolith.

The process conditions were kept comparable to earlier ethylene hydrogenation studies [17]: The reactant gas supply of the reactor with argon, hydrogen and ethylene was realized by mass flow controllers (F-201CV, Bronkhorst, Ruurlo, Netherlands, FMA-2618-A, Omega Engineering, Stamford, USA).

To explore the limits of the 3D MRSI method, the total initial volume flow was set to either about 0.4 Nl/min or 1.0 Nl/min with different hydrogen content in the reactant gases. The corresponding experiments are referred to as "low flow rate experiment" and "high flow rate experiment" in the following text (cf. Table 7.1). The outlet pressure was held at a constant level of 1.3 bar (abs). Behind the reactor outlet, the composition of the product gases was analyzed by a process mass spectrometer (pMS, GAM 200, InProcess Instruments, Bremen, Germany).

7.2.3. MRSI experiments

All NMR experiments were performed on a 7 Tesla preclinical NMR imaging system (Biospec 70/20, Bruker Biospin GmbH, Etlingen, Germany) equipped with a magnetic field gradient system BGA12S2 with a maximum gradient strength of 441 mT/m per direction (x,y,z) and a rise time of 130 µs. A circularly polarized RF coil with an inner diameter of 72 mm was used for both RF transmission and signal detection.

Based on the multislice MRSI pulse sequence used in a previous study [17], a 3D MRSI sequence was developed and then applied with the following parameters: repetition time T_R=12.5 ms; flip angle: 15°, echo time T_E=0.35 ms; spectral width: 25 kHz; 256 complex data points per acquired time domain signal; matrix size for a non-isotropic spatial resolution (in x,y,z): 63 × 63 × 49 with elliptically reduced phase encoding; field-of-view (FOV): 63 × 63 × 105 mm^3; The slice thickness in z direction was adjusted to the FOV. The total measurement time was about 20.1 minutes and every measurement was repeated three times. Note that the short echo time, i.e., the delay between RF excitation and the start of data acquisition was achieved by using an optimized asymmetric RF pulse and a short duration of phase encoding of 260 µs in all three directions.

For visual inspection, data processing consisted of apodization (multiplication) of the measured raw data using a Hamming function followed by a 4D Fast Fourier Transform (FFT) and magnitude calculation.

For quantitative data evaluation, data fitting was performed using the matrix pencil method (MPM) [17, 22–24], which approximates the measured time domain data by a sum of exponentially decaying signals each being defined by four parameters (amplitude, frequency, phase, decay constant). To this end, apodization and a 3D FFT in three spatial directions was performed followed

by MPM fitting of the time domain data in each voxel (cf. Figure 7.3). The performance of MPM for quantifying noisy spectroscopic NMR time domain data was investigated in [23] and [24], emphasizing the excellent estimation accuracy and the low breakdown "signal-to-noise" (SNR) threshold.

To quantify the volumetric fraction of ethylene and ethane, the maximum number of signals was set to two (ethylene, ethane). This was appropriate because the hydrogen signal of H_2 gas was not detected due to its very short transverse relaxation time. In each voxel, the number of signals was automatically determined (0, 1 or 2) to account for voxels with low signal-to-noise ratio (SNR) (e.g., outside the reactor) or regions where ethane was not or not yet produced. The amplitudes determined by the MPM algorithm were assigned to their corresponding chemical component on the basis of the associated frequency. The ethane/ethylene ratio was determined by normalizing the amplitudes to the number of attached hydrogen atoms per molecule and dividing the normalized amplitudes. This procedure was chosen to avoid unnecessary integration errors, particularly for regions with broad resonance lines where signal overlap may lead to an overestimation of the smaller component.

The MRSI data sets of this study were processed using in-house developed IDL (Interactive Data Language, version 7.0, Exilis Visual Information Solutions, Bolder, USA) and Matlab (version 7.11.0, The MathWorks, Inc., Natick, USA) programs.

7.2.4. Modeling approach

For the simulations, we used a pseudo homogeneous 1D fixed bed reactor model that combines the fluid and solid phase into a single effective phase and thus neglects interfacial heat and mass transfer. Neglecting interfacial mass transfer in this case is justified because of the Mears' criterion calculated in the Appendix. Furthermore, based on the temperature measurements, we assume isothermal conditions for the low flow rate experiment. In addition, pressure is considered to be constant because of the short reactor and high gas permeabilities of the catalyst supports. Consequently, an overall mass balance and n species mass balances are necessary to describe the process with sufficient physical accuracy. The balance equations read:

$$\frac{\mathrm{d}G}{\mathrm{d}z} = 0 \tag{7.1}$$

$$G\frac{\mathrm{d}\omega_i}{\mathrm{d}z} = M_i \sum_{j=1}^{n_r} \nu_{ij}\eta_j r_j^{(V)}, i = 1...n_s \tag{7.2}$$

Here $G = \rho\epsilon v_z$ describes the gas load, which remains constant along the catalyst bed due to mass conservation. It is a product of the fluid density ρ, the porosity of the catalyst bed ϵ, and the longitudinal fluid velocity v_z. ω_i refers to the mass fraction, M_i to the molar weight, η_i to the effectiveness factor and ν_i to the stoichiometric coefficient of the respective component i. n_r is the number of species of the reaction system. The effectiveness factor η_i, accounting for mass transport limitations within the porous catalyst, is considered to be unity because of the thin catalyst layers on the supports (approximately 6 µm and 20 µm for honeycomb and sponge, respectively, cf. A.1.1) and the low temperatures (see estimation of the Thiele modulus in the Appendix, A.1.1). The balance equations were subject to Dirichlet boundary conditions:

$$G\left(z = 0\right) = G_0 \tag{7.3}$$

and

$$\omega_i\left(z = 0\right) = \omega_{i,0}, \tag{7.4}$$

where 0 indicates inlet conditions.

The density is calculated from the ideal gas law:

$$\rho = \frac{pM}{R_\mathrm{u}T}. \tag{7.5}$$

Here, R_u is to the universal gas constant and T the temperature of the system.

An explicit expression for the reaction rate $r_j^{(V)}$ was derived from kinetic data from the literature. For the occurring reaction conditions the expression for the reaction rate was assumed to follow a power rate law:

$$r^{(Site)} = A\exp\left\{-\frac{E_\mathrm{a}}{R_\mathrm{u}T}\right\}\left(p_{\mathrm{H_2}}^m p_{\mathrm{C_2H_4}}^n\right), \tag{7.6}$$

where $r^{(Site)}$ is the reaction rate per active surface site of the catalyst, A is the pre-exponential factor, and E_a is the activation energy of the catalyst. Since the partial pressure of ethylene, $p_{\mathrm{C_2H_4}}$, was much higher than 7 kPa during all experiments, the reaction order of ethylene m was set

to zero [25]. The expression for the rate equation (Eq. 7.6) was then fitted to kinetic data published in [19], wherein the reaction order or the partial pressure of hydrogen, p_{H_2}, was found to be 1.18 ± 0.2 and $E_a = (37 \pm 0.63)$ kJ mol^{-1} (cf. Figure A1). These values are in good agreement with other data from literature [25].

The pre-exponential factor A could not be derived from the kinetic data due to uncertainties regarding the quantity of active sites of the catalysts investigated in [19]. Hence, A was adapted to the MRSI results shown in section 7.3.2. Note that, due to the adaption, the pre-exponential factor A might not only account for collision frequency and the probability of matching orientation of the reactant molecules, but could in principle also account for mass transport within the washcoat. Nevertheless, the estimation of the effectiveness factor η_i (cf. Appendix) indicates that this macro kinetic effect is negligible. Furthermore, the effect of dispersion of the Pt-catalyst on the reaction rate is also lumped in the pre-exponential factor A, since data on Pt-dispersion could not be derived from the kinetic study published in [19].

Thus, it is assumed for reasons of simplification that the amount of catalyst, m_{Pt}, is homogeneously distributed on the catalyst surface, the active site related reaction rate, Eq. 7.6, was used to calculate the volumetric reaction rate by relating the amount of catalyst to the total volume of the catalyst bed V_{tot}, and the molar weight M_{Pt}:

$$r^{(V)} = r^{(Site)} \frac{m_{Pt}}{V_{tot} M_{Pt}} \tag{7.7}$$

The system of differential equations of the 1D model was solved numerically using well established integration libraries [26, 27]. The pre-exponential factor A was determined by minimizing the difference between the experimental and model results in a root-mean-square sense [28].

7.3. Results and discussion

Due to the axial resolution of the 3D MRSI method 22 slices could be utilized to track the reaction progress along the catalyst bed. Eight typical normalized magnitude spectra measured on the sponge and the honeycomb are shown in Figure 7.3a and Figure 7.3b, respectively. The spectra originate from the same voxel position along the longitudinal axis of the reactor.

Both sets of spectra profiles follow the same pattern: In the first spectra no or just insignificant amounts of ethane were detected. The ethane signal then increases along the first half of the reactor length and subsequently remains stable at the last three to four spectra. To demonstrate the performance of the applied fit routine (cf. section 7.2.3), the second and last spectrum of the diagrams are shown with superimposed MPM-fitted magnitude spectra.

In accordance with former NMR studies [17] on ethylene hydrogenation a significant shift of the positions of the spectral peaks could not be observed with one exception: The ethylene peak of the first spectra of Figure 7.3a and Figure 7.3b is shifted by up to 2 ppm compared to the other ethylene peaks. This might result from B_0 changes, due to the transition between pure gas and catalytic monolith, which should be located there. The elevated SNR of the first spectra compared to the following spectra supports this explanation because of the higher signal from voxels with free gas compared to voxels containing also solid material.

The comparably small peak width of all observed spectra implies that the NMR signal primarily arises from the ethylene and ethane molecules of the gas phase and not from surface-adsorbed molecules. For comparison, spectra of an adsorbed and free gas ethylene/ethane mixture are shown in Figure A2. This assumption is supported by the comparably high SNR variation in Figure 7.3a (sponge) compared to Figure 7.3b (honeycomb): The material of the honeycomb is significantly more permeable to gas than the struts of the Al_2O_3 sponge (cf. Figure 7.4a and Figure 7.5a). Thus in spectra, which are measured in voxels with a high amount of solid material, like sponge struts, the amount of detectable gas is lower, hence the SNR decreases, and this may reduce both precision and accuracy of spectrum analysis (cf. second and fourth spectrum in Figure 7.3a). However, this effect of SNR decrease allows for deducing macroscopic morphological properties of gas impermeable catalyst support structures (cf. Figure 7.4b).

7.3.1. Spatially resolved gas concentration analysis

The results of the spatially resolved gas MRSI analysis demonstrate that the NMR patterns match the porous structures of the investigated catalytic supports. Due to its macroscopic dimensions, the analysis of the sponge packing enables to detect the position and shape of the macro pores and structure depending reaction zones, whereas the

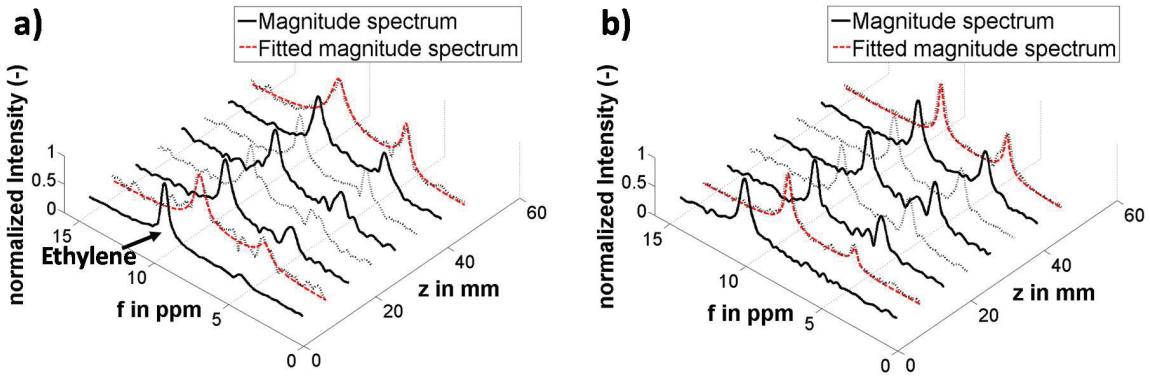

Figure 7.3.: Magnitude spectra measured in (a) the sponge catalyst support and (b) the honeycomb catalyst support at the same voxel position along the longitudinal axis of the reactor. The measured magnitude spectra were normalized by their maximum value and plotted alternating with solid and dashed lines for better readability. Additionally each second and last spectrum of the diagrams are shown with the corresponding MPM-fitted magnitude spectrum superimposed (red). The spectra were acquired at reaction conditions of the configuration "low flow rate" (cf. Table 7.1).

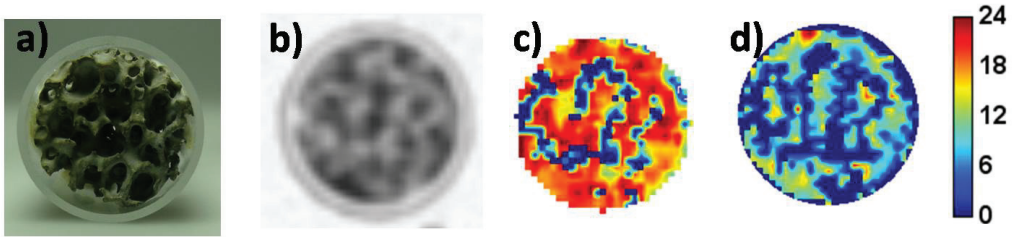

Figure 7.4.: (a) Photographic image of the cross section of the catalytic sponge packing at z = 32 mm. (b) NMR ethylene image (with inverted grey scale) of the cross section of the catalytic sponge packing at z = 32 mm measured by 3D MRSI during a constant flow of a non-reactive mixture of ethylene and argon.(c) Volumetric ethane concentration map of the low flow rate experiment of the catalytic sponge packing at z = 32 mm (d) Volumetric ethane concentration map of the high flow rate experiment of the catalytic sponge packing at z = 32 mm. All concentrations are given in vol.%.

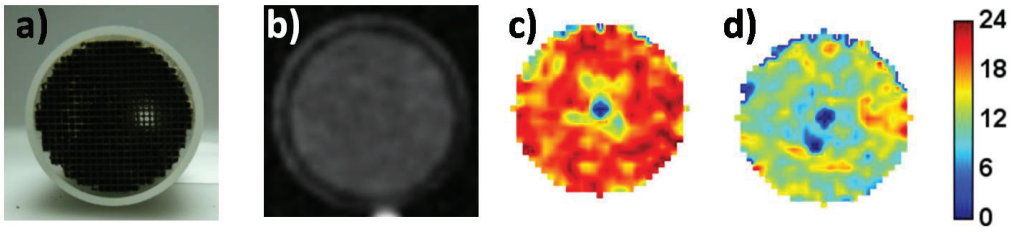

Figure 7.5.: (a) Photographic image of the cross section of the honeycomb catalyst (b) NMR ethylene image of the cross section of the honeycomb catalyst at z = 32 mm measured by 3D MRSI during a constant flow of a non-reactive mixture of ethylene and argon. (c) Volumetric ethane concentration map of the low flow rate experiment of the honeycomb catalyst at z = 32 mm (d) Volumetric ethane concentration map of the high flow rate experiment of the honeycomb catalyst at z = 32 mm. All concentrations are given in vol.%.

analysis of the honeycomb (600 cpsi) allows for conclusions concerning the overall reaction process and the distribution of the catalytic coating.

Figure 7.4a shows a photographic image of the cross section of the sponge packing. The cross section was located at the interface between the second and the third sponge segment of the catalytic sponge packing (z=32 mm, cf. Figure 7.1a). A corresponding NMR image is shown in Figure 7.4b. This image of ethylene was measured by MRSI during a constant flow of a non-reactive mixture of ethylene and argon. For the sake of comparability with Figure 7.4a, the grey scale of image 7.4b was inverted, i.e., black represents high signal intensity and white low signal intensity. The comparison of Figure 7.4a and 7.4b demonstrates that the

macroscopic morphology of the sponge can be determined by MRSI at flow conditions. Significant pore structures, which are shown in Figure 7.4a, are also clearly recognizable in Figure 7.4b. The glass casing of the catalyst bed is also delineated in Figure 7.4b, marked by a bright ring, which surrounds the sponge cross section. The grey ring shaped area which surrounds the glass casing, results from ethylene molecules that permeate the gap filled by the sealing cord between glass casing and reactor wall (cf. Figure 7.2).

Figure 7.4c and Figure 7.4d show the resulting ethane concentration maps of the low and high flow rate experiments, respectively (cf. Table 7.1). The concentration maps were calculated based on the ethane/ethylene ratio determined from the 3D MRSI data as well as the inlet and outlet conditions. The procedure is described in detail in [17]. The concentration pattern corresponds to the position of the pores. Thus, the reaction product is mainly detectable in areas with a high share of pore volume.

In comparison with Figure 7.4c the concentration distribution within the pores of Figure 7.4d appears to be more heterogeneous. This can be explained by the different reaction conditions (cf. Table 7.1): Due to the increase of flow velocity in the high flow rate experiment, the residence time is decreased and the process shown in Figure 7.4d has not reached its maximum conversion at that position (cf. Figure 7.6). Hence the gas molecules inside the sponge packing are not evenly distributed within all pores of the sponge, and areas with higher and lower reactivity are still distinguishable.

In order to compare the results of the sponge packing with the honeycomb experiments, Figure 7.5a shows a photographic image of the honeycomb cross section and Figure 7.5b shows an NMR image of ethylene measured during a constant flow of a non-reactive mixture of ethylene and argon. Figure 7.5c and Figure 7.5d depict ethane concentration maps of the low (Figure 7.5c) and high flow rate experiments (Figure 7.5d) at z=32 mm, respectively. Note that in Figure 7.5b, the grey scale was not inverted, i.e., white corresponds to high signal intensity.

In contrast to Figure 7.4a and 7.4b, the macroscopic structures of the honeycomb are not visible in the MR image shown in Figure 7.5b. The signal intensity is homogenously distributed within the cross section of the honeycomb. The reasons for this are twofold: On the one hand the cordierite honeycomb is permeable to gas, thus gas molecules inside the ceramic structures of the honeycomb produce an NMR signal and the signal intensity is not significantly lowered there. On the other hand the cells of the honeycomb are too small to be sufficiently resolved using the present MRSI voxel size. Future MRSI studies with improved spatial resolution will require stronger phase encoding gradients, which may cause technical problems due to the limited maximum gradient strength and signal distortions by gradient induced eddy currents. The alternative use of a longer phase encoding period will increase the delay between RF excitation and signal detection, thus leading to SNR losses, particularly for rapidly decaying time domain signals which correspond to broad resonance lines. Higher spatial resolution, i.e., a reduced voxel size, will also decrease the inherent SNR, which could be compensated for by a longer total measurement time (averaging) and/or improved RF coil design.

In accordance with the NMR image of Figure 7.5b, the concentration distribution of ethane shown in Figure 7.5c and 7.5d appears nearly homogenous. Just a slight decrease of ethane concentration towards the center of the honeycomb is noticeable. This might be an indication of a lower amount of catalytic material in the central areas compared to the outer areas of the coated monolith, due to an inhomogeneous wetting of the monolith during the coating procedure. Furthermore, no ethane appears to occur in a small area in the centre of the cross section. The apparent lack of ethane is caused by a failure of the fit algorithm, which occurs because artifact signals superimpose the ethylene and ethane signals in the respective areas. The artifact signals may originate from local contamination of the honeycomb. This would also explain the more frequent occurrence of that error in Figure 7.5d, since the influence of local contamination is exacerbated by a low SNR.

7.3.2. MRSI measurement and simulation of the reaction progress

To further investigate the reaction progress along the longitudinal axis of the reactor, the SNR of the MRSI data sets was increased by repeating every experiment three times and adding the time domain signals before performing the fitting procedure. To determine the mean ethane/ethylene ratio of each slice, the amplitudes of each signal were added, and then the ethane/ethylene ra-

tio was calculated from the combined amplitude values. These ethane/ethylene ratios were plotted over the longitudinal position of the slices (cf. Figure 7.6a). The applied averaging process has the advantage, that porosity depending SNR variations do not influence the outcome.

The profiles of the low flow rate experiment of both investigated catalyst beds show a characteristic degressive pattern: After a strong ethane concentration gradient at the beginning of the catalyst beds, the profile flattens and levels at maximum conversion at two-thirds of the length of the catalyst bed and then remains stable until the end of the catalyst bed. The outlier at $z \approx 6\,mm$ of the honeycomb profile are caused by disturbing artifact signals. The localized artifact signals in this slice, which was also observed in the high flow rate experiment of the honeycomb, appeared at the same frequency range as the ethane signal. Both signals added up and caused a reproducible overestimation of the ethane/ethylene ratio in that slice. Note that the ethane/ethylene ratio measured by MRSI at the end of the catalyst bed is in a very good agreement with the ethane/ethylene ratio calculated from the pMS measurements.

Furthermore, the profiles measured at low flow rate are nearly identical for both catalyst supports, which indicates that the different support structures do not influence the process performance significantly. Further it leads to the assumption that differing convectional transport has an insignificant impact on the reaction progress of both reaction systems. The temperature differences between the inlet and the outlet of both catalyst beds support this assumption: The difference for both experiments is about 10 K. The observed temperature difference between the inlet and outlet temperature of the sponge packing and the honeycomb can also be due to a slightly different position of the ethylene glycol capsules: The gap between the uncoated cordierite segments and the coated honeycomb was ca. 1 to 2 mm wider compared to the experimental set up of the sponge packing.

The profiles of the high flow rate experiments differ more considerably: Compared to the profile of the honeycomb support the profile of the sponge packing is less degressive, the maximum conversion is reached only at the end of the catalyst bed. In addition, the outlet temperatures of both experiments differ by more than 10 K, while the inlet temperatures are nearly identical. It is worth to point out that in both experiments the final conversions determined by either MRSI or pMS measurements are in good agreement.

The differences compared to the low flow rate experiments are unlikely the result of different mass transport limitations (cf. Appendix), but rather indicate an enhanced influence of convection. Under consideration of the isobaric reaction conditions and the same flow rate in both setups, the gas load within both catalyst beds should be constant. The sponge packing, however, has a higher amount of struts per volume element compared to the honeycomb. This would lead to an increased gas flow velocity within the sponge packing and thus to a decrease of contact time of the gas molecules, which could cause the flatting of the ethane/ethylene ratio profile. In addition, the increased flow velocity would move the reaction zone somewhat further to the outlet.

To prove the physical plausibility of the 3D MRSI measurements, the model introduced in section 7.2.4 was used to simulate the ethylene hydrogenation process and the results were compared with the findings of the MRSI measurements. A well known problem of validating simulation approaches with experimental data is accurate knowledge of the boundary conditions of a process. Therefore, the low flow rate experiment of the honeycomb was chosen to validate the simulation approach. The temperature boundary conditions were assumed to be nearly isothermal, because on the one hand the temperature difference between the inlet and the outlet is comparably low. On the other hand the concentration gradients are quite low across the cross section of the catalyst bed (cf. Figure 7.5c, Figure A3). However, the occurring concentration gradients appear to be more localized. In addition, the NMR signal intensity profiles indicate that there are only minor temperature differences between the central and boundary areas of the catalyst bed (cf. Figure A4). Accordingly, the applied 1D simulation approach should be adequate to provide reasonable results.

The model used for simulation (cf. Eq. 7.1 to 7.7) was not completely deterministic and required a fitting of the pre-exponential factor (set to $1.7794\,10^{-22} mol\,s^{-1}Pa^{-1.18}$) to the experimental data (cf. Figure 7.6b). The simulation shows the same degressive pattern as the MRSI derived ethane/ethylene ratio profiles. Model and experimental data diverge slightly at the end of the catalyst bed. The deviation between model and

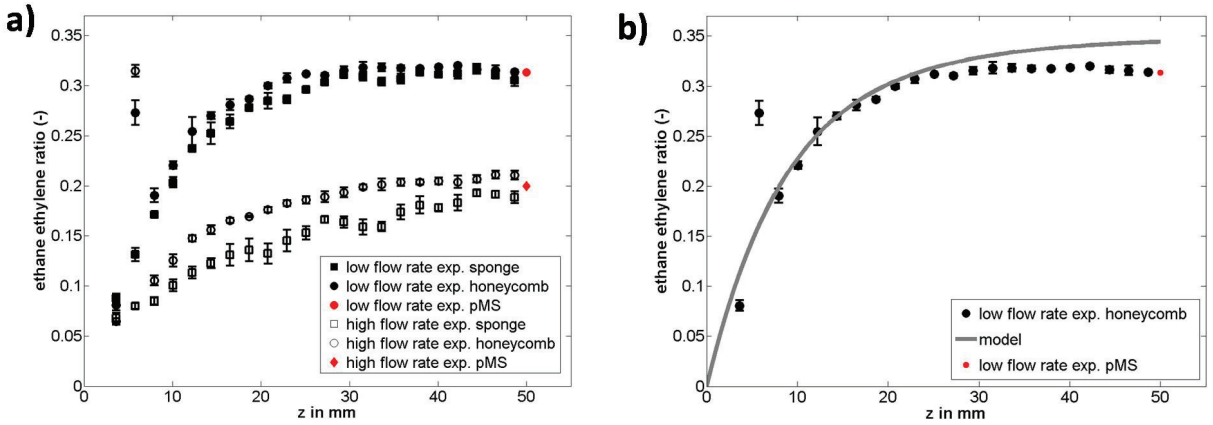

Figure 7.6.: (a) Ethane/ethylene ratio profiles of the experiments of this study. The standard deviation was calculated on the basis of the three individual measurements. The outliers of the honeycomb profiles are caused by measurement artifacts as described in the text. (b) Ethane/ethylene ratio profile of the low flow rate experiment catalyzed by the honeycomb with superimposed model of the reaction process.

experimental data is below 10 % and can at least partly be explained by slightly different flow conditions between model and experiment: While in the model all of the reactant gases flow through the catalyst bed and nearly all of the hydrogen is converted, in the experiment a small share of the reactant gases permeates through the sealing cord (cf. Figure 7.2) and is not available for the catalytic reaction. This small amount of not converted hydrogen was also detected by the pMS at the outlet (cf. Table 7.1) and lead to somewhat reduced ethane/ethylene ratios compared to the model. In addition, in the simulation the reaction process is assumed to be completely isothermal, while in the experiments some temperature gradients along the catalyst bed are very likely to occur. These diverging boundary conditions are also a source for discrepancies between model and experimental data.

However, despite the deviations between model and experimental data at the end of the catalyst bed and the necessary adjustment of the kinetic model, the simulation underlines physical plausibility of the experimental data and forms the basis for future investigations.

In the high flow rate experiments, no reliable assumptions for boundary conditions could be made due to considerable temperature differences between the inlet and the outlet. The determination of the boundary conditions of these experiments is still an open question and will be subject of future studies.

Regarding the applicability of 3D MRSI for characterizing catalyzed gas reactions in larger model reactors, a number of aspects have to be considered. The gas molecules should give rise to NMR signals at different chemical shifts to enable signal separation. To achieve a sufficient SNR, a compromise is required between the spatial resolution, the measurement time and the gas concentration. Furthermore, optimized NMR pulse sequences (with ultrashort echo time) and NMR hardware components (e.g., high static magnetic field, strong and rapidly switchable magnetic field gradients, efficient RF coils) are required. In general, data quality will also depend on the properties of the applied catalyst supports and the detected gases (relaxation times), and will be reduced with increasing temperature and flow velocity. The construction of NMR compatible reactors is another critical issue, particularly for studies at high temperature and high pressure. Because of the large number of factors, a detailed analysis of the applicability of MRSI is required for each specific model reactor.

7.4. Conclusion

An optimized 3D MRSI method has been successfully developed to non-invasively map the concentration distribution inside different monolithic catalysts using the ethylene hydrogenation under different reaction conditions as an example. The measured concentrations at the outlet are in remarkably good agreement (deviations below 5 %) with simultaneously performed mass spectrometric measurements. Furthermore, the qualitative development of the reaction progress was con-

firmed by comparing the measured concentration profiles with a 1D model of the reactor, which was based on kinetic data from the literature. Minor deviations between model and experimental data could be explained by differing flow and boundary conditions between experiment and simulation.

However, more efforts should be made to employ the 3D MRSI method not only for measuring spatially resolved gas concentrations but also to determine temperature fields to describe the reaction process more comprehensively [14], and thus validate simulation approaches for various reaction conditions.

In conclusion, the presented study demonstrates the feasibility of measuring spatially resolved concentration maps of a gas phase process non-invasively within different opaque and mechanically inaccessible monolithic catalyst supports. Thus, information from 3D MRSI can provide the basis to develop and validate more complex modeling approaches, which will allow a deeper insight into the interactions between catalyst, catalyst support and gas phase, thus helping to identify potentials for enhancements of process performances.

Acknowledgment

We would like to thank BASF Catalyst Germany GmbH, Nienburg and Roswita Krebs-Goldbecker from the glass workshop of the University of Bremen. This work was in part supported by the German Research Foundation (DFG) within the Research Training Group GRK 1860 “Micro-, meso- and macroporous nonmetallic Materials: Fundamentals and Applications” (MIMENIMA).

References

1. Heck, R., Gulati, S. & Farrauto, R. The application of monoliths for gas phase catalytic reactions. *Chemical Engineering Journal* **82,** 149–156 (2001).
2. Tronconi, E., Groppi, G. & Visconti, C. Structured catalysts for non-adiabatic applications. *Current Opinion in Chemical Engineering* **5,** 55–67 (2014).
3. Gräf, I., Ladenburger, G. & Kraushaar-Czarnetzki, B. Heat transport in catalytic sponge packings in the presence of an exothermal reaction: Characterization by 2D modeling of experiments. *Chemical Engineering Journal* **287,** 425–435 (2016).
4. Hettel, M., Diehm, C., Torkashvand, B. & Deutschmann, O. Critical evaluation of in situ probe techniques for catalytic honeycomb monoliths. *Catalysis Today* **216,** 2–10 (2013).
5. Schildhauer, T., Pangarkar, K., van Ommen, J., Nijenhuis, J., Moulijn, J. & Kapteijn, F. Heat transport in structured packings with two-phase co-current downflow. *Chemical Engineering Journal* **185-186,** 250–266 (2012).
6. Vervloet, D., Kapteijn, F., Nijenhuis, J. & van Ommen, J. A convection-based single-parameter model for heat transport in multiphase tubular reactors packed with closed cross flow structures. *Chemical Engineering Journal* **233,** 265–273 (2013).
7. Koptyug, I. in *Spectroscopic Properties of Inorganic and Organometallic Compounds: Volume 45* (eds Yarwood, J., Douthwaite, R. & Duckett, S.) 1–42 (The Royal Society of Chemistry, 2014).
8. Koptyug, I., Lysova, A., Kulikov, A., Kirillov, V., Parmon, V. & Sagdeev, R. Functional imaging and NMR spectroscopy of an operating gas-liquid-solid catalytic reactor. *Applied Catalysis A: General* **267,** 143–148 (2004).
9. Gladden, L., Mantle, M. & Sederman, A. Magnetic resonance imaging of catalysts and catalytic processes. *Advances in Catalysis* **50,** 1–75 (2006).
10. Lysova, A., Koptyug, I., Kulikov, A., Kirillov, V. & Sagdeev, R. An NMR Imaging Study of Steady-State and Periodic Operation Modes of a Trickle Bed Reactor. *Topics in Catalysis* **52,** 1371–1380 (2009).
11. Jameson, C. Gas-phase NMR spectroscopy. *Chemical Reviews* **91,** 1375–1395 (1991).
12. Glover, P. & Mansfield, P. Limits to magnetic resonance microscopy. *Reports on Progress in Physics* **65,** 1489 (2002).

13. Bouchard, L., Burt, S., Anwar, M., Kovtunov, K., Koptyug, I. & Pines, A. NMR Imaging of Catalytic Hydrogenation in Microreactors with the Use of para-Hydrogen. *Science* **319,** 442–445 (2008).

14. Jarenwattananon, N., Glöggler, S., Otto, T., Melkonian, A., Morris, W., Burt, S., Yaghi, O. & Bouchard, L. Thermal maps of gases in heterogeneous reactions. *Nature* **502,** 537–540 (2013).

15. Moulé, A., Spence, M., Han, S.-I., Seeley, J., Pierce, K., Saxena, S. & Pines, A. Amplification of xenon NMR and MRI by remote detection. *Proceedings of the National Academy of Sciences of the United States of America* **100,** 9122–9127 (2003).

16. Seeley, J., Han, S.-I. & Pines, A. Remotely detected high-field MRI of porous samples. *Journal of Magnetic Resonance* **167,** 282–290 (2004).

17. Ulpts, J., Dreher, W., Klink, M. & Thöming, J. NMR imaging of gas phase hydrogenation in a packed bed flow reactor. *Applied Catalysis A: General* **502,** 340–349 (2015).

18. Ebrahimi, H., Shaghaghi, H. & Tafazzoli, M. Gauge invariant atomic orbital-density functional theory prediction of accurate gas phase ^{1}H and ^{13}C NMR chemical shifts. *Concepts in Magnetic Resonance Part A* **38A,** 269–279 (2011).

19. Cortright, R., Goddard, S., Rekoske, J. & Dumesic, J. Kinetic study of ethylene hydrogenation. *Journal of Catalysis* **127,** 342–353 (1991).

20. Dorling, T., Eastlake, M. & Moss, R. The structure and activity of supported metal catalysts: IV. Ethylene hydrogenation on platinum/silica catalysts. *Journal of Catalysis* **14,** 23–33 (1969).

21. Schlatter, J. & Boudart, M. Hydrogenation of ethylene on supported platinum. *Journal of Catalysis* **24,** 482–492 (1972).

22. Hua, Y. & Sarkar, T. Matrix pencil method for estimating parameters of exponentially damped/undamped sinusoids in noise. *Acoustics, Speech and Signal Processing, IEEE Transactions on* **38,** 814–824 (1990).

23. Wang, Y.-M., Lee, H. & Apte, D. V. Quantitative NMR spectroscopy by matrix pencil methods. *International Journal of Imaging Systems and Technology* **4,** 201–206 (1992).

24. Lin, Y.-Y., Hodgkinson, P., Ernst, M. & Pines, A. A Novel Detection-Estimation Scheme for Noisy NMR Signals: Applications to Delayed Acquisition Data. *Journal of Magnetic Resonance* **128,** 30–41 (1997).

25. Bond, G. *Metal-Catalysed Reactions of Hydrocarbons* (eds Twig, M. V. & Spencer, M. S.) (Springer Science+Business Media, Inc., 2005).

26. Hindmarsh, A. ODEPACK, A Systematized Collection of ODE Solvers, RS Stepleman et al.(eds.), North-Holland, Amsterdam,(vol. 1 of), pp. 55-64. *IMACS transactions on scientific computation* **1,** 55–64 (1983).

27. Kiewidt, L. & Thöming, J. Predicting optimal temperature profiles in single-stage fixed-bed reactors for CO_2-methanation. *Chemical Engineering Science* **132,** 59–71 (2015).

28. J. Nocedal, S. W. *Numerical Optimization* (ed T. Mikosch S. Resnick, S. R.) (Springer, New York, USA, 2006).

8. NMR based validation of modeling approaches

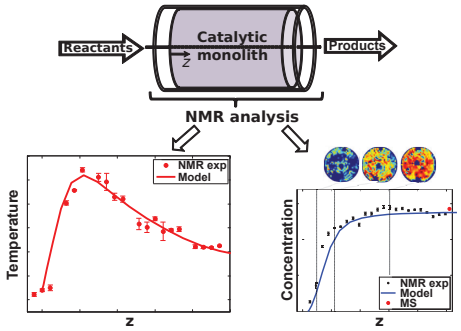

Adapted from:

3D characterization of gas phase reactors with regularly and irregularly structured monolithic catalysts by NMR imaging and modeling

Published in:

Catalysis Today, Received 12.01.2017, Revised 30.03.2017, Accepted 04.05.2017

DOI: 10.1016/j.cattod.2017.05.009

Authors:

Jürgen Ulpts[a,*,†], Lars Kiewidt[a,†], Wolfgang Dreher[b] and Jorg Thöming[a]

[a] University of Bremen, Center for Environmental Research and Sustainable Technology (UFT), Leobener Str. 6, 28359 Bremen, Germany

[b] University of Bremen, Department of Chemistry (FB2), in vivo MR Group, 28359 Bremen, Leobener Str. 2, Germany

[*] Corresponding author. Phone: +49 421 218 63466, E-Mail: julpts@Uni-Bremen.de

[†] shared first authorship (the author's contributions can be found from page 89 onwards)

Abstract: A heterogeneously catalyzed gas phase reaction process was characterized regarding temperature and concentration profiles by means of three dimensional (3D) ^{1}H magnetic resonance spectroscopic imaging (MRSI), using the exothermal ethylene hydrogenation as an example. Here, temperature mapping was achieved by using specifically designed thermometers filled with ethylene glycol.

The impact of heat and mass transfer on the process performance was investigated by using two different monolithic catalysts with completely different heat and mass transfer characteristics: a regularly structured honeycomb monolith and a irregularly structured open-cell foam packing. The influence of these characteristics on the reaction zones within the monolithic catalysts was demonstrated by simulations that were based on 2D reactor models.

To evaluate the applicability of temperature and concentration mapping by ^{1}H MRSI for model validation, a predictive two dimensional model of the process was applied. The resulting simulations of temperature profiles and concentration distributions were in very good agreement with the experimental data with deviations below 9 %. Conventional mass spectroscopic measurements provided further evidence of the accuracy of 3D MRSI measurements as well as the 2D reactor model.

8.1. Introduction

Intensification of gas phase reaction processes benefits from spatially resolved information about process parameters such as concentration conditions, temperature and pressure. By means of process modeling these information can be obtained. To prove the reliability of modeling, validation with measurements of real processes, e.g. those with monolithic catalysts, are necessary [1].

Monolithic catalysts are of particular interest, because their adjustable properties regarding pressure drop as well as mass and heat transfer [2–4] allow the adaption of their catalyst supports to specific challenges of various reaction systems. Usually mathematical approaches are applied to describe reaction processes within such monolithic catalysts and to identify potentials of process intensification [1, 5]. Frequently, these models use mathematical simplifications like correlations for heat and mass transport or fluid properties to save computational costs and development efforts and to maintain flexibility regarding the reuse of the model for different reaction systems.

However, characterization of gas phase processes within monolithic catalysts is especially challenging, due to the typically inaccessible and opaque nature of these supports. The commonly applied measurement methods either provide only integral information, like online gas chromatography (GC) analysis, or they are invasive. Invasive methods however, such as suction probe techniques or probe thermometers [3, 6, 7], can cause design limitations due to the necessary provision of access to the reaction zone, and might yield misleading results caused by a significant increase of the local residence time, in particular when applied to monolithic catalysts [6, 8].

Thus, alternative measurements methods like Nuclear Magnetic Resonance (NMR) based imaging approaches are welcome. NMR imaging is a common tool in medical diagnostics and can provide versatile spatially resolved measurements of concentrations, [9, 10], temperature [11, 12], and velocity [13] within opaque monolithic catalysts without the need for mechanical or optical access [14]. The plausibility of these NMR measurements in terms of qualitative and quantitative characterization of the concentration profiles within heterogeneously catalyzed gas phase processes has already been shown [10], but the validation of modeling approaches of gas phase reaction processes by NMR measurements has not been demonstrated yet. To achieve this objective, information about the temperature conditions within the reaction zones is also needed.

There are already techniques available which allow spatially resolved temperature measurements within fixed-beds of heterogeneously catalyzed gas phase reactions. They measure the temperature directly from either the gas phase of reactants and products [11], or the solid phase [12]. Nevertheless, these techniques require additional equipment for hyperpolarization [11] or ^{27}Al measurements and calibration procedures, which extend the experimental efforts considerably. Furthermore, hyperpolarization techniques are more suited to study micro reactor systems with rather short residence times. However, these restrictions can be overcome by alternative NMR methods.

Such an approach was applied by Gladden et al. [15] to monitor the temperature conditions of a three phase reaction process. They inserted ethylene glycol filled glass spheres (diameter 4 mm) into a packed bed. However, temperature measurements with ethylene glycol filled glass spheres allow temperature measurements with a rather coarse spatial resolution [16] and, because of their size, are not applicable for monolithic catalysts. Nevertheless, the method is applicable if appropriately extended. Thus, we filled ethylene glycol into glass capillaries (diameter 0.68 mm). These capillaries can easily be inserted into the monolithic catalysts and enable the determination of highly resolved temperature profiles along the longitudinal direction of the monolithic catalysts. This allows the combination of simultaneous temperature and gas phase concentration measurements within monolithic catalysts under reaction conditions using the well investigated ethylene hydrogenation as model reaction.

The present contribution is a follow-up of our previous study [10] and closes the temperature boundary condition gap to describe a reaction process sufficiently for validating modeling approaches. To this end, 3D ^{1}H Magnetic Resonance Spectroscopic Imaging (MRSI) measurements are compared to predictive 2D reaction models of the processes using two monolithic catalysts with completely different heat and mass transfer characteristics, as examples.

8.2. Experimental

As in the previous studies we chose the exothermal hydrogenation of ethylene as example reaction, due to its favorable features like selectivity, irreversibility, and good detectability for conventional and ^{1}H MRSI measurement systems. In addition, the high exothermicity of the reaction is expected to have a significant impact on the temperature behavior of the processes which is a main aspect of this study. All NMR experiments were performed with the same experimental setup and the same NMR tomograph (7 Tesla preclinical NMR imaging system, Biospec 70/20, Bruker Biospin GmbH, Ettlingen, Germany) as used in the previous studies [9, 10] unless stated otherwise.

In order to explore the limitation of the temperature measurement methods, the process conditions were changed compared to our earlier studies by reducing the inlet concentration of hydrogen (cf. Table 8.1).

8.2.1. Monolithic catalysts

To investigate the hydrogenation process by means of 3D MRSI, two monolithic catalysts were used: A cordierite honeycomb monolith (length: 50 mm, diameter 25 mm, 600 cpsi, NGK Poland) and a foam packing which consisted of two stacked 10 wt.% SiO_2-Al_2O_3 irregularly structured open-cell foam segments (length 25 mm, diameter 25 mm, 10 PPI, open porosity 79 %, Hofmann Ceramics GmbH, Germany). Both were coated with a 1 wt.% Pt-Al_2O_3 catalyst layer. The amount of coated material was kept comparable: ca. 1.5 g at the honeycomb monolith and ca. 1.45 g at the foam packing. The coating and activation procedure was the same as described in [10].

During operation, the monolithic catalysts were tightly fitted into a glass tube (inner diameter 25 mm; wall thickness 1.5 mm; length 51 mm) to reduce bypass flows and dead zones. The tube containing the monolithic catalyst was in turn inserted into the reactor. The resulting gap between glass tube and inner reactor wall was sealed with glass fiber sealing cord. For measuring the temperature profiles along the rotational axis and along the wall area of the monolithic catalysts, ethylene glycol filled glass capillaries were introduced into the respective areas of the monolithic catalysts (cf. Figure 8.1 and section 8.2.2).

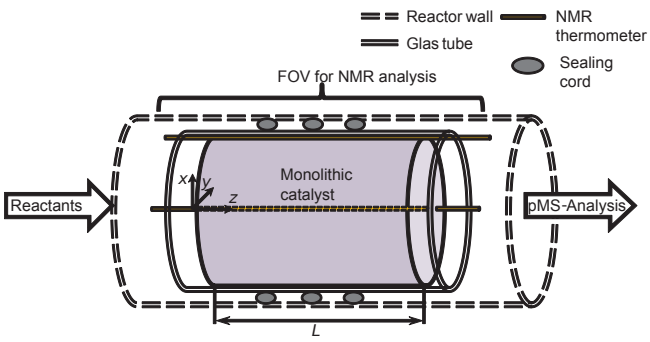

Figure 8.1.: Scheme of the experimental setup with indicated field of view (FOV). The flow direction is from left to right.

8.2.2. Temperature measurements

Temperature measurements along the rotational axis and the wall area of the monolithic catalysts were performed with fused glass capillaries (diameter 0.68 mm, CS Chromatographie Service GmbH, Germany) which were filled with ethylene glycol (99.5 % purity, Fluka, USA). In the following the ethylene glycol filled glass capillaries are referred to as "NMR thermometer". This NMR thermometer is based on the effect that the difference between the resonance frequencies of the two NMR signals of ethylene glycol depends linearly on the temperature and allows temperature measurements up to 165 °C [17, 18]. Furthermore, it allows to determine temperature conditions of NMR experiments within the reactor simultaneously with the MRSI used for gas concentration measurements, without the need for additional equipment or ducts for thermometers. The stick-like shape of the ethylene glycol containers offers the possibility to use it as a multipoint thermometer.

To verify this assumption, the distortion of the temperature profile induced by heat conduction of the glass capillary was investigated prior to its insertion into the monolithic catalysts. For this purpose, an experiment was performed which applied a steep temperature gradient along the longitudinal direction of the glass capillary. To this end, a duct was attached to a Liebig condenser in which the NMR thermometers could be inserted through a membrane (cf. Figure 8.2).

The Liebig condenser was filled with perfluoro polyether (Fomblin, Solvay Solexis, Bollate (MI), Italy), which does not contain hydrogen, and thus, does not distort the temperature measurements by superposition of the ethylene glycol spectra with additional signals. During the 3D MRSI measurements, the Liebig condenser was heated with a

Table 8.1.: Experimental parameters (volume flow, concentration) of the honeycomb and foam packing experiments. During the experiments the pressure level was kept constant at 1.3 bar (abs). The volumetric concentrations were measured with a process mass spectrometer (pMS) behind the outlet of the reactor. The concentration measurements were performed at steady state conditions. The measurement uncertainty of the pMS for all experiments was below 0.5 %.

	Honeycomb experiment		Foam packing experiment	
Inlet				
$\dot{v}_{Ar}$	0.41	$Nl\,min^{-1}$	0.4	$Nl\,min^{-1}$
$\dot{v}_{C_2H_4}$	0.53	$Nl\,min^{-1}$	0.52	$Nl\,min^{-1}$
$\dot{v}_{H_2}$	0.067	$Nl\,min^{-1}$	0.067	$Nl\,min^{-1}$
Linear velocity	3.4	cm/s	3.4	cm/s
Outlet				
c_{Ar}	44.8	vol.%	46.5	vol.%
$c_{C_2H_4}$	47.4	vol.%	45.3	vol.%
$c_{C_2H_6}$	7.3	vol.%	7.7	vol.%
c_{H_2}	< 0.5	vol.%	< 0.5	vol.%

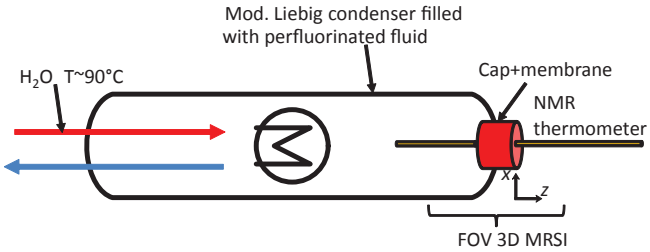

Figure 8.2.: Scheme of the modified Liebig condenser used to validate the NMR thermometers.

constant flow of hot water (90 °C). To prevent heating of the surrounding inside the tomograph, slight air flow was induced by pressurized air ($\sim 1\ Nl\,min^{-1}$). To prove the reliability of the NMR derived temperature measurements, the temperature profile was also compared to conventional thermocouple measurements (resolution 0.1 °C, GTH 1170, Greisinger, Germany). Furthermore, the measured temperatures were compared to the analytical solution of unilaterally heated fin with uniform cross sectional area and adiabatic boundary conditions at the tip [19]:

$$T(z) = (T_1 - T_U) \cdot \frac{\cosh(m \cdot (L_{fin} - z))}{\cosh(m \cdot L_{fin})} \tag{8.1}$$

with

$$m = \sqrt{\frac{\alpha \cdot C_{fin}}{\lambda_{fin} \cdot L_{fin}}}. \tag{8.2}$$

Here, the thermal conductivity of the fin was assumed to be $0.25\ W\,m^{-1}\,K^{-1}$, the same as ethylene glycol [20].

8.2.3. Kinetic measurements

The catalyst used for the kinetic analysis consists of material of the washcoat suspension, which was dried at 120 °C and calcinated at 490 °C for 3 h each. The calcinated suspension was milled and fractionated. For the kinetic investigation the 150 µm to 250 µm fraction was used to avoid intraparticle mass transport limitations. A sample of 10.6 mg of this fraction was diluted with 90 mg of pure Al_2O_3 particles (grain size: 150 µm to 250 µm), inserted into an U-shaped tubular glass reactor (inner diameter 4 mm), and fixed with glass wool plugs. The catalyst was then activated at the same conditions applied to the monolithic catalysts using a constant flow of hydrogen and nitrogen (N_2:H_2 1:5) at a temperature of 400 °C. To run the ethylene hydrogenation reaction for the kinetic studies, the reactor was supplied with ethylene (purity 3.0, Linde, Germany) and hydrogen (purity 3.0, Linde, Germany) by mass flow controllers (Omega Engineering, USA). The mass related space velocity was varied between $5.5\ Nl/g_{cat}$ and $27.5\ Nl/g_{cat}$, while the molar hydrogen fraction of the reactants was always kept below 10 % to maintain isothermal conditions. To monitor the pressure conditions, pressure gauges were attached to the inlet and outlet of the catalyst bed. The inlet pressure was kept constant at 1.15 bar (abs) and for all experiments the pressure drop never exceeded 10 %.

To achieve isothermal conditions during the kinetic measurements the kinetic reactor was placed inside a constantly circulating oil bath of a thermostat (Ultra 300, Lauda, Germany). In addition, the wall temperature of the reactor was moni-

tored with a thermometer equipped with a NiCr-Ni probe (resolution 0.1 °C, GTH 1170, Greisinger, Germany). The concentration of reactants and products were analyzed by the same mass spectrometer (pMS, GAM 200, InProcess Instruments, Germany) which was also used for the NMR setup. Prior to the experiments, it was calibrated with test gases manufactured by Linde (Germany) (Ar:H_2, Ar:C_2H_4, Ar;C_2H_6; each 90 vol.%: 10 vol.% with regard to standard conditions, relative measurements uncertainty: 2 %). Before the kinetic analysis, the ethylene hydrogenation was operated at 180 °C with 25 Nml min^{-1} H_2 and 250 Nml min^{-1} C_2H_4 for 2 h to take account of the initial deactivation of the catalyst [21]. After achieving stationary activity of the catalyst kinetic data were recorded in a temperature range between 60 °C and 150 °C.

8.2.4. 3D MRSI temperature and concentration measurements

The 3D MRSI experiments allowed the detection of 22 slices along z-direction of the monolithic catalysts with a total measurement time of about 20.1 min. The Signal-to-Noise Ratio (SNR) of the MRSI data sets was increased by repeating every experiment nine times. The 3D MRSI sequence and quantitative data evaluation by the matrix pencil method used for temperature and concentration measurements have already been described in [10]. The ethane-ethylene ratio in each voxel was derived by determining the amplitudes $\widehat{U}_i$ of the ethane and ethylene signals, normalizing to the number of attached hydrogen atoms and relating them to one another:

$$\text{Ethane-ethylene ratio} = \frac{c_{C_2H_6}}{c_{C_2H_4}+c_{C_2H_6}} = \frac{\frac{\widehat{U}_{C_2H_6}}{6}}{\frac{\widehat{U}_{C_2H_4}}{4}+\frac{\widehat{U}_{C_2H_6}}{6}}. \tag{8.3}$$

The MRSI data sets of this study were processed using in-house developed IDL (Interactive Data Language, version 7.0, Exilis Visual Information Solutions, Bolder, USA) and Matlab (version 7.11.0, TheMathWorks, Inc., Natick, USA) programs of the previous study, which were adapted to the recent experimental design. Note that the matrix size for spatial resolution (in x,y,z) was 63×63×49 with spherically reduced phase encoding and a rectangular field-of-view (FOV) of 63 × 63 × 105 mm^3, whereas for the temperature validation experiments the matrix size was decreased to 42 × 42 × 42 with spherically reduced phase encoding and a rectangular FOV of 63 × 63 × 31.5 mm^3 to achieve a maximum of spatial resolution in longitudinal direction.

8.3. 2D pseudo-homogeneous fixed-bed reactor model

8.3.1. Governing balance equations

For the simulations of the concentration and temperature fields, we used a 2D pseudo-homogeneous model ($T_\mathrm{f} = T_\mathrm{s} = T$) of an axisymmetric tubular fixed-bed reactor. The model domain is composed of a catalytically active section of length L and diameter D, and a non-catalytic outlet section of length $L/2$ (see Figure 8.3). The corresponding species continuity and energy equations including transient changes, convective transport, axial and radial dispersion, and chemical source terms read:

$$\varepsilon_\mathrm{o}\rho_\mathrm{f}\frac{\partial\omega_i}{\partial t} = -\rho_\mathrm{f}v_\mathrm{s}\frac{\partial\omega_i}{\partial z} - \frac{\partial j_{\mathrm{z},i}}{\partial z} - \frac{\partial j_{\mathrm{r},i}}{\partial r} - \frac{1}{r}j_{\mathrm{r},i} + (1-\varepsilon_\mathrm{o})\,\rho_\mathrm{cat}M_i\sum_{j=1}^{n_\mathrm{R}}\eta_j\nu_{ij}r_j^{(\mathrm{m})} \tag{8.4a}$$

$$(\rho c_\mathrm{p})_\mathrm{eff}\frac{\partial T}{\partial t} = -\rho_\mathrm{f}v_\mathrm{s}c_{\mathrm{p,f}}\frac{\partial T}{\partial z} - \frac{\partial q_\mathrm{z}}{\partial z} - \frac{\partial q_\mathrm{r}}{\partial r} - \frac{1}{r}q_\mathrm{r} + (1-\varepsilon_\mathrm{o})\,\rho_\mathrm{cat}\sum_{j=1}^{n_\mathrm{R}}\eta_j r_j^{(\mathrm{m})}\,(-\Delta_\mathrm{R}H^\circ) \tag{8.4b}$$

with

$$(\rho c_\mathrm{p})_\mathrm{eff} = \varepsilon_\mathrm{o}\rho_\mathrm{f}c_{\mathrm{p,f}} + (1-\varepsilon_\mathrm{o})\,\rho_\mathrm{s}c_{\mathrm{p,s}}. \tag{8.5}$$

In addition, we used an overall steady-state continuity equation, $\rho_\mathrm{f}v_\mathrm{s}$ = const., to calculate the uniform superficial velocity along the reactor axis. Radial velocities were not considered as they are usually smaller by a factor R/L.

The parameter $(\rho c_\mathrm{p})_\mathrm{eff}$ is important to accurately describe the dynamic behavior of the reactor. If dynamics is not relevant, however, one can artificially decrease its value to accelerate the approach to steady state, or increase its value to underrelax the time integration and promote numerical stability. In this study we set $\rho_\mathrm{s} = 3350\,\mathrm{kg\,m^{-3}}$ and $c_{\mathrm{p,s}} = 1000\,\mathrm{J\,kg^{-1}\,K^{-1}}$, corresponding to the Al_2O_3 foam properties, and calculate the fluid density and specific heat from correlated equations [20].

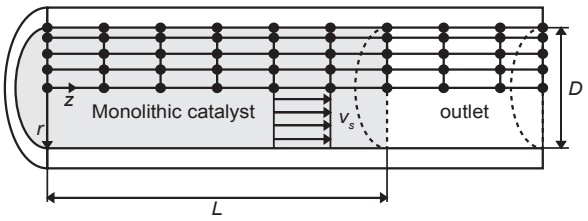

Figure 8.3.: Sketch of the reactor model indicating the monolithic catalyst of length $L = 50\,\mathrm{mm}$ (gray), the outlet section of length $L/2$ (white), and the nodes of the computational grid (•). The tube diameter $D = 25\,\mathrm{mm}$. A plug flow with superficial velocity v_s is assumed in both sections.

Eqs. (8.4) were solved simultaneously (see section 8.3.4) subject to the following initial conditions

$$\omega_i(0,z,r) = \omega_{i,0} \tag{8.6a}$$
$$T(0,z,r) = T_0, \tag{8.6b}$$

and the following boundary conditions

$$\omega_i(t,0,r) = \omega_{i,0} \tag{8.7a}$$
$$T(t,0,r) = T_0 \tag{8.7b}$$
$$j_{i,\mathrm{z}}(t,L,r) = 0 \tag{8.7c}$$
$$q_\mathrm{z}(t,L,r) = 0 \tag{8.7d}$$
$$j_{i,\mathrm{r}}(t,z,0) = 0 \tag{8.7e}$$
$$q_\mathrm{r}(t,z,0) = 0 \tag{8.7f}$$
$$j_{i,\mathrm{r}}(t,z,R) = 0 \tag{8.7g}$$
$$T(t,z,R) = T_\mathrm{w}(z). \tag{8.7h}$$

We allowed the constant wall temperature $T_\mathrm{w}(z)$ to be a function of the axial coordinate z to account for non-isothermal wall temperatures during the experiments.

Here, we did not include a momentum balance in the model and thus assume isobaric conditions. This assumption is justified because of short lengths and high permeabilites of the catalyst supports. Furthermore, we switched off the source terms in the outlet section by setting the catalyst mass manually to zero, so that the Neumann boundary conditions at the outlet did not influence the concentration and temperature profiles within the monolithic catalysts.

The effectiveness factors η_j modeled diffusional transport limitations within the mesoporous washcoat. For the conditions investigated in this study, we found $\eta_j = 0.98$ for the honeycomb and $\eta_j = 0.89$ for the foams (see Appendix A8.1). Note that Bischoff's [22] analytical approximation of the effectiveness factor gives unrealistic results in our case because the assumption of strong diffusional limitations is not met for the given washcoat.

8.3.2. Kinetic model

To derive an explicit expression for the reaction rate $r^{(\mathrm{m})}$ of the Pt-catalyzed ethylene hydrogenation reaction, a single rate equation was chosen, because the hydrogenation of ethylene yields ethane as the only product. Moreover, the reaction conditions of this study are limited to temperatures above 330 K with an excess of ethylene. Thus it is assumed, that a power law approach of the form

$$r^{(\mathrm{m})} = k p_{\mathrm{H2}}^n p_{\mathrm{C2H4}}^m \tag{8.8}$$

with

$$k = k_\mathrm{inf} \exp\left\{-\frac{E_\mathrm{a}}{R_\mathrm{u} T}\right\} \tag{8.9}$$

is justified for the limited temperature range of this study [23].

To fit the kinetic law approach to the measured kinetic data the parameter k_inf was estimated by using the rate equation 8.8 as objective function for a minimization problem, whereas $\mathrm{E_a}$ was set to 37.0 kJ/mol, n to 1.18, and m to -0.6. The values of these parameters were derived from previously published kinetic studies [23] and not additionally fitted to avoid overfitting. The location of the global minimum of this function was approximated by applying a differential evolution algorithm [24] with an initial population of 50, which was developed over 200 generations. Subsequently, the found parameters were used as initial values to determine the local minimum by means of a least square estimation algorithm [25].

The fitting routine estimated the frequency factor to be $k_\mathrm{inf} = 9.98\,\mathrm{mol\,s^{-1}\,kg^{-1}\,Pa^{-0.58}} \pm 0.90\,\mathrm{mol\,s^{-1}\,kg^{-1}\,Pa^{-0.58}}$. To evaluate the accuracy of the kinetic modeling approach, the experimentally determined and calculated hydrogen conversions are compared in Figure 8.4 and show no systematical deviations for different hydrogen flow rates.

8.3.3. Constitutive models and material laws

The mass and heat fluxes in Eqs. (8.4) are modeled by Fick's and Fourier's law, with effective intensities taking into account the material and structure

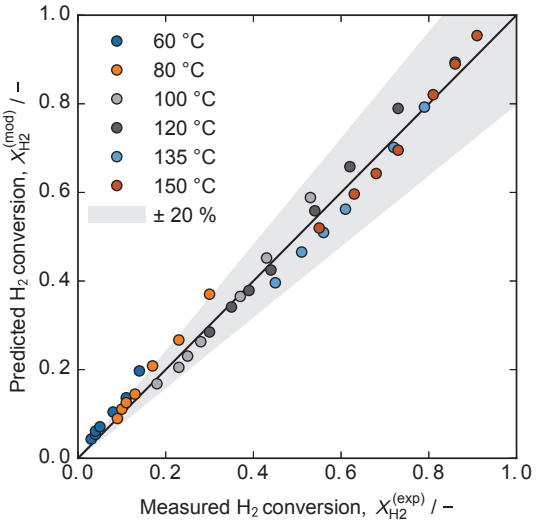

Figure 8.4.: Evaluation of the kinetic model by a parity plot.

of the catalyst support,

$$j_{\mathrm{r},i} = -D^{(\mathrm{eff})}_{\mathrm{rad},i} \frac{\partial \rho_i}{\partial r} \tag{8.10a}$$

$$j_{\mathrm{z},i} = -D^{(\mathrm{eff})}_{\mathrm{ax},i} \frac{\partial \rho_i}{\partial z} \tag{8.10b}$$

$$q_{\mathrm{r}} = -\lambda^{(\mathrm{eff})}_{\mathrm{rad}} \frac{\partial T}{\partial r} \tag{8.10c}$$

$$q_{\mathrm{z}} = -\lambda^{(\mathrm{eff})}_{\mathrm{ax}} \frac{\partial T}{\partial z}. \tag{8.10d}$$

In case of the honeycomb, we use the model of Groppi et al. [26] for the axial effective thermal conductivity, and the model of Visconti et al. [27] for the radial effective thermal conductivity,

$$\lambda^{(\mathrm{eff})}_{\mathrm{ax}} = (1-\varepsilon_{\mathrm{o}})\,\lambda_{\mathrm{s,wc}} \tag{8.11a}$$

$$\lambda^{(\mathrm{eff})}_{\mathrm{rad}} = \frac{1-\varepsilon_{\mathrm{o}}}{1+\varepsilon_{\mathrm{o}}}\lambda_{\mathrm{s,sup}}. \tag{8.11b}$$

Both models are limiting cases for negligible heat transport in the fluid phase ($\lambda_{\mathrm{s}} \gg \lambda_{\mathrm{f}}$) which can safely be assumed for the materials in this study. Note that we assumed different solid thermal conductivities in the axial and radial direction because the thermal conductivity of the Al_2O_3-washcoat ($\lambda_{\mathrm{s,wc}} = 5.8\,\mathrm{W\,m^{-1}\,K^{-1}}$, $\lambda_{\mathrm{Al2O3}} = 25.9\,\mathrm{W\,m^{-1}\,K^{-1}}$ [28], $\varepsilon_{\mathrm{cat,tot}} = 0.77$) is higher than the one of the cordierite support ($\lambda_{\mathrm{s,sup}} = 1.2\,\mathrm{W\,m^{-1}\,K^{-1}}$, [29]). Because of the continuous washcoat, the honeycomb catalyst behaves like a parallel resistor network in the axial direction, where the heat transport in the cordierite support is *negligible*, and like a serial resistor network in the radial direction, where the heat transport in the cordierite support is *limiting*.

The effective mass dispersion coefficients for the honeycomb are

$$D^{(\mathrm{eff})}_{\mathrm{ax},i} = \varepsilon_{\mathrm{o}} D_{\mathrm{mol},i} \tag{8.12a}$$

$$D^{(\mathrm{eff})}_{\mathrm{rad},i} = 0. \tag{8.12b}$$

Here, the radial dispersion coefficient was set to zero to consider in the modeling approach that the concentration gradients at the channel walls become zero. This leads to a decoupling of mass transfer between adjacent nodes in radial direction.

In case of the foams, the models for radial transport are more involved as they take hydrodynamic dispersion into account. For the axial direction we used the model of Lemlich et al. [30], for the radial direction the one of Wallenstein et al. [31],

$$\lambda^{(\mathrm{eff})}_{\mathrm{ax}} = \frac{1-\varepsilon_{\mathrm{o}}}{3}\lambda_{\mathrm{s}} \tag{8.13a}$$

$$\lambda^{(\mathrm{eff})}_{\mathrm{rad}} = \lambda^{(\mathrm{eff})}_{\mathrm{o}} + \frac{v_{\mathrm{s}}}{\varepsilon_{\mathrm{o}}}\frac{\rho_{\mathrm{f}} c_{\mathrm{p,f}} x_{\mathrm{f}}}{8}, \tag{8.13b}$$

where the characteristic length $x_{\mathrm{f}} = 0.99\,(d_{\mathrm{s}} + d_{\mathrm{w}})$, and the stagnant effective thermal conductivity is a weighted sum of a serial and parallel resistor network,

$$\lambda^{(\mathrm{eff})}_{\mathrm{o}} = 0.63\lambda_{\mathrm{ser}} + 0.37\lambda_{\mathrm{par}} \tag{8.14a}$$

$$\lambda_{\mathrm{ser}} = \left(\frac{\varepsilon_{\mathrm{o}}}{\lambda_{\mathrm{f}}} + \frac{1-\varepsilon_{\mathrm{o}}}{\lambda_{\mathrm{s}}}\right)^{-1} \tag{8.14b}$$

$$\lambda_{\mathrm{par}} = \varepsilon_{\mathrm{o}}\lambda_{\mathrm{f}} + (1-\varepsilon_{\mathrm{o}})\,\lambda_{\mathrm{s}}. \tag{8.14c}$$

As the availability of reliable models for the axial and radial mass transport in solid foams is scarce, we used the analogy between heat and mass transport to model the radial dispersion in foams,

$$D^{(\mathrm{eff})}_{\mathrm{ax}} = \varepsilon_{\mathrm{o}} D_{\mathrm{mol},i} \tag{8.15a}$$

$$D^{(\mathrm{eff})}_{\mathrm{rad}} = \varepsilon_{\mathrm{o}} D_{\mathrm{mol},i} + \frac{v_{\mathrm{s}}}{\varepsilon_{\mathrm{o}}}\frac{x_{\mathrm{f}}}{8}. \tag{8.15b}$$

For the fluid density we used the ideal gas equation of state,

$$\rho_{\mathrm{f}} = \frac{pM}{R_{\mathrm{u}}T}. \tag{8.16}$$

Further, we evaluated temperature and composition dependent state-of-the-art correlations by [20] for the remaining fluid properties, such as specific heat and thermal conductivity. Finally, we used Kirchoff's law to calculate the temperature dependent reaction enthalpy.

8.3.4. Numerical solution of the balance equations

To solve the governing reactor equations (8.4), we applied a numerical method of lines. Therefore, we discretized the equations in the spatial domain using Chebyshev-Gauss-Lobatto points and a pseudospectral method [32] to approximate all derivatives except for the convective terms. For the latter we utilized a two-point upwind scheme to enhance stability of the method. We then integrated the semi-discretized equations in time using the well-established CVODE solver from the SUNDIALS suite [33] until steady-state is reached.

8.4. Results and discussion

8.4.1. Validation of temperature measurements

Deviations between actual and measured local temperature can become an issue which has to be considered to estimate the significance of the measured temperature [34]. This is especially true if the characteristics of the applied thermometer are unknown. To test the sensitivity of the NMR thermometers, the Liebig cooler setup as described in section 8.2.2 was used to induce a temperature jump in longitudinal direction of the thermometer. The measured temperature profile is shown in Figure 8.5. To evaluate the ethylene glycol derived temperature profile, the temperature profile along the capillary was also measured with a conventional thermal couple.

The temperature profile shows a slight decrease towards the screw cap of the Liebig cooler, which is the result of the unilateral heating of the test system. Here, the NMR based and conventional measurements are in good agreement. Then the temperature rapidly decreases. Note that NMR based measurements were not possible in this area due to strong magnetic field inhomogeneities. These are a result of the susceptibility differences between cap material, glass and thermal fluid. Consequently, the membrane temperature could only be measured with the conventional thermocouple yielding about 45 °C. Directly behind the membrane the temperature rapidly decreases reaching the surrounding temperature level shortly after.

To estimate the impact of conduction on the NMR measured temperature profile, the result was compared to an analytical solution of a unilaterally heated fin with uniform cross sectional area as

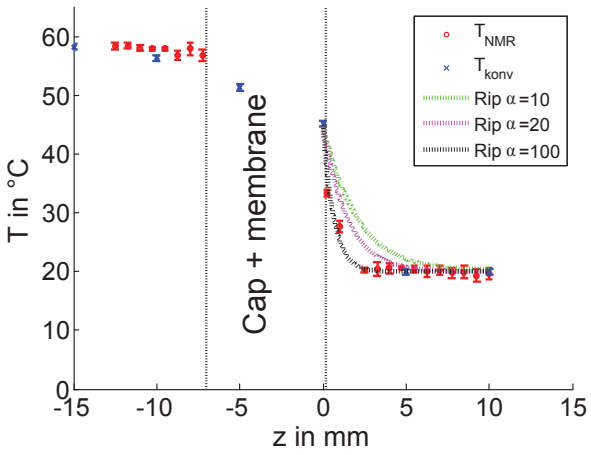

Figure 8.5.: Results of the temperature measurements within the temperature test setup described in section 8.2.2. The blue markers indicate the conventional measurements; here measurement deviations are smaller than symbols. The red markers indicate the temperatures determined by the analysis of the ethylene glycol spectra of the NMR thermometer. Here, the measurement deviations were determined by analyzing the central four ethylene glycol spectra of the NMR thermometer.

described in section 8.2.2, where the heat transfer coefficient was varied in the range of typical values for convective heat transfer of a gas flow [19].

The comparison shows a good agreement with the analytical solution for the case that heat transfer through the shell surface of the capillary is much stronger than heat conduction in longitudinal direction. Thus, we assume that heat conduction in longitudinal direction has only a minor impact on the measured temperature profile. Furthermore, once inserted into the monolithic catalysts, radial heat transfer should be enhanced, because the capillary has direct contact to the monolithic catalyst, which should further increase heat transfer through the shell area.

As a second aspect, we checked the impact of the NMR thermometers on the gas spectra. As the NMR signal intensity of liquids is approximately 1000 times higher than that of gases, it has to be ensured that the insertion of ethylene glycol filled capillaries does not lead to crosstalk of the ethylene glycol signal into the gas signal. This would make concentration measurements in wide areas of the monolithic catalysts impossible and reduce the advantage of contact free concentration measurements crucially. Due to this problem only the inlet and outlet temperatures in non-reactive areas within the FOV of the MRSI experiments were measured in our previous studies [9, 10].

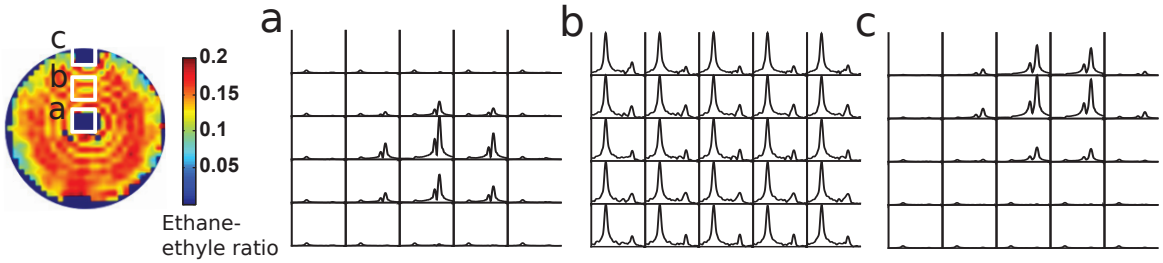

Figure 8.6.: 2D ethane-ethylene ratio map of the cross section of the honeycomb monolith. The spectra map in (a) shows the ethylene glycol spectra of the central area of the catalyst. (b) shows the spectra of ethane and ethylene within the area between both NMR thermometers and (c) are the ethylene glycol spectra of the outer thermometer.

Figure 8.6 shows the measured concentration distribution along the cross section of the honeycomb monolith with inserted NMR thermometers. To estimate the impact of ethylene glycol spectra on adjacent areas, three spectral maps within this cross section are shown: (a) The ethylene glycol spectra of a centrally inserted NMR thermometer area, (b) a spectral map of the area between both thermometers, where only gas signals should be detected, and (c) ethylene glycol spectra of the NMR thermometer of the wall.

As noticeable in Figure 8.6a and 8.6c ethylene glycol spectra are only measured in a confined area of the monolithic catalyst. Within each slice and per NMR thermometer in approximately six to twelve voxels ethylene glycol spectra can be detected, whereas four to six of these spectra can be used for temperature determination. Next to these spectra no superimposition of gas and ethylene glycol spectra is noticed. This is underlined by Figure 8.6b: only magnitude spectra from the gas phase are measured without any contamination by the ethylene glycol spectra. This result was expected because in this study the amount of ethylene glycol used for temperature determination is considerably reduced compared to [10, 15] but is still sufficient to measure reliable temperature profiles as also shown in Figure 8.6a and 8.6c. Thus simultaneous temperature and concentration measurements are possible by accepting a loss of approximately 20 spectra per slice, where just ethylene glycol spectra are measured for temperature determination.

8.4.2. Comparison of MRSI measured and predicted temperature profiles

The temperature conditions of the ethylene hydrogenation process catalyzed by a honeycomb catalyst and monolithic foam packing were analyzed

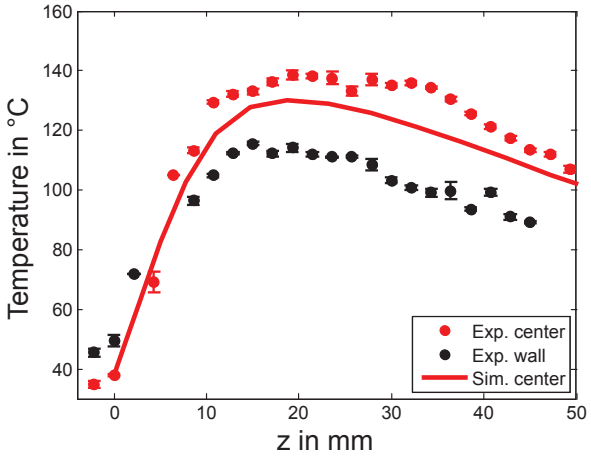

Figure 8.7.: Measured and simulated longitudinal temperature profiles of the honeycomb experiment. The error bars were derived by quantifying the deviations between the ethylene glycol spectra used for temperature determination.

by inserting capillary ethylene glycol thermometers along the rotational axis of the monolithic catalyst (in the following referred to as “center” or “centerline” position) and along the wall areas of the catalyst (referred to as “wall” position). The reaction conditions of the experiments were comparable and are given in section 8.2.

The centerline temperature profile of the honeycomb is shown in Figure 8.7. The temperature increases within the first 20 mm of the honeycomb, reaches a maximum temperature of approximately 140 °C, remains constant for the next 10 mm and then drops slightly towards the outlet to a temperature of ca. 105 °C. The measured wall temperature profile develops nearly parallel to the centerline profile with a maximum temperature of 115 °C which declines smoothly to approximately 85 °C at the outlet.

The temperature profiles clearly indicate the polytropic reaction conditions within the reactor. The wall cooling can only remove a small amount of

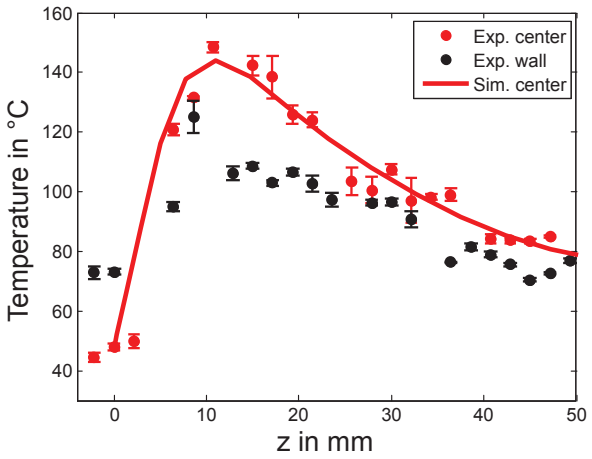

Figure 8.8.: Measured and simulated longitudinal temperature profiles of the foam experiment. The errorbars were derived by quantifying the deviations between the ethylene glycol spectra used for temperature determination.

heat produced by the hydrogenation process. In addition, the centerline temperature profile is typical for a catalyst structure with minor radial thermal conductivity: The heat can not be efficiently removed from central areas to the wall and, thus, it is transported in axial direction and heats up the following sections of the honeycomb. The nearly parallel temperature profile of the wall is a result of superimposed heat removal by the cooling circuit and heating by the outer areas of the honeycomb monolith.

The center temperature of the catalytic foam packing (Figure 8.8) increases with a steeper gradient within the first few millimeters of the foam packing. After 10 mm it shows a pronounced temperature peak of 150 °C. This is followed by a flat decrease in temperature to 80 °C at the outlet of the foam packing. The wall temperature of the catalyst shows a comparable profile: A steep temperature increase in the inlet area of the foam packing results in a temperature peak of 125 °C at z = 8 mm. In the following the temperature decreases smoothly to a temperature of 80 °C at the outlet.

The temperature peaks of the wall and centerline temperature profiles are a result of enhanced radial heat transfer properties of the foam structure compared to the honeycomb structure: In both monolithic catalysts, the exothermal reaction leads to a strong temperature increase shortly after the inlet. But due to the higher radial heat conduction of the catalytic foam packing (ca. factor 5, cf. section 8.3.3) the heat is removed in the rear section of the catalyst which leads to a clearly identifiable hot spot.

In addition, it is noticeable that the measured temperature profile of the foam packing appears to be less continuous than the profile of the honeycomb support. This is likely a result of the temperature measurement method as well as the different characteristics of both supports: To measure the temperature inside the catalyst and in the wall area, no channels were drilled for the thermometer, but the thermometer was inserted along the pores of the foam packing. Thus in areas were the struts of the foam packing are in direct contact with the thermometer, the locally detected temperature can be more affected by the solid temperature of the foam packing than in other areas. This can also explain the temperature peak at the wall at z= 10 mm. Furthermore, the unstructured geometric properties of the foam packing have the disadvantage that it enlarges magnetic field inhomogeneities within the field of view. This can lead to signal corruption and thus makes temperature detection in several slices within the catalyst foam packing impossible. However, the measured temperatures of both experiments exhibit the expected temperature behavior and clearly show the influence of different radial heat conduction characteristics on the temperature profiles. To evaluate the accuracy of the measured temperatures, the processes were compared to reactor models. Since the main deviation of the experimental conditions from ideal reactor behavior is the non-isothermicity in longitudinal and radial direction, the 2D pseudo homogeneous modeling approach of section 8.3 had to be applied to ensure the appropriate description of the heat removal out of the monolithic catalysts.

To simulate the reaction processes with the reactor model, a grid resolution of 15 nodes in radial direction and 25 nodes in axial direction was applied. Furthermore, the wall temperature profiles of the experiments were used to calculate the temperature boundary conditions at $r = R$. The initial parameters for flow rates and pressure levels were the same as applied in the experiments. Note that the model is completely predictive: No fitting of any model parameters to the experimental data sets was done to decrease the deviations between experimental and modeled values. Figure 8.7 shows the model prediction for the center temperature of the honeycomb. In agreement with the experimental data, the maximum temperature is achieved within in the first 20 mm of the honey-

comb. Then, and in accordance with the measured values, the temperature decreases slightly towards the outlet of the honeycomb to a temperature of 100 °C. Although the model underestimates the measured temperatures by approximately 10 % it clearly reflects the heat transfer properties of the honeycomb catalyst. The simulated and measured temperature profiles are nearly parallel with an offset of approximately 9 °C to 15 °C.

The deviations between measured and simulated center temperatures might be due to differences between experiment and model assumptions: While the center temperature of the reactor model is the mean value of solid and gas phase temperature, the thermometer might be more effected by the channel wall temperature of the monolith. The channel wall temperature should be increased to some extent compared to the gas phase, because all the heat of the process is released in the solid phase. Finally, it should be mentioned that isothermal temperature conditions assumed in our previous study [10] could not be confirmed. Furthermore, the occurring temperatures within the honeycomb catalyst were considerably underestimated. These uncertainties made the adaption of the 1D reactor model applied in [10] necessary, and thus, just allowed a qualitative comparison of simulated and measured concentration conditions until now. The current results demonstrate that this gap in knowledge can be closed.

The modeled centerline temperature of the foam packing is shown in Figure 8.8. As in the honeycomb experiment, it predicts temperature conditions within the foam packing considerably well. In accordance with the measured profile a pronounced temperature peak can be detected 10 mm after the inlet. The simulated maximum temperature is with 145 °C just 5 °C lower than the measured temperature. The following flat temperature decrease which is predicted by the model is also validated by the measured temperature profile. Minor deviations between model and measured values are likely the results of the unstructured nature of the foam packing, which can lead to a locally increased contact between foam packing and the thermometer as discussed above. Larger deviations occur at mid-length of the foam packing: Here, the foam packing is interrupted and thus the longitudinal thermal conductance is significantly reduced, which is not considered in the model. Hence, the local temperatures are overestimated to some extend in the model.

8.4.3. Comparison of MRSI measured and predicted concentration profiles

In both simulated processes no major concentration gradients in radial direction are noticed (cf. Figure 8.9a and b). Hence, in both cases the reaction progresses nearly homogeneously along the longitudinal direction of the monolithic catalysts. In addition, it is necessary to note, that due to the low SNR of the individual spectra the measured concentration maps do not allow quantitative comparison to the simulated concentration profiles in each voxel. Thus, the quantitative comparison of the measured and simulated concentration conditions focuses on the averaged longitudinal reaction progress. Therefore, the reaction progress as measured by MRSI was quantified by averaging the ethane-ethylene ratios in every detected slice and plotting the averaged values over their longitudinal postions (cf.[10]).

The concentration maps of the honeycomb structure (Figure 8.10a) indicate the reaction progress: At z = 4 mm just small amounts of ethane are produced. At z = 10 mm the amount of ethane increases considerably. It also appears that more ethane is produced in the outer regions of the honeycomb. A comparable pattern was also detected in a previous study with a similar honeycomb catalyst [10]. This is not intuitive, as the local center temperature is higher than the wall temperature and should rather favor increased reaction rates in central areas of the honeycomb catalyst. In addition, the reactor model does not indicate such concentration gradients (cf. Figure 8.9a). Thus we assume inhomogeneously distributed active material to be the cause of these ring shaped areas of increased ethane concentrations. This is also indicated by scanning electron microscope measurements (data not shown), which showed decreasing washcoat thicknesses towards the centre of the honeycomb. At z = 30 mm ethane appears to be more homogeneously distributed, whereas a ring shaped area of elevated ethane concentrations still occurs.

The corresponding profiles of measured and simulated reaction progress show both a similar degressive pattern (Figure 8.10b): The strongest concentration gradients occur within the first 15 mm of the honeycomb. Then the profile flattens and levels at mid-length of the honeycomb catalyst. The profiles correspond well to the temperature profiles shown in Figure 8.7: At 20 mm, where the maximum temperature is achieved also more than

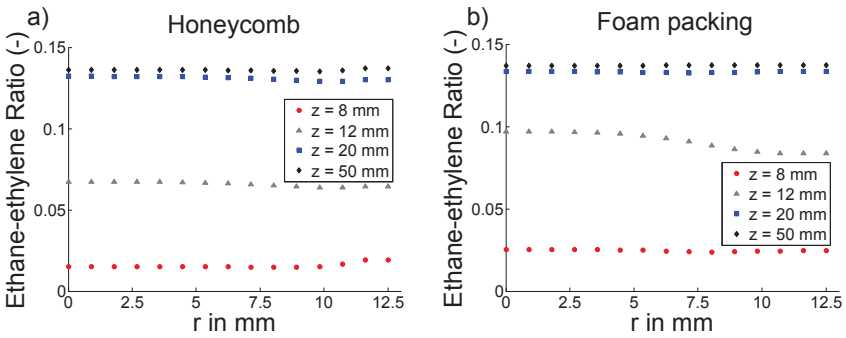

Figure 8.9.: Simulated radial ethane-ethylene ratios of the honeycomb experiment (a) and the foam packing experiments (b) at different longitudinal distances.

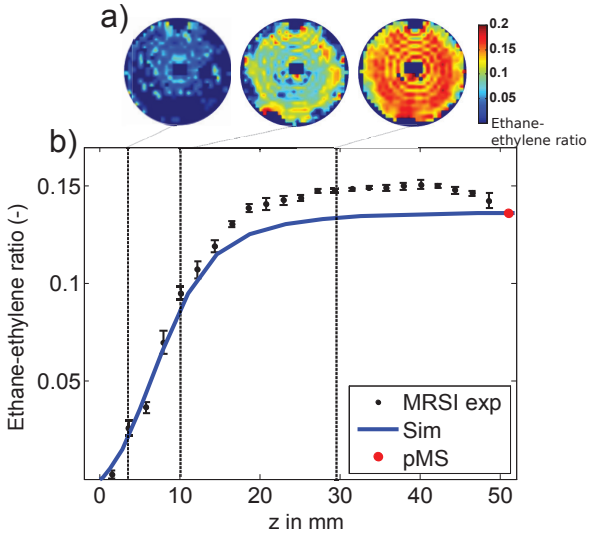

Figure 8.10.: 2D maps and ethane-ethylene ratio profiles of the honeycomb experiments of this study. The standard deviation was calculated on the basis of three averaged experiments.

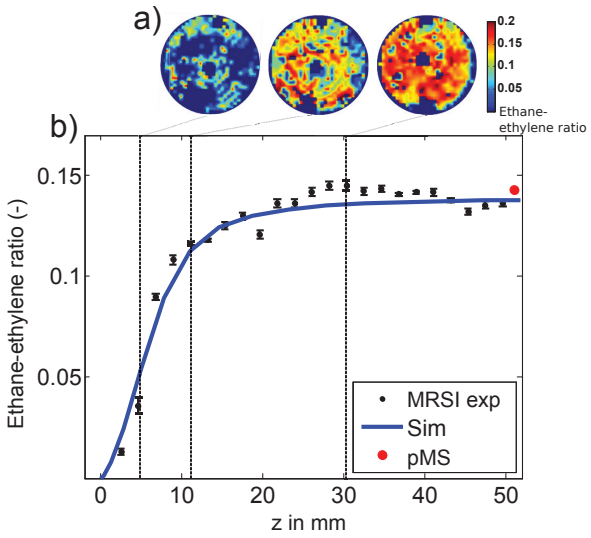

Figure 8.11.: 2D maps and ethane-ethylene ratio profiles of the foam packing experiments of this study. The standard deviation was calculated on the basis of three averaged experiments.

90 % of the available hydrogen is already consumed. In the following only minor amounts of hydrogen are converted to ethane and thus the amount of released heat drops significantly, which results in the flat temperature decrease. The concentration conditions at the outlet measured with the pMS are in good agreement with the simulated ethane-ethylene ratio, whereas the 3D MRSI experiment overestimates the amount of ethane by ca. 10 %. This appears to be a systematic error, because the measured values remain quite stable within the last 25 mm towards the outlet and only deviate insignificantly.

The reaction progress in the foam packing is shown in Figure 8.11. The detected 2D maps of the concentration distribution match the irregular structure of the foam packing: In the inlet area only minor amounts of ethane can be detected, which are randomly distributed all over the cross section of the foam packing (cf. Figure 8.11a). Then the amount of ethane increases with a very irregular distribution. At z = 30 mm the maximum ethylene conversion is achieved and ethane appears to be more uniformly distributed. However, due to the magnetic field inhomgenities induced by the irregular structure and the higher material density of the foam packing, in some voxels the SNR is so heavily reduced that spectra evaluation is made impossible. The averaged reaction progress is also shown in Figure 8.11b. In this experiment the simulated and measured concentration conditions are in excellent agreement. Both show a degressive development but with stronger concentration gradients in the inlet area compared to the honeycomb experiment. This corresponds well to the temperature profile shown in Figure 8.8. Here, the maximum temperature of the foam packing experiment is higher and closer to the inlet of

the foam packing than in the honeycomb experiment. This indicates locally increased conversion rates, which is confirmed by detected stronger longitudinal concentration gradients.

Since both catalysts are coated with a comparable amount of active material and the foam has a significantly lower specific surface area compared to the honeycomb [35], we assume that the enhanced radial gas flow of the foam packing is the reason for the higher conversion rates in the inlet area. In contrast to the honeycomb channels the struts of the foam packing disrupt the longitudinal flow and increase crossmixing, which lead to an enhanced catalyst utilization. A significant outlier of the otherwise comparably continuous profile of the measured values is noticed at mid-length of the foam packing. Here, the two segments are stacked which lead to a local discontinuity. This discontinuity can induce locally elevated field inhomogeneities, which might distort the concentration measurement at this position.

The plausibility of MRSI measurement and reactor model is additionally supported by the pMS measurements: The deviation between MS measurement MRSI measurement and reactor model at the outlet is below 5 %. A systematic measurement error as in the honeycomb experiment was not observed. The origin of this error is still an open question, which will be addressed in future studies.

8.5. Conclusion

A heterogeneously catalyzed ethylene hydrogenation process was successfully characterized by 3D ^{1}H MRSI with respect to temperature and concentration conditions within a regularly structured honeycomb catalyst and a irregularly structured monolithic foam packing. The temperature measurements were achieved by the insertion of ethylene glycol filled glass capillaries. This allowed the determination of temperature boundary conditions, which was still an open question in previous studies [9, 10] and now made the comparison of the measured results with a predictive reactor model of the process possible.

To increase the reliability of the simulations, a microkinetic model of the hydrogenation process was adapted to in-house collected kinetic data and implemented in the reactor model. The predicted concentration and temperature profiles were in good agreement with the results of the 3D MRSI measurement and with the simultaneously performed mass-spectrometric measurements. This underlines the plausibility of the measurements and the accuracy of the 2D reactor model. This approach demonstrates, for the first time, that conventional 3D ^{1}H MRSI based characterization can also be successfully applied to validate simulation approaches of gas phase reaction processes catalyzed by opaque monolithic structures.

The temperature sensing material, ethylene glycol, that was used here for demonstrating the approach, is limited in the temperature measurement range (max. 165 °C). To adopt this approach to processes with elevated temperature conditions chemical agents with a broader range of reproducible temperature depending NMR properties have to be identified. Consequently, our future research will focus on temperature measurements by determining self-diffusions coefficient of high-boiling fluids.

Acknowledgment

This work was in part supported by the German Research Foundation (DFG) within the Research Training Group GRK 1860 “Micro-, meso- and macroporous nonmetallic Materials: Fundamentals and Applications” (MIMENIMA).

We would like to thank Roswita Krebs-Gold-, becker from the glas workshop of the University of Bremen for her obliging assistance with the manufacturing of the experimental setup. In addition, we express our thanks to Miriam Schubert, now at BASF Catalysts Germany, for her assistance with the application of the catalytic coating.

References

1. Jakobsen, H. *Chemical Reactor Modeling* (Springer Science & Business Media, 2014).
2. Heck, R., Gulati, S. & Farrauto, R. The application of monoliths for gas phase catalytic reactions. *Chemical Engineering Journal* **82,** 149–156 (2001).
3. Gräf, I., Ladenburger, G. & Kraushaar-Czarnetzki, B. Heat transport in catalytic sponge packings in the presence of an exothermal reaction: Characterization by 2D modeling of experiments. *Chemical Engineering Journal* **287,** 425–435 (2016).

4. Tronconi, E., Groppi, G. & Visconti, C. Structured catalysts for non-adiabatic applications. *Current Opinion in Chemical Engineering* **5,** 55–67 (2014).
5. Kiewidt, L. & Thöming, J. Predicting optimal temperature profiles in single-stage fixed-bed reactors for CO_2-methanation. *Chemical Engineering Science* **132,** 59–71 (2015).
6. Hettel, M., Diehm, C., Torkashvand, B. & Deutschmann, O. Critical evaluation of in situ probe techniques for catalytic honeycomb monoliths. *Catalysis Today* **216,** 2–10 (2013).
7. Schildhauer, T., Pangarkar, K., van Ommen, J., Nijenhuis, J., Moulijn, J. & Kapteijn, F. Heat transport in structured packings with two-phase co-current downflow. *Chemical Engineering Journal* **185-186,** 250–266 (2012).
8. Hettel, M., Antinori, C. & Deutschmann, O. CFD Evaluation of In Situ Probe Techniques for Catalytic Honeycomb Monoliths. *Emission Control Science and Technology* **2,** 188–203 (2016).
9. Ulpts, J., Dreher, W., Klink, M. & Thöming, J. NMR imaging of gas phase hydrogenation in a packed bed flow reactor. *Applied Catalysis A: General* **502,** 340–349 (2015).
10. Ulpts, J., Dreher, W., Kiewidt, L., Schubert, M. & Thöming, J. In situ analysis of gas phase reaction processes within monolithic catalyst supports by applying NMR imaging methods. *Catalysis Today* **273,** 91–98 (2016).
11. Jarenwattananon, N., Glöggler, S., Otto, T., Melkonian, A., Morris, W., Burt, S., Yaghi, O. & Bouchard, L. Thermal maps of gases in heterogeneous reactions. *Nature* **502,** 537–540 (2013).
12. Lysova, A., Kulikov, A., Parmon, V., Sagdeev, R. & Koptyug, I. Quantitative temperature mapping within an operating catalyst by spatially resolved ^{27}Al NMR. *Chemical Communications* **48,** 5763–5765 (2012).
13. Elkins, C. & Alley, M. Magnetic resonance velocimetry: applications of magnetic resonance imaging in the measurement of fluid motion. *Experiments in Fluids* **43,** 823–858 (2007).
14. Lysova, A. & Koptyug, I. Magnetic resonance imaging methods for in situ studies in heterogeneous catalysis. *Chemical Society Reviews* **39,** 4585–4601 (2010).
15. Gladden, L., Abegao, F., Dunckley, C., Holland, D., Sankey, M. & Sederman, A. MRI: Operando measurements of temperature, hydrodynamics and local reaction rate in a heterogeneous catalytic reactor. *Catalysis Today* **155,** 157–163 (2010).
16. Koptyug, I. in *Spectroscopic Properties of Inorganic and Organometallic Compounds: Volume 45* (eds Yarwood, J., Douthwaite, R. & Duckett, S.) 1–42 (The Royal Society of Chemistry, 2014).
17. Ammann, C., Meier, P. & Merbach, A. A Simple Multinuclear NMR Thermometer. *Journal of Magnetic Resonance* **46,** 319–321 (1982).
18. Kaplan, M., Bovey, F. & Cheng, H. Simplified method of calibrating thermometric nuclear magnetic resonance standards. *Analytical Chemistry* **47,** 1703–1705 (1975).
19. Marek R. Nitsche, K. *Praxis der Wärmeübertragung* (Fachbuchverlag Leipzig, 2012).
20. Kleiber, M. & Joh, R. in *VDI-Wärmeatlas* (ed e.V., V.) 13th ed., 357–488 (Springer, Berlin, Heidelberg, 2013).
21. Cortright, R., Goddard, S., Rekoske, J. & Dumesic, J. Kinetic study of ethylene hydrogenation. *Journal of Catalysis* **127,** 342–353 (1991).
22. Bischoff, K. Effectiveness factors for general reaction rate forms. *AIChE Journal* **11,** 351–355 (1965).
23. Bond, G. *Metal-Catalysed Reactions of Hydrocarbons* (eds Twig, M. V. & Spencer, M. S.) (Springer Science+Business Media, Inc., 2005).
24. Das, S., Mullick, S. & Suganthan, P. Recent advances in differential evolution - An updated survey. *Swarm and Evolutionary Computation* **27,** 1–30 (2016).
25. Branch, M., Coleman, T. & Li, Y. A Subspace, Interior, and Conjugate Gradient Method for Large-Scale Bound-Constrained Minimization Problems. *SIAM Journal on Scientific Computing* **21,** 1–23 (1999).

26. Groppi, G. & Tronconi, E. Honeycomb supports with high thermal conductivity for gas/solid chemical processes. *Catalysis Today* **105,** 297–304 (2005).

27. Visconti, C., Groppi, G. & Tronconi, E. Accurate prediction of the effective radial conductivity of highly conductive honeycomb monoliths with square channels. *Chemical Engineering Journal* **223,** 224–230 (2013).

28. Dietrich, B., Schell, G., Bucharsky, E., Oberacker, R., Hoffmann, M., Schabel, W., Kind, M. & Martin, H. Determination of the thermal properties of ceramic sponges. *International Journal of Heat and Mass Transfer* **53,** 198–205 (2010).

29. Hayes, R., Rojas, A. & Mmbaga, J. The effective thermal conductivity of monolith honeycomb structures. *Catalysis Today* **147, Supplement,** S113–S119 (2009).

30. Lemlich, R. A theory for the limiting conductivity of polyhedral foam at low density. *Journal of Colloid and Interface Science* **64,** 107–110 (1978).

31. Wallenstein, M., Kind, M. & Dietrich, B. Radial two-phase thermal conductivity and wall heat transfer coefficient of ceramic sponges - Experimental results and correlation. *International Journal of Heat and Mass Transfer* **79,** 486–495 (2014).

32. Fornberg, B. *A Practical Guide to Pseudospectral Methods* (Cambridge University Press, Cambridge, 1998).

33. Hindmarsh, A., Brown, P., Grant, K., Lee, S., Serban, R., Shumaker, D. & Woodward, C. SUNDIALS: Suite of Nonlinear and Differential/Algebraic Equation Solvers. *ACM Transactions on Mathematical Software* **31,** 363–396 (2005).

34. Beretta, A., Groppi, G., Lualdi, M., Tavazzi, I. & Forzatti, P. Experimental and Modeling Analysis of Methane Partial Oxidation: Transient and Steady-State Behavior of Rh-Coated Honeycomb Monoliths. *Industrial & Engineering Chemistry Research* **48,** 3825–3836 (2009).

35. Reitzmann, A., Patcas, F. & Kraushaar-Czarnetzki, B. Keramische Schwämme - Anwendungspotenzial monolithischer Netzstrukturen als katalytische Packungen. *Chemie Ingenieur Technik* **78,** 885–898 (2006).

36. Kierzenka, J. & Shampine, L. A BVP Solver Based on Residual Control and the MATLAB PSE. *ACM Transactions on Mathematical Software* **27,** 299–316 (2001).

37. Young, J. & Todd, B. Modelling of multicomponent gas flows in capillaries and porous solids. *International Journal of Heat and Mass Transfer* **48,** 5338–5353 (2005).

Appendix chapter 8

A8.1. Catalyst model

The catalyst model describes the concentration and temperature gradients within the washcoat. The species continuity and energy equations for a 1D slab geometry read:

$$\frac{\mathrm{d}j_i}{\mathrm{d}\xi} = (1-\varepsilon_{\mathrm{cat}})\,\rho_{\mathrm{cat}} M_i \sum_{j=1}^{n_{\mathrm{r}}} \nu_{ij} r_j^{(m)} \tag{A8.1a}$$

$$\frac{\mathrm{d}q}{\mathrm{d}\xi} = (1-\varepsilon_{\mathrm{cat}})\,\rho_{\mathrm{cat}} \sum_{j=1}^{n_{\mathrm{r}}} r_j^{(m)}\,(-\Delta_{\mathrm{R}}H^{\circ})\,. \tag{A8.1b}$$

We solved Eqs. (A8.1a) with a 4th order collocation method similar to Kierzenka et al. [36] subject to the following boundary conditions:

$$\rho_i(\xi=\delta) = \rho_i^{(\mathrm{bulk})} \tag{A8.2a}$$

$$T(\xi=\delta) = T^{(\mathrm{bulk})} \tag{A8.2b}$$

$$j_i(\xi=0) = 0 \tag{A8.2c}$$

$$q(\xi=0) = 0. \tag{A8.2d}$$

To account for multicomponent effects and Knudsen diffusion in the mesopores of the washcoat ($\mathrm{d_p} \approx 14\,\mathrm{nm}$, derived from Hg porosimetry measurements of a comparable washcoat, data not shown), we use the *Cylindrical Pore Interpolation Model* (CPIM) by Young et al. [37], and Fourier's law for the heat flux

$$\frac{\varepsilon_{\mathrm{cat}}}{\tau^2}\frac{\mathrm{d}\rho_i}{\mathrm{d}\xi} = \sum_{j=1}^{n_{\mathrm{s}}}\left(\frac{\omega_i j_j}{D_{ji}^{(\mathrm{eff})}} - \frac{\omega_j j_i}{D_{ij}^{(\mathrm{eff})}}\right) \tag{A8.3a}$$

$$\frac{\varepsilon_{\mathrm{cat}}}{\tau^2}\frac{\mathrm{d}p}{\mathrm{d}\xi} = -A_{\mathrm{A}} \sum_{i=1}^{n_{\mathrm{s}}} M_i^{-1/2} j_i \tag{A8.3b}$$

$$q = -\lambda_{\mathrm{cat}}\frac{\mathrm{d}T}{\mathrm{d}\xi}. \tag{A8.3c}$$

with

$$\frac{1}{D_{ij}^{(\mathrm{eff})}} = \frac{1}{D_{ij}} + \frac{1}{D_i^{(\mathrm{Kn})}} \tag{A8.4a}$$

$$\frac{1}{A_\mathrm{A}} = \frac{1}{A_\mathrm{c}} + \frac{1}{A_\mathrm{Kn}} \tag{A8.4b}$$

and

$$D_i^{(\mathrm{Kn})} = \frac{d_\mathrm{p}}{3}\left(\frac{8R_\mathrm{u}T}{\pi M_i}\right)^{1/2} \tag{A8.5a}$$

$$A_\mathrm{c} = \frac{32\mu_\mathrm{f}}{\rho_\mathrm{f} d_\mathrm{p}^2 \sum_{i=1}^{n_\mathrm{s}} \omega_i M_i^{-1/2}} \tag{A8.5b}$$

$$A_\mathrm{Kn} = \frac{3}{2d_\mathrm{p}}\left(\frac{\pi R_\mathrm{u}T}{2}\right)^{1/2}. \tag{A8.5c}$$

The effectiveness factor is the ratio between the average reaction rate in the washcoat and the reaction rate in the bulk phase,

$$\eta_j = \frac{1}{\delta r_j^{(\mathrm{m,\ bulk})}} \int_0^\delta r_j^{(\mathrm{m})} \mathrm{d}\xi. \tag{A8.6}$$

Figure A8.1 shows the molar fraction profiles within the washcoat for the feed gas composition and pressure at $T = 150\,^\circ\mathrm{C}$. Because of the thin layer on the honeycomb, $\delta = 14.6\,\mu\mathrm{m}$, we can safely neglect diffusional limitations in this case. The washcoat on the foams, however, is approximately 2.5 times thicker so that diffusional limitations do have a small influence on the reaction rate.

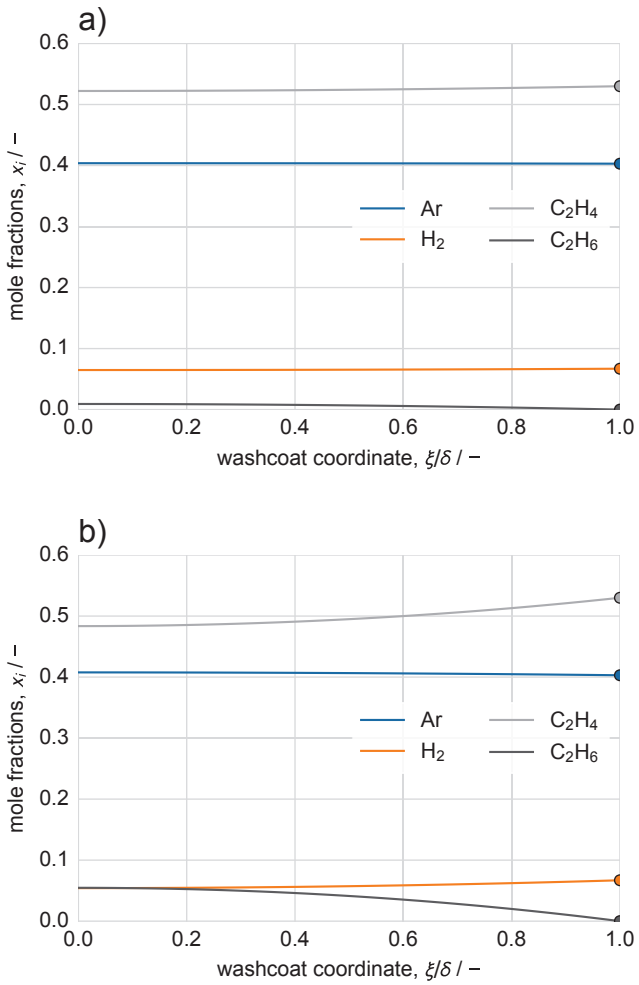

Figure A8.1.: Molar fractions within the washcoat at $p = 1.3\,\mathrm{bar}$, $T = 150\,^{\circ}\mathrm{C}$, and $H_2/C_2H_4 = 0.067/0.403$ in Ar for the honeycomb (a, $\delta = 14.6\,\mu\mathrm{m}$) and the foam (b, $\delta = 38\,\mu\mathrm{m}$). The corresponding effectiveness factors used in the reactor model are $\eta_{\mathrm{honey}} = 0.98$ and $\eta_{\mathrm{foam}} = 0.89$.

A8.2. Notation

Roman		
C_{fin}	cross section of the fin	m
c_i	concentration of species i	$\mathrm{mol\,m^{-3}}$
$c_{\mathrm{p,f}}$	fluid mixture specific heat capacity	$\mathrm{J\,kg^{-1}\,K^{-1}}$
$c_{\mathrm{p,s}}$	solid specific heat capacity	$\mathrm{J\,kg^{-1}\,K^{-1}}$
d_{p}	average pore size of washcoat	m
D	reactor inner diameter	m
D_{ij}	binary diffusivity of species i and j	$\mathrm{m^2\,s^{-1}}$
$D_{\mathrm{mol},i}$	molar diffusivity of species i	$\mathrm{m^2\,s^{-1}}$
$D_i^{(\mathrm{Kn})}$	Knudsen diffusivity of species i	$\mathrm{m^2\,s^{-1}}$
$D_{ij}^{(\mathrm{eff})}$	effective molar diffusivity in washcoat	$\mathrm{m^2\,s^{-1}}$
$D_{\mathrm{ax},i}^{(\mathrm{eff})}$	effective axial diffusivity of species i	$\mathrm{m^2\,s^{-1}}$
$D_{\mathrm{rad},i}^{(\mathrm{eff})}$	effective radial diffusivity of species i	$\mathrm{m^2\,s^{-1}}$
E_{a}	activation energy	$\mathrm{J\,mol^{-1}}$
$\Delta_{\mathrm{R}}H^{\circ}$	enthalpy of reaction j	$\mathrm{J\,mol^{-1}}$
$j_{\mathrm{z},i}$	axial mass flux	$\mathrm{kg\,m^{-2}\,s^{-1}}$
$j_{\mathrm{r},i}$	radial mass flux	$\mathrm{kg\,m^{-2}\,s^{-1}}$
j_i, j_j	mass flux of species i, j in washcoat	$\mathrm{kg\,m^{-2}\,s^{-1}}$
k	reaction rate constant	$\mathrm{mol\,s^{-1}\,kg^{-1}\,Pa^{-0.58}}$
k_{inf}	frequency factor	$\mathrm{mol\,s^{-1}\,kg^{-1}\,Pa^{-0.58}}$
L	reactor length	m
L_{fin}	length of the fin	m
m	reaction order of ethylene	–
M_i	molar weight of species i	$\mathrm{kg\,mol^{-1}}$
M	mixture molar weight	$\mathrm{kg\,mol^{-1}}$
n	reaction order of hydrogen	–
n_{s}	number of species	–
n_{R}	number of reactions	–
p	absolute pressure	Pa
p_{H2}	hydrogen partial pressure	Pa
p_{C2H4}	ethylene partial pressure	Pa
q_{z}	axial heat flux	$\mathrm{W\,m^{-2}}$
q_{r}	radial heat flux	$\mathrm{W\,m^{-2}}$
q	heat flux in washcoat	$\mathrm{W\,m^{-2}}$
r	radial reactor model coordinate	m
$r_j^{(\mathrm{m})}$	rate of reaction j per catalyst mass	$\mathrm{mol\,kg^{-1}\,s^{-1}}$
$r_j^{(\mathrm{m,\ bulk})}$	rate of reaction j at bulk conditions	$\mathrm{mol\,kg^{-1}\,s^{-1}}$
R	reactor radius	m
R_{u}	universal gas constant	$\mathrm{J\,mol^{-1}\,K^{-1}}$
$\widehat{U}_i$	amplitude of NMR signal of species i	–
t	time	s
T_1	membrane temperature	°C
T_{s}	solid temperature	K, °C
T_{f}	fluid temperature	K, °C
T	effective medium temperature	K, °C
T_U	surrounding temperature	°C

T_w	wall temperature	K, °C
T_0	initial temperature	K, °C
$T^{(\mathrm{bulk})}$	temperature in bulk phase	$\mathrm{kg\,m^{-3}}$
$\dot{v}_i$	volume flow of species i	$\mathrm{Nl\,min^{-1}}$
v_s	superficial fluid velocity	$\mathrm{m\,s^{-1}}$
x_f	characteristic length in foam	m
x_i, x_j	molar fraction of species i, j in washcoat	$\mathrm{kg\,m^{-2}\,s^{-1}}$
z	axial reactor model coordinate	m

Greek

α	heat transfer coefficient	$\mathrm{W\,m^{-2}\,K^{-1}}$
δ	washcoat thickness	m
ε_o	open porosity	−
ε_cat	catalyst porosity	−
η_j	effectiveness factor for reaction j	−
λ_f	fluid mixture thermal conductivity	$\mathrm{W\,m^{-1}\,K^{-1}}$
λ_fin	thermal conductivity of the fin	$\mathrm{W\,m^{-1}\,K^{-1}}$
λ_s	solid thermal conductivity	$\mathrm{W\,m^{-1}\,K^{-1}}$
λ_cat	catalyst thermal conductivity	$\mathrm{W\,m^{-1}\,K^{-1}}$
$\lambda_\mathrm{s,wc}$	washcoat material thermal conductivity	$\mathrm{W\,m^{-1}\,K^{-1}}$
$\lambda_\mathrm{s,sup}$	support material thermal conductivity	$\mathrm{W\,m^{-1}\,K^{-1}}$
λ_par	parallel contrib. to thermal conductivity	$\mathrm{W\,m^{-1}\,K^{-1}}$
λ_ser	serial contrib. to thermal conductivity	$\mathrm{W\,m^{-1}\,K^{-1}}$
$\lambda_\mathrm{o}^{(\mathrm{eff})}$	stagnant eff. radial thermal conductivity	$\mathrm{W\,m^{-1}\,K^{-1}}$
$\lambda_\mathrm{ax}^{(\mathrm{eff})}$	eff. axial thermal conductivity	$\mathrm{W\,m^{-1}\,K^{-1}}$
$\lambda_\mathrm{rad}^{(\mathrm{eff})}$	eff. radial thermal conductivity	$\mathrm{W\,m^{-1}\,K^{-1}}$
μ_f	fluid mixture viscosity	Pa s
ν_{ij}	stoichiometric coeff. of species i in reaction j	−
ξ	catalyst model coordinate	m
ρ_f	fluid mixture density	$\mathrm{kg\,m^{-3}}$
ρ_cat	catalyst density	$\mathrm{kg\,m^{-3}}$
$\rho_i^{(\mathrm{bulk})}$	mass concentration of species i in bulk phase	$\mathrm{kg\,m^{-3}}$
τ	catalyst tortuosity	−
ω_i	mass fraction of species i	−
$\omega_{i,0}$	initial mass fraction of species i	−

9. Conclusion

The aim of this work was to demonstrate that MRI can be used to analyze heterogeneously catalyzed gas phase processes in macroscopic tubular reactors. To achieve this, in a first study an experimental set up, suitable for operating safely inside an NMR tomograph, was designed and constructed. Using the exothermic ethylene hydrogenation as model process, spatial mapping of the concentration conditions inside a packed bed at five equally spaced longitudinal positions was achieved by applying an optimized ultrahort echo time MRSI method in combination with a fast and robust time domain fitting algorithm. Furthermore, inlet and outlet temperatures could be monitored by using ethylene glycol filled capsules as NMR thermometers. The influence of different flow rates and hydrogen concentrations on the concentration pattern and temperature levels could be clearly identified.

The averaged concentration conditions were in moderate agreement with integral mass spectrometer measurements: The MRSI measurements underestimated the amount of ethane in the product gas by up to 20 %. Here, saturation effects are expected to cause this underestimation, since ethane was only build in the central parts of the catalyst bed, thus might be more effected by saturation than ethylene, and hence lead to a selective underestimation.

Based on the findings of the first study, the MRSI approach was extended to enable 3D MRSI measurements with a nearly continuous concentration mapping in longitudinal direction. This method was applied to study the ethylene hydrogenation catalyzed by regularly and irregularly structured monolithic catalysts. The continuous solid phase of the catalyst supports did not distort concentration measurements within the monolithic structure. It was even possible to derive structure information from the measured concentration pattern. In addition, the averaged concentration measurements in every detected slice within the monolithic catalysts allowed the determination of the reaction progress in longitudinal direction. The development of the measured reaction progress could be qualitatively confirmed by comparison with a 1D model of the reactor which was based on kinetic data. Here, the MRSI measured concentrations were in very good agreement with integral mass spectrometer measurements with deviations below 5 %. However, the collection of 3D data sets and the low SNR necessitated significantly increased measurement times compared to the multislice approach of the first study.

The third part of this work focused on a quantitative comparison of 3D MRSI measurements of the ethylene hydrogenation process and mathematical modeling. The reaction process here was catalyzed by comparable monolithic catalyst as in the second study. To identify the temperature conditions within the process, an multipoint NMR thermometer was developed and validated by comparative conventional temperature measurements. The insertion of these NMR thermometers inside the monolithic catalysts allowed simultaneous temperature and concentration measurements.

To compare the 3D MRSI derived concentration and temperature profiles to a predictive numerical model, a pseudo homogeneous 2D reactor model was adapted to the investigated process. This was achieved by applying a microkinetic model of the ethylene hydrogenation based on in-house collected kinetic data as well as heat and mass transfer correlations from literature for the used monolithic catalysts. Measured and modeled temperatures were in remarkably good agreement. The accuracy of the 3D MRSI concentration measurements could further be confirmed by mass spectrometer measurements.

Nevertheless, the limitations of the applied methods also have to be mentioned: The long measurement durations allow only the characterization of steady state processes. If lower concentrations than in the presented study should be reliably quantified even longer measurement durations have to be considered to further increase the SNR. Furthermore, the used temperature measurement method is on the one hand easy to apply and does not need any additional calibration measurements. Nevertheless, it is limited to temperature measurements up to a maximum of 165 °C or even lower, if signal separation is not possible anymore. In addition, even though this thermometry approach enables remote detection, it is invasive,

and ethylene glycol has a boiling point of approximately 197 °C. If an ethylene glycol containing thermometer is exposed to higher temperatures it could be destroyed. Both aspects restrict the usability of this temperature measurement technique and thus alternatives would be welcome.

However, the presented work demonstrates, for the first time, an MRI based validation of a predictive reactor model. This is especially noteworthy because gas phase MRI is particularly challenging compared the MRI of the liquid phase. Furthermore, the reaction processes within in tubular reactor of macroscopic size (Ø>20 mm) have been characterized by applying conventional MRI without specialized equipment. So far, this combination has never been demonstrated and is particularly favorable, since it can foster joint ventures of chemical engineering and biological or preclinical MR imaging groups.

10. Outlook

This work addresses the application of conventional MRI to analyze reactive gaseous flows. Since the determination of temperature conditions within such processes has been determined to be one of the major limiting factors, it would be reasonable to focus on the development of NMR thermometry approaches with a broader measurement range. A straightforward solution would be to measure self-diffusion coefficients of high boiling fluids, which are known to depend on temperature. The use of ionic liquids as temperature detector agents for instance could potentially increase the measurement range by a factor of three.

Another option would be to use ^{27}Al thermometry for temperature mapping. MRI experiments with double resonance coils (^{27}Al and ^{1}H) might even enable simultaneous mapping of temperature and concentration.

Since MRSI can provide spatial information, it would also be interesting to compare MRSI measurements of gas phase processes not only to 1D or 2D reactor models, but also to CFD-modeling of reactive flows. To this end, MRV methods could be combinded with spectroscopic imaging approaches to enable simultaneous velocimetry and concentration mapping. In addition to the published studies of gas flows in honeycomb structures (cf. section 3.3), own preliminary work demonstrated the applicability of gas phase MRV to visualize flow pattern in sponge structures (cf. Figure A5), and thus brings the combination of gas phase MRI and MRV within reach. Under certain circumstances it would be even possible to derive the necessary computational grids directly from MRSI/MRV data sets.

Furthermore, experiments at elevated temperatures and pressures would be very interesting since such reactions are more common in industrial practice. The increased pressure should lead to higher spin densities and thus higher sensitivities, which could compensate lower sensitivities due to lower thermal equilibrium polarization. But higher pressures could also have an impact on relaxation processes and diffusion coefficients of the gaseous phase, and thus could lead to biased measurements. Since NMR compatible reactors for such reaction conditions are commercially available, these kinds of experiments are potentially in reach.

It should also be considered to switch to alternative model reactions: A gas phase reaction which can yield more than a single product would enable the determination of macroscopic influences on the selectivity of a process. Even the investigation of 3-phase systems might be possible: Tailored selective saturation MRI methods could allow the alternating detection of the liquid and gaseous phase. Anyway, this would require a detailed analysis of the applicability of MRSI for these alternative processes, which should involve detailed experimental evaluations, due to the multiple determinants on the measurement method. These include, for example, influence of magnetic properties, amount and dispersion of the respective catalyst on the magnetic field of the NMR tomograph, separability and shape of the NMR signals of reactant and product molecules, maximum temperature of the process up to which signal detection is possible, and many more. Due to the variety of potential interactions an evaluation of the respective applicability entirely based on theoretical considerations wouldn't be sufficiently conclusive.

A. Appendix

A.1. Supporting information for chapter 7

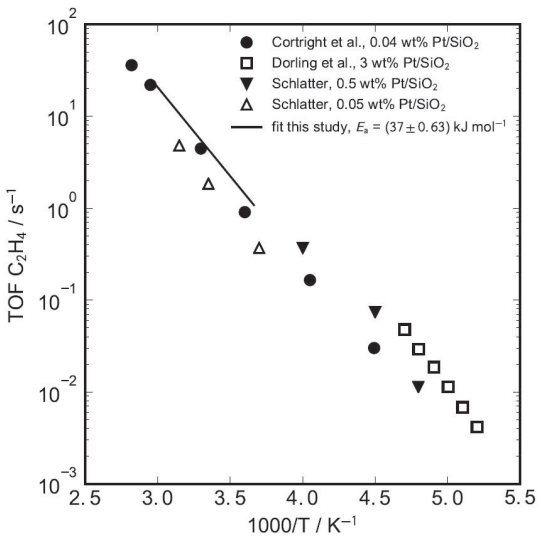

Figure A1.: Arrhenius plot (turnover frequency versus inverse temperature) of the kinetic data from [1], with superimposed model presented in section 7.2.4. For comparison the kinetic data from [2] and [3] are also shown.

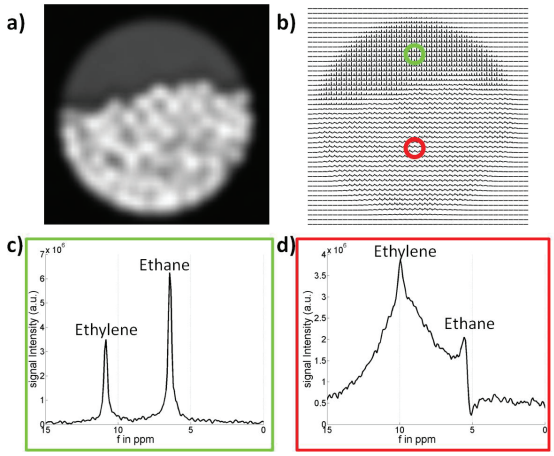

Figure A2.: NMR image of a tube partly filled with commercial cylindrical Al_2O_3-pellets (length: 8 mm; diameter: 3.2 mm; BET: 220 m^2/g; Alfa Aesar GmbH) in a C_2H_4: C_2H_6 atmosphere (gas ratio 50:50 in vol.%; pressure: ca. 1.5 bar (abs)) b) spectral map of the cross section of the tube. Single spectra of the free gas area and the pellet containing area are marked with green and red circles. The associated single spectra of the free gas and the pellets containing area are shown in c) and d). A quantification of the ethane ethylene ratio is in case d) not possible. Note that the adsorption at the pellet surface appears to be batch dependent, because in a prior study [4] another pellet batch was used, which did not show significant adsorption tendencies.

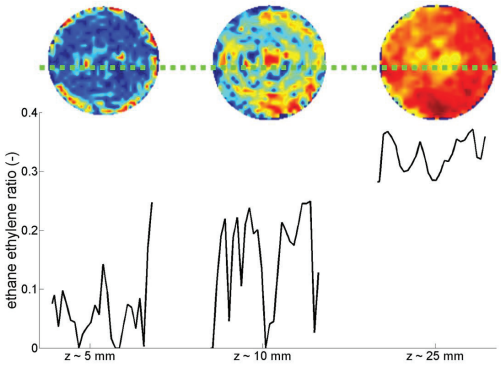

Figure A3.: Profiles of ethane/ethylene ratios calculated from NMR signals along the cross section of the honeycomb under "low flow rate" reaction conditions at three different positions. Only in the first section of the catalyst enhanced activity occurs directly at the wall. The concentration profiles, however, do not show significant gradients between the central and boundary region of the catalyst bed. Instead, the gradients appear to be more localized..

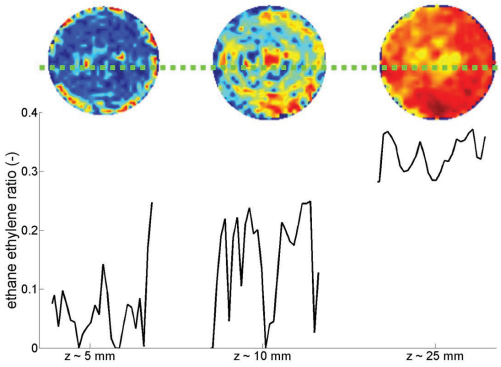

Figure A4.: : Intensity profiles of the NMR signals along the cross section of the honeycomb monolith under "low flow rate"-reaction conditions at three different positions. The intensity profiles do not show a characteristic u-type pattern compared to the intensity profiles shown in [4]. Therefore, we expect no significant temperature gradients along the radial and circumferential direction.

A.1.1. Estimation of the influence of internal and external mass transport

Internal mass transport

The influence of internal mass transport resistance was assessed by estimating the effectiveness factor based on the Thiele modulus:

$$\eta = \frac{\tanh\Phi}{\Phi}.$$

$$\Phi^2 = \frac{\delta^2 r^{(V)}}{D_{eff} c_{\mathrm{C2H4}}}$$

with

$\eta_j =$ effectiveness factor
$\Phi =$ Thiele modulus
$\delta =$ thickness of washcoat, m

$r^{(V)} =$ volumetric reaction rate, $\frac{\text{mol}}{\text{m}^3\text{s}}$
$D_{eff} =$ effective diffusivity, m^2/s
$c_{\text{C2H4}} =$ ethylene concentration, $\frac{\text{mol}}{\text{m}^3}$
Assumption for neglecting internal mass transfer: $\eta \geq 0.95 \longrightarrow \Phi \leq 0.4 \longrightarrow \Phi^2 \leq 0.16$

Calculation of the thickness of the washcoat of the honeycomb monolith (HC) and of the catalytic sponge packing (Sponge)

$$\delta = \frac{V_{\text{WC}}}{A},$$

$$V_{\text{WC,HC}} = \frac{m_{\text{WC,HC}}}{\epsilon_{\text{WC}} \cdot \rho_{\text{Al2O3}}} = \frac{1.5\,\text{g}\,\text{cm}^{-3}}{0.5 \cdot 3.95\,\text{g}} \approx 0.76\,\text{cm}^3$$

$$A_{\text{HC}} = 0.126\,\text{m}^2,$$

$$\delta_{\text{HC}} = \frac{0.76\,\text{cm}^3}{1260\,\text{cm}^2} \approx 6 \cdot 10^{-4}\,\text{cm} = 6\,\mu\text{m}$$

and

$$V_{\text{WC,Sponge}} = \frac{m_{\text{WC,Sponge}}}{\epsilon_{\text{WC}} \cdot \rho_{\text{Al2O3}}} = \frac{1.6\,\text{g}\,\text{cm}^{-3}}{0.5 \cdot 3.95\,\text{g}} \approx 0.81\,\text{cm}^3$$

$$A_{\text{Sponge}} = 0.0353\,\text{m}^2,$$

$$\delta_{\text{Sponge}} = \frac{0.81\,\text{cm}^3}{353\,\text{cm}^2} \approx 20 \cdot 10^{-4}\,\text{cm} = 20\,\mu\text{m}$$

with
$V_{\text{WC,...}}$ = total volume of washcoat on the honey comb monolith (HC) or sponge packing (Sponge), cm^3
A_{HC} = surface of the honey comb monolith with a diameter of 0.025 m, a length of 0.05 m and 600 cpsi, m^2
A_{Sponge} = surface of the sponge packing with a diameter of 0.025 m, a length of 0.05 m and 10 PPI, m^2 estimated from the correlation given in [5]
$m_{\text{WC,...}}$ = total mass of washcoat on the honey comb monolith (HC) or sponge packing (Sponge), g
ϵ_{WC} = porosity of the washcoat (measured by Hg-porosimetry, here $\epsilon_{\text{WC}} \approx 0.5$
ρ_{Al2O3} = density of the wash coat, g/cm^3

Calculation of the Thiele modulus

with $r^{(V)}$(1.3 bar, 328 K)= 1.273 $\frac{\text{mol}}{\text{m}^3}$ (calculated with fitted preexponential factor A)

$$D_{\text{eff}} = \frac{\epsilon}{\tau^2} D_{\text{Kn}} = \frac{\epsilon}{\tau^2} \frac{d_{\text{p}}}{3} \left\{ \frac{8 R_{\text{u}} T}{\pi M_{\text{C2H4}}} \right\}^{1/2} = 4.146 \cdot 10^{-7}\,\frac{\text{m}^2}{\text{s}}$$

The effective diffusivity D_{eff} was calculated from the Knudsen diffusivity considering the reactant molecule with the highest impact on the diffusivity. Here is
d_P = mean pore diameter, for the here applied wash coat ≈ 20 nm, measured by Hg-porosimetry
τ = tortuosity, for the here applied washcoat ≈ 2, assumed for typical washcoats
M_{C2H4} = molecular mass of ethylene, ≈ 28.05 g/mol
This leads to:
$D_{\text{eff}} \approx 4.146 \cdot 10^{-7}\,\frac{\text{m}^2}{\text{s}}$

With the concentration of ethylene c_{C2H4} calculated by the ideal gas law, where x_{C2H4} is the molar fraction of ethylene:

$$c_{\mathrm{C2H4}} = \frac{x_{\mathrm{C2H4}} \cdot p}{R_{\mathrm{u}} T} \approx 22.22 \, \frac{\mathrm{mol}}{\mathrm{m}^3}$$

The square of the Thiele modulus results in:
$\Phi^2_{\mathrm{HC}} \approx 5 \cdot 10^{-7} \ll 0.16$, thus an internal mass transfer limitation for the honeycomb monolith can not be expected.
$\Phi^2_{\mathrm{Sponge}} \approx 6.4 \cdot 10^{-5} \ll 0.16$, thus an internal mass transfer limitation for the catalytic sponge packing can not be expected.

Honeycomb monolith: Estimation of the impact of external mass transport by the Mears' Criterion

Mears′ Criterion:

$$\frac{r^{(V)}_{eff}}{\beta \cdot A_{\mathrm{V,HC}} \; c_{\mathrm{C2H4}}} \leq 0.05$$

with β= mass transfer coeffcient, m/s
$A_{\mathrm{V,HC}}$ = specific surface of a single channel of the honeycomb monolith, 1/m

$$A_{\mathrm{V,HC}} = \frac{4}{D_{\mathrm{HC}}}$$

with
D_{HC} = channel diameter of the honeycomb, ≈ 1 mm

Calculation of the Sherwood number Sh

$$Sh = \frac{\beta \cdot D_{\mathrm{HC}}}{D_{\mathrm{C2H4\text{-}H2}}} \approx 3.6 \text{ (pure diffusion)}$$

with
$D_{\mathrm{C2H4\text{-}H2}}$ = diffusion coefficient of ethylene in hydrogen, m^2/s
leads to

$$\frac{r^{(V)}_{eff} \cdot D^2_{\mathrm{HC}}}{3.6 \cdot c_{\mathrm{C2H4}} \cdot 4 \cdot D_{\mathrm{C2H4\text{-}H2}}} \leq 0.05$$

It therefore follows:

$$\frac{r^{(V)}_{eff} \cdot D^2_{\mathrm{HC}}}{c_{\mathrm{C2H4}} \cdot D_{\mathrm{C2H4\text{-}H2}}} \leq 0.72$$

with

$$r^{(V)}_{eff} = r^{(V)} = 1.273 \frac{\mathrm{mol}}{\mathrm{m}^3 \mathrm{s}}$$

and
$D_{\mathrm{C2H4\text{-}H2}}$ = diffusion coefficient of ethylene in hydrogen, $\approx 5.425 \cdot 10^{-5}$ m^2/s estimated from Chapman-Enskog theory ([6], p. 526)

This leads to:

$$\frac{r_{eff}^{(V)} \cdot D_{\mathrm{HC}}^2}{c_{\mathrm{C2H4}} \cdot D_{\mathrm{C2H4\text{-}H2}}} \approx 1 \cdot 10^{-3} \ll 0.72$$

$\longrightarrow$ The influence of external mass transport can be neglected; a pseudo homogenous modeling approach appears to be justified.

For comparison: estimation of the impact of external mass transport of the sponge packing:

$$Sh = \frac{\beta \cdot D_{\mathrm{Sponge}}}{D_{\mathrm{C2H4\text{-}H2}}} \approx 3.6 \text{ (pure diffusion)}$$

$\longrightarrow$

$$\beta = \frac{3.6 \cdot D_{\mathrm{C2H4\text{-}H2}}}{D_{\mathrm{Sponge}}} \text{ (pure diffusion)}$$

As a result the Mears′ criterion for the sponge packing reads:

$$\frac{r_{eff}^{(V)} \cdot D_{\mathrm{Sponge}}}{3.6 \cdot D_{\mathrm{C2H4\text{-}H2}} \cdot A_{\mathrm{V,Sponge}} \cdot c_{\mathrm{C2H4}}} \leq 0.05$$

with D_{Sponge} = mean pore diameter of the sponge (10 PPI), 2.5 mm
$A_{\mathrm{V,Sponge}}$ = specific surface area of the sponge (10 PPI), $\approx 1440\ \mathrm{m^2/m^3}$, estimated from the correlation given in [5]

the Mears' criterion results to:

$$\frac{r_{eff}^{(V)} \cdot D_{\mathrm{Sponge}}}{3.6 \cdot D_{\mathrm{C2H4\text{-}H2}} \cdot A_{\mathrm{V,Sponge}} \cdot c_{\mathrm{C2H4}}} \approx 5 \cdot 10^{-4} \ll 0.05$$

$\longrightarrow$ For the sponge packing the influence of external mass transport can also be neglected

References

1. Cortright, R., Goddard, S., Rekoske, J. & Dumesic, J. Kinetic study of ethylene hydrogenation. *Journal of Catalysis* **127,** 342–353 (1991).
2. Dorling, T., Eastlake, M. & Moss, R. The structure and activity of supported metal catalysts: IV. Ethylene hydrogenation on platinum/silica catalysts. *Journal of Catalysis* **14,** 23–33 (1969).
3. Schlatter, J. & Boudart, M. Hydrogenation of ethylene on supported platinum. *Journal of Catalysis* **24,** 482–492 (1972).
4. Ulpts, J., Dreher, W., Klink, M. & Thöming, J. NMR imaging of gas phase hydrogenation in a packed bed flow reactor. *Applied Catalysis A: General* **502,** 340–349 (2015).
5. Reitzmann, A., Patcas, F. & Kraushaar-Czarnetzki, B. Keramische Schwämme - Anwendungspotenzial monolithischer Netzstrukturen als katalytische Packungen. *Chemie Ingenieur Technik* **78,** 885–898 (2006).
6. Bird, R., Stewart, W. & Lightfoot, E. *Transport phenomena* (John Wiley & Sons, 2007).

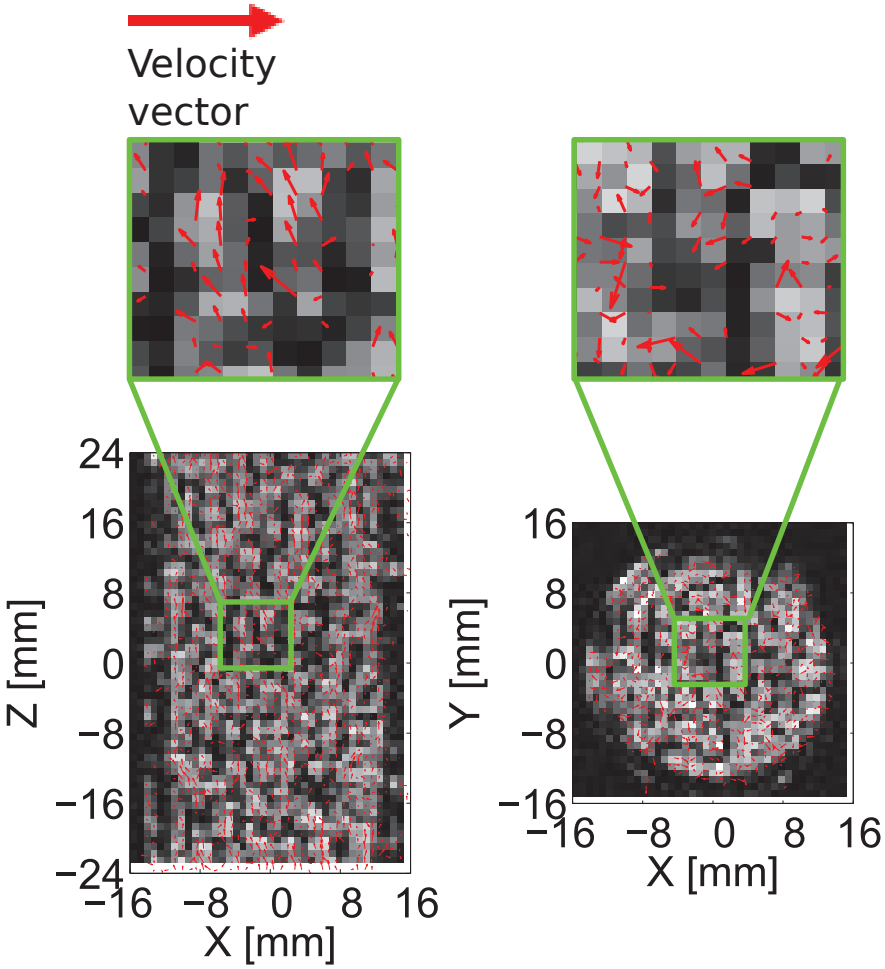

Figure A5.: With 3D Spin Echo Phase Contrast Velocity Mapping measured methane flow through 20 PPI sponge packings. Flow rate: 1.5 L/min; Velocity measurement range: -300 mm/s to 300 mm/s; resolution: 0.8 mm × 0.8 mm × 0.8 mm; data acquisition time: 2.84 h.

Publications presented in this Work

Author Contributions

Publication presented in chapter 6

Jürgen Ulpts, Wolfgang Dreher, Miriam Klink and Jorg Thöming "NMR imaging of gas phase hydrogenation in a packed bed flow reactor".
In: Applied Catalysis A: General 502 (2015), pp. 340–349. DOI: 10.1016/j.apcata.2015.06.011.

Author	Contributions
Jürgen Ulpts	Concept and planning of work, design and construction of the experimental set up, preparation of catalysts, development and validation of temperature measurement method, NMR experiments, data analysis and interpretation, manuscript preparation (design, editing, writing)
Wolfgang Dreher	Development of the MRI method, supervision of the MRI experiments, gave conceptual advices, discussed data, and edited manuscript
Miriam Klink	Preparation of catalysts
Jorg Thöming	Gave conceptual advices, discussed data, edited manuscript

Publication presented in chapter 7

Jürgen Ulpts, Wolfgang Dreher, Lars Kiewidt, Miriam Schubert and Jorg Thöming "In situ analysis of gas phase reaction processes within monolithic catalyst supports by applying NMR imaging methods". In: Catalysis Today 273 (2016), pp. 91-98, DOI: 10.1016/j.cattod.2016.02.062.

Author	Contributions
Jürgen Ulpts	Concept and planning of work, preparation of catalysts, NMR experiments, kinetic modeling, data analysis and interpretation, manuscript preparation (design, editing, writing)
Wolfgang Dreher	Development of the MRI method, supervision of the MRI experiments, gave conceptual advices, discussed data, and edited manuscript
Lars Kiewidt	Development of the model used in this paper, gave conceptual advices, discussed data, edited manuscript
Miriam Schubert	Preparation of catalysts
Jorg Thöming	Gave conceptual advices, discussed data, edited manuscript

Publication presented in chapter 8

Jürgen Ulpts, Lars Kiewidt, Wolfgang Dreher and Jorg Thöming "3D characterization of gas phase reactors with regularly and irregularly structured monolithic catalysts by NMR imaging and modeling". In: Microporous and Mesoporous Materials (2017), accepted 04.05.2017, DOI: 10.1016/j.cattod.2017.05.009.

Author	**Contributions**
Jürgen Ulpts	Concept and planning of work, development and validation of temperature measurement method, NMR experiments, preparation of catalysts, design and construction of experimental setup for kinetic analysis, kinetic study, evaluation of kinetic data, data analysis and interpretation, adaption of the reactor models to the reaction processes and simulation, manuscript preparation (design, editing, writing)
Lars Kiewidt	Development of the model used in this paper, preparation of catalysts, evaluation of kinetic data, prepared sections 8.3.1 and 8.3.3, gave conceptual advices, discussed data, and edited manuscript
Wolfgang Dreher	Supervision of the MRI experiments, gave conceptual advices, discussed data, and edited manuscript
Jorg Thöming	Gave conceptual advices, discussed data, edited manuscript

List of Oral and Poster Presentations

Jürgen Ulpts, Wolfgang Dreher, Lars Kiewidt, and Jorg Thöming "3D Messungen von Konzentrationsfeldern in monolithischen Katalysatoren mittels MRSI". Oral presentation, Reaktionstage 2016, Würzburg, Germany.

Jürgen Ulpts, Wolfgang Dreher, Lars Kiewidt, and Jorg Thöming "In situ Analysis of Gas Phase Reaction Processes within Monolithic Catalyst Supports by applying NMR Imaging Methods", Flash talk and poster presentation, ICOSCAR 5 2016, Donostia-San Sebastian, Spain.

Jürgen Ulpts, Wolfgang Dreher, Lars Kiewidt, and Jorg Thöming "NMR-basierte ortsaufgelöste Charakterisierung von reaktiven Gasströmungen in porösen Systemen". Oral presentation, ProcessNet-Jahrestagung 2016, Aachen, Germany.

Jürgen Ulpts, Wolfgang Dreher, Lars Kiewidt, and Jorg Thöming "NMR-based characterization of gas phase reaction processes within monolithic catalyst supports". Oral presentation, CCE 2016, Baltimore, USA.

“Wenn man Glück mit ‘ue’ schreibt, hat man mehr Buchstaben.”,
Florian Meichsner, Weltraumingenieur und Freidenker